Direct Observation of Ultrafast Lattice Dynamics with Femtosecond X-ray Diffraction

Masaki HADA

2010

Abstract

Over the two last decades, optical, THz, and soft X-ray spectroscopic pump–probe measurements and time-resolved crystallography (X-ray and electron diffraction) have attracted much interest to demonstrate the atomic dynamics of chemical reactions, phase transition and coherent phonon vibrations. Above all, the time-resolved X-ray diffraction experiments have made it possible to directly observe the atomic motion in materials with femtosecond to picosecond time resolution. The purpose of this thesis is to develop the laser-based tabletop time-resolved X-ray diffraction system and to demonstrate the time-resolved X-ray diffraction measurements on a phase transition material.

The fundamental studies of femtosecond laser are mentioned in the first part of this thesis, because all of the spectroscopic pump–probe measurements and the time-resolved crystallography have been based on the femtosecond lasers. The optical reflective pump–probe measurements with femtosecond laser are demonstrated on a bismuth thin film and single crystal silicon. Ultrafast dynamical changes, such as the A_{1g} coherent lattice vibration in bismuth film and non-thermal solid–liquid phase transition in silicon, were observed from the modulation of reflectivity.

The time-resolved X-ray diffraction measurements have been assembled with the synchrotrons facilities or the laboratory-based high-power above 100 mJ/pulse and low repetition rate about 10 Hz femtosecond laser and huge vacuum chamber. However, the utilization of such an ultrafast pulsed X-ray sources have been limited because of the complexity of the huge facility systems or the difficulty in managing large high-power lasers and vacuum systems. Therefore, a high-intensity X-ray source with a tabletop laser would be a desirable for the time-resolved X-ray diffraction measurements. The relationship between Kα X-ray conversion efficiency and the ambient atmosphere near the target surface is explained with a simple electron collision model. This model suggests that the electron mean free path is the important parameter in laser-induced X-ray radiation and the X-ray intensity in helium ambient is calculated to be 30–40% of that in vacuum. This result also suggested the possibility of tabletop time-resolved X-ray diffrac-

tion measurements in air or helium ambient. In this study, we developed the high-intensity tabletop X-ray source which is distinguished by the capability of operating in air or helium atmospheric condition.

The time-resolved X-ray diffraction measurements were demostrated on a single crystalline cadmium telluride (CdTe) and an insulator–metal phase transition material, vanadium dioxide (VO_2), with the tabletop time-resolved X-ray diffractometer. The results from the measurements on CdTe crystal revealed that the longitudinal optical and acoustic phonons were selectively excited with laser pulses and the anisotropic phonons expanded into the deep area of the crystal with acoustic velocity of ∼3400 m/s in the CdTe crystal. This report shows the first experiment of the time-resolved X-ray diffraction measurements with a tabletop time-resolved X-ray diffractometer.

The results from the measurements on VO_2 suggested that the unit cell of low-temperature monoclinic VO_2 transformed into high-temperature tetragonal phase extremely fast (within less than 25 ps); however, the atoms in the unit cell fluctuated with the center of the tetragonal coordinate within ∼100 ps. The intermediate state of the VO_2 has been observed only in the spectroscopic methods; however, it was observed using more direct X-ray diffraction measurement with the changes in the intensity and FWHM of the diffraction lines. The tabletop time-resolved X-ray diffraction system is a promising tool for laboratory-based molecular dynamic studies on materials, chemical and biological systems.

The next generation ultrafast time-resolved crystallography, such as ultrafast time-resolved electron diffraction measurements and time-resolved X-ray diffraction measurements with X-ray free electron laser, are introduced in the last part of this thesis. It is difficult or almost impossible to observe the unrepeatable or irreversible phenomena with the conventional ultrafast time-resolved crystallographic methods because of the intensity or the longitudinal coherence. However, a large majority of the chemical processes in the real world is unrepeatable or irreversible phenomena, and to reveal the phenomena is more and more attractive for scientists. The next generation ultrafast time-resolved crystallography would be a solution for this requirement. In the near future, a series of ultrafast time-resolved optical measurements and crystallographic measurements will break new ground of the science and make a revolution on the scientific world.

Acknowledgements

I would like to express my extremely deep gratitude to Professor Akio Itoh and Associate Professor Jiro Matsuo of Kyoto University for their continuous guidance and encouragement throughout this study. I also would like to thank Professor Jun Kawai of Kyoto University for his comments, advices and discussions of this thesis. I am very grateful to Professor R. J. Dwayne Miller in University of Toronto for his advices, encouragements and allowing me to study in his laboratory.

I would like to thank Professor Ikuo Kanno, Associate Professor Hiromi Shibata, Associate Professor Hidetsugu Tsuchida, and Assistant Professor Makoto Imai of Kyoto University for many helpful comments and advices. I would like to express my heartfelt thanks to Lecturer Toshio Seki and Lecturer Takaaki Aoki of Kyoto University for their continuous advices and experimental assistances, encouragements in my six and half years of student life in Kyoto University. I would like to show my thanks to Mr. Kazuya Ichiki for his assistances, encouragements and mainly giving me a comfortable environment in the laboratory. I also express my thanks to Assistant Professor Satoshi Ninomiya of Yamanashi University, Dr. Yoshihiko Nakata, Mr. Takeshi Murase and Mr. Minoru Kaneda for their helpful discussion in this work and encouragements in the student life. I would like to show my thanks to Dr. Shigeru Kakuta, Kazuhiro Ueda, and Tatsumi Hirano of Hitachi Ltd. for his helpful advices and encouragements. I would like to show my thanks to Chief in editor of Edit Associates Dr. Rafael Manory for his helpful comments in correcting and improving my English in my papers.

I show my many thanks to Ms. Masae Mogami, Mr. Yoshiro Honda, Mr. Hideaki Yamada, Mr. Mattuie Py, Ms. Sachi Ibuki, Mr. Yasuyuki Yamamoto, Mr. Takafumi Yamanobe, Mr. Yoshinobu Wakamatsu, Mr. Tomoya Hontani for their helpful discussion and mainly creating a smoothing atmosphere in the laboratory.

I would like to express my thanks to Professor Yoichi Kawakami and Assistant Professor Kazunobu Kojima of Kyoto University for their kind advices in the early days of my study. I also would like to express my thanks to Associate Professor Kazutaka Nakamura of Tokyo Institute of

Technology and Professor Masahiro Kitajima of National Defense Academy of Japan for his helpful advices and discussion in the conferences. I would like show my thanks to Professor Kunio Okimura of Tokai University for his kind help for my study with precious sample provision.

I would like to show my thanks to Dr. German Sciaini, Dr. Gustavo Moriena, Dr. Maher Harb, Dr. Cheng Lu, Mr. Hubert Jean-Ruel in University of Toronto and Assistant Professor Mariko Yamaguchi in Nara Institute of Technology for their comments and encouragements for my study and hospitality for my stay in Toronto. I also show my thanks to Mr. Yasuhiro Kato, Takahisa Kou, and Koutaro Shibata of Spectra Physics for his advices and maintainances of the femtosecond laser.

I would like to show my gratitude for Takenaka Ikueikai, scholarship society for their nine-year financial support to my study. I also would like to thank my friends. Finally, I especially thank my mother, sister and brother for their kind care, support and encouragement.

Contents

Chapter 1

Introduction

This study aimed to visualize the molecular dynamics in condensed matter in real time. In the past two decades, ultrafast science has revealed the intriguing nature of nonequilibrium phenomena and states of materials. In this chapter, a brief summary of the phenomena in the femtosecond timescale is presented. The purpose of the study and the structure of this thesis are shown at the end of this chapter.

1.1 Phenomena in the femtosecond timescale

Since the beginnings of modern science in eighteenth century, scientists have discussed phenomena on an atomic basis. [1)] Physicists have discussed phonon movement, phase transition and so on in the perspective of atomic coordinates, and similarly chemists have discussed chemical reactions with molecule models. Recently, biologists have dealt with biological reactions, such as protein foldings, DNA unwinds, and enzymes' reactions with the atomic conformational model. [2, 3)] In this way, scientists have tried to observe phenomena in real space using the great scientific developments of the X-ray and electron diffraction, electron microscope, and atomic probe. However, who observed the reactions of molecules at the atomic basis and in real time? In other words, who was watching their dancing on the stage? It has been necessary to scrutinize the dynamics at the atomic basis and in real time.

First, the question that arose was "When would the first molecular motion occur?" For thermally sampled coordinates, the fastest pair of atoms could move at the speed of sound. To keep things simple, the typical length of chemical bonds and the speed of sound were assumed to be $\sim$1 Åand $\sim$1000 m/s, i.e., it would take about 100 fs for the first atomic event to be invoked. Therefore, it observations with a time-resolution of 100 fs or less

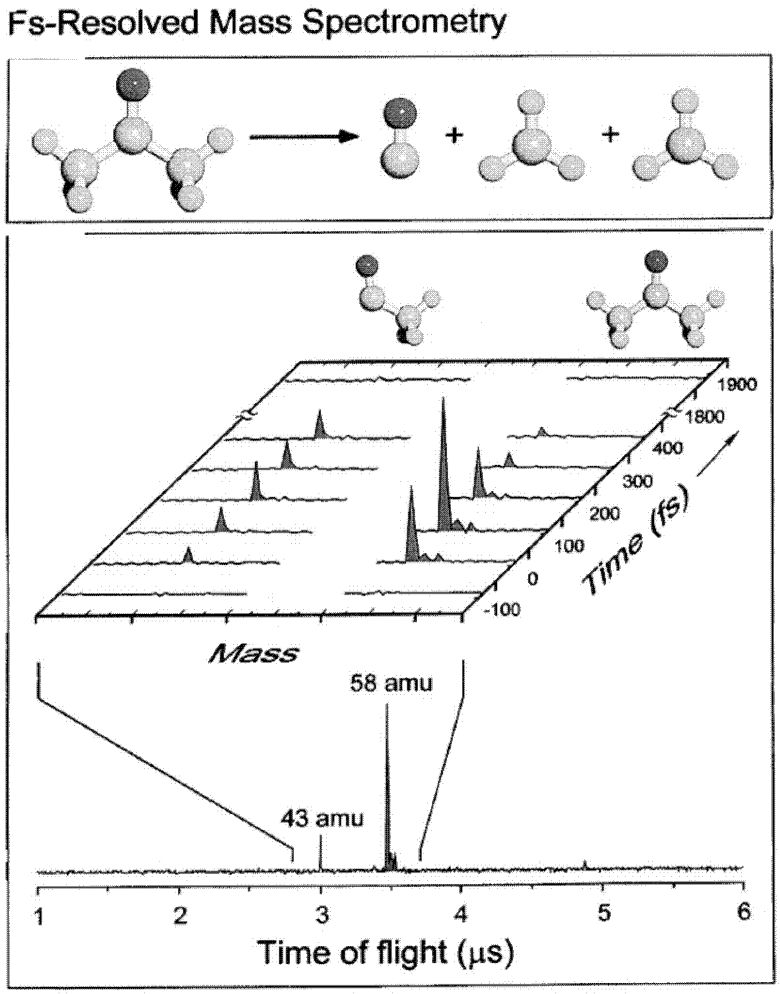

Figure 1.1: The ultrafast disassociation of an acetone molecules in the femtosecond time scale. (A. Zewail et al. [7])

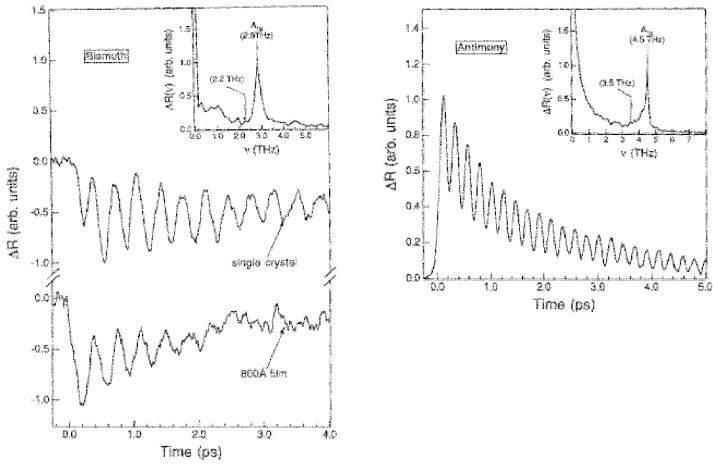

Figure 1.2: Coherent phonon observation on semiconductors with femtosecond optical pump-probe measurement. (H.J. Zeiger et al. [12])

and with spatial-resolution of less than 1 Åis required.

From 1979, Ahmed Zewail started to demonstrate the first time-resolved observation of intramolecular vibrational processes using a molecular beam and a picosecond or femtosecond laser. They performed the observation of disassociation processes in vacuum of isolated molecules such as ICN, NaI, HgI_2, acetone, etc. [4, 5, 6] He was awarded Nobel Prize in chemistry in 1999 for his contribution to femtochemistry. [7] In these experiments, an optical pulse was separated into two pulses named a pump pulse and a probe pulse. The pump pulse generated some kind of excitation or modification in the molecules. After an adjustable time delay controlled with an optical delay line, a probe pulse hit the molecules, and the transmission or ionized fragment molecules were detected as a function of the time delay. Thus, it is possible to obtain information on the decay of the generated excitation, or on other processes initiated by the pump pulse. The multiple step disassociation process of the acetone molecules is shown in Fig. 1.1. The experiments revealed unique molecular behaviors such as coherent vibration, rotation, step-wise disassociation or reactive intermediates in the femtosecond timescale.

In early 1980's, pump–probe spectroscopic experiments on condensed matter such as metals, semiconductors and semimetals have been performed,

and changes in the refractive index of infrared light or visible light of the materials were demonstrated. [8, 9, 10] One of the most representative examples is the coherent phonon in semimetals or semiconductors, demonstrated in the 1990's. [11, 12] The coherent phonon vibrations in single crystalline bismuth and antimony are shown in Fig. 1.2. The experiments successfully captured the intermediate states in condensed matter, which could not be explained with the existing statistical mechanics. The mechanism of the coherent phonon vibration (impulsive stimulated Raman scattering model or displacive excitation of the coherent phonon model) has continued to be studied and discussed for more than twenty years. [12, 13] In these experiments, however, the infrared and visible light used to probe the dynamics inherently cannot resolve atomic-scale features because the lights mainly interact with valence and free electrons and not with the deeper lying core electrons and nuclei that most directly indicate structure. Hard X-ray or electrons, the wavelengths of the same order as the interatomic distance (∼1 Å) would be suitable for the measurement of molecular dynamics.

1.2 Ultrafast time-resolved crystallography

The electric changes associated with the chemical process can be measured by the ultrafast time-resolved spectroscopy; however, the accompanying structural rearrangements have been difficult or impossible to be observed. Unlike the spectroscopic methods, time-resolved X-ray diffraction methods make it possible to directly observe the structural dynamics. Since the end of 1990's, the time-resolved X-ray diffraction measurements have shown the potential to probe the atomic motion in the nanosecond to femtosecond timescale, and several X-ray studies of fast dynamics have been reported. In the time-resolved X-ray diffraction measurements, the photo-excited samples by the optical pump pulses were characterized with diffraction methods using adjustable time delay controlled X-ray pulses.

Several techniques have emerged for generating such an ultrafast X-ray probe. Extremely high-intensity synchrotron X-rays at the pulse duration of ∼50 ps have been used for time-resolved measurements of semiconductors, phase-transition materials and even photo-sensitive proteins. [14, 15] X-ray pulses of 100–300 fs duration have been generated by the scattering of femtosecond laser pulses on synchrotron relativistic electron bunches. [16, 17] There is a completely different laboratory-based X-ray generating method. When an ultrashort laser pulse is focused onto a solid surface, plasma is produced on the surface. Kα X-rays are emitted where the electrons in the

plasma react with the atoms in the solid. [18] The theory indicated that X-ray pulses of less than 100 fs might be obtained with this laser-produced plasma technique.

In 1997, C. Pischel et al. [19] reported the first femtosecond time-resolved X-ray diffraction with laser-produced plasma technique on a laser-heated cadmium-doped organic film. The well-known work of the ultrafast time-resolved X-ray diffraction measurement by C. Rose-Petruck et al. in 1999 is shown in Fig. 1.3. [20] Changes in intensity and peak position of diffraction lines were observed for single crystalline gallium arsenide (GaAs), and indicated that lattice expansion and atom disordering were simultaneously induced in the superheated GaAs crystal in the femtosecond time scale. Since then, several femtoseond X-ray diffraction measurements have been performed and revealed the intriguing nature of structural dynamics, such as nonthermal melting, acoustic and optical coherent phonon in semimetals, semiconductors and superlattice, and photo-excited phase transitions in phase-change materials and superconductors. [21, 22, 23, 24, 25] However, the utilization of such ultrafast time-resolved X-ray diffraction measurements has been limited because of the complexity of huge facilities or the difficulty of managing large high-power lasers and vacuum systems. The ultrafast pulse X-ray sources needed to be more compact and easier to access.

In parallel, there is another different stream of ultrafast crystallography; femtosecond time-resolved electron diffraction measurements have been reported by R.J.D. Miller et al. in the 2000's. [26, 27, 28] The time-resolved electron diffraction, which can be assembled in a tabletop manner, is also a powerful tool for direct atomic motion observation in condensed matter. The most important features of the electron would be the high interaction cross-section and the shorter wavelength. Compared with X-ray, electron has $\sim 10^4$ higher scattering cross-section with the electrons surrounding atoms; therefore fewer electrons are required to obtain an image of the diffraction pattern. [29, 30] The De Broglie wavelength of an electron at $\sim$100 keV is $\sim$0.1 Å, which is much shorter than the copper characteristic X-rays ($\sim$1 Å). This feature makes it possible to obtain dozens of low-to-high ordered diffraction spots at one time; however, it reduces the spatial resolution to about 1 Å(X-ray diffraction: $<$0.1 Å). [28] Several time-resolved electron diffraction measurements in reflection and transmission manner on samples of semiconductors, semimetals and photosensitive phase transition materials have been reported.

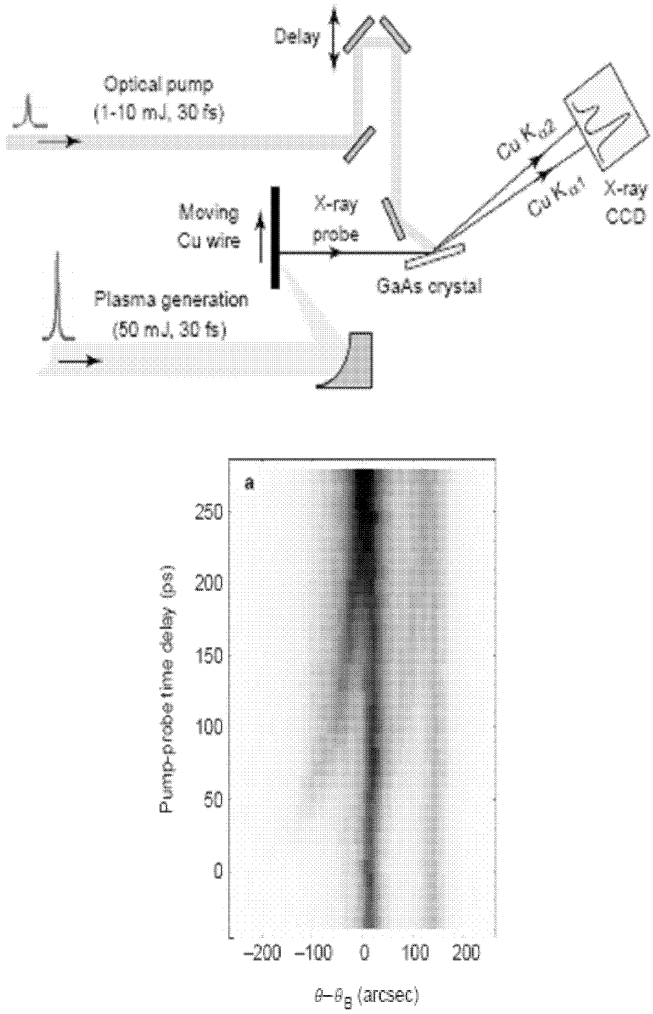

Figure 1.3: Acoustic coherent phonon in a semiconductor observed with the time-resolved X-ray diffraction method. (C. Rose-Petruck et al. [20])

1.3 Purpose of study and structure of the thesis

This thesis aims to develop a high-intensity and compact–designed X-ray source with a tabletop femtosecond laser and to reveal the atomic dynamics in solid materials irradiated with an optical pulse by using the ultrafast time-resolved X-ray diffraction measurement. We reported the first direct observation of photothermal atomic motion in a single crystal cadmium telluride and insulator–metal phase transition in vanadium dioxide with a tabletop time-resolved X-ray diffractometer.

In Chapter 2, fundamental studies for the femtosecond lasers and the optical pump–probe measurements are described. The basic optical pump–probe measurements on reversible and irreversible phenomena are introduced.

To achieve ultrafast time-resolve X-ray diffraction measurements, extremely short ($\sim$100 fs) pulsed X-ray is required. In Chapter3, femtosecond pulsed X-ray radiation by laser-produced plasma is discussed. The interaction between the electrons in laser-produced plasma and the ambient atoms is also explained with a simple collision model.

In Chapter 4, ultra-fast time-resolved X-ray diffraction measurements on a single crystal semiconductor (CdTe) and ultrathin film of metal–insulator phase transition material (VO_2) are described. In this experiment, the superheated transition state of the VO_2 was observed in the $\sim$10 picosecond time scale.

Finally, Chapter 5 presents a summary of this study. Time-resolved crystallography has revealed the intriguing nature of molecular dynamics; however, there remained a serious problem. Only the reversible phenomena or phenomena in well crystallized samples could be detected with the existing time-resolved crystallography because of the X-ray or electron intensity or transverse coherence. There are many more irreversible chemical processes and phenomena in hard-to-crystallized materials. The next generation time-resolved crystallography will overcome the problem. In Chapter 5, the next generation time-resolved X-ray and electron diffraction is introduced.

Chapter 2

Femtosecond Laser Science

The mode-locked Ti:sapphire laser (a femtosecond laser) is one of the most important tools for the observation of nonequilibrium phenomena in the femtosecond time-scale. In this chapter we describe the fundamentals of the femtosecond laser and optical pump-probe experiments with femtosecond laser. [31)]

2.1 Fundamental studies of femtosecond laser

The laser emission frequencies are determined by the natural bandwidth of the gain medium (laser crystal) and the longitudinal modes of the optical cavity, as shown in Fig. 2.1. In the simplest case, the two flat mirrors face each other, surrounding the gain medium of the laser. The laser light is generated or amplified in the gain medium, while the light rays bounce between the mirrors leading to formation of standing waves in the cavity. These standing waves are a discrete set of frequencies which are called "the longitudinal modes of the cavity". The frequency separation between any two adjacent modes ($\Delta\nu$) is given with the cavity length;

$$\Delta\nu = \frac{c}{2L}, \tag{2.1}$$

where c is the speed of light.

In a simple laser, each of the modes oscillates independently, i.e., the individual phase of the light waves in each mode varies randomly, mainly because of the thermal effects in the materials of the laser. [32)] By installing an acousto-optic modulator or a saturable absorber into the laser cavity, the modes of the laser can periodically interfere with one another and the phase of the light waves in each mode can be fixed. This phase-fixing process is called "mode-locking". Such the mode-locked lasers produce intense bursts or pulses of light. [33, 34, 35, 36)]

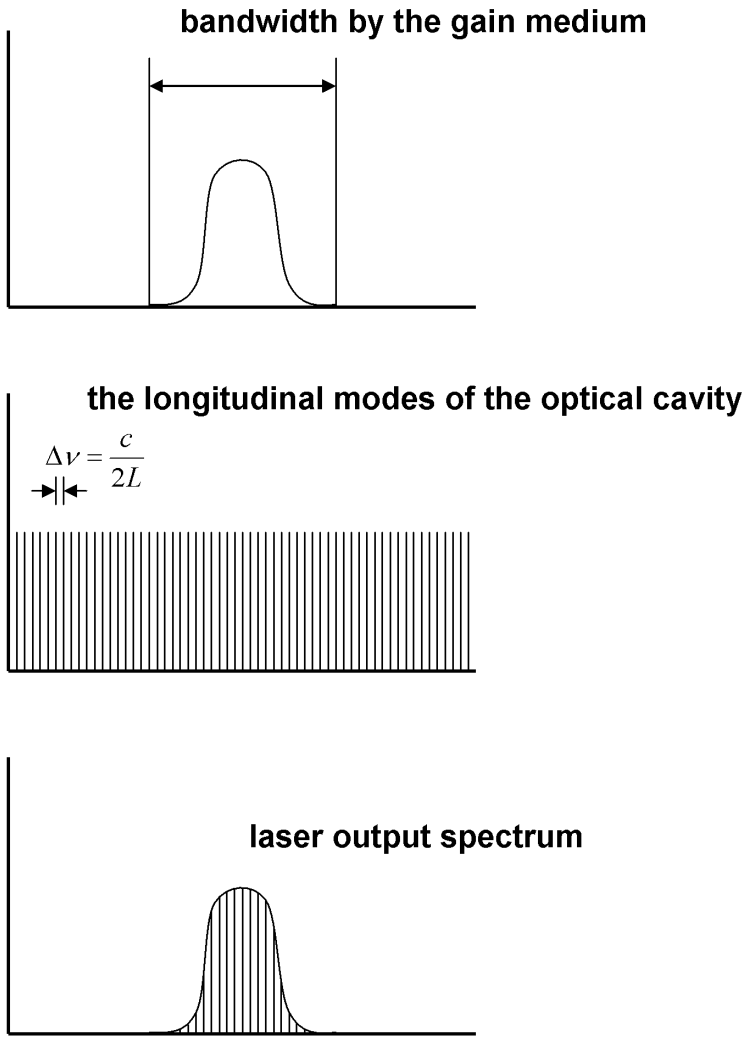

Figure 2.1: The laser emission frequencies with the natural bandwidth and the longitudinal modes of the optical cavity

The fundamental relationship between the pulse duration and the bandwidth of the Gaussian mode-locked laser pulse is given by the simple Fourier transformation as:

$$\Delta\nu \cdot \Delta t \sim 0.441, \tag{2.2}$$

where Δt is the laser pulse width. This means that a very short pulse exhibits a broad bandwidth, and vice versa. The value 0.441 is known as the "time-bandwidth product" of the pulse, and varies depending on the pulse shape. For ultrashort pulse lasers, a $\mathrm{sech}^2(t)$ pulse shape is assumed, giving a time-bandwidth product of 0.315. [37] For example, for a 110 fs pulse at $\lambda = 800$ nm, the corresponding bandwidth is about 12 nm.

Ti:sapphire is a crystal produced by introducing Ti_2O_3 into a Al_2O_3, where Ti^{3+} ions replace a small percentage of the Al^{3+} ions. The Ti^{3+} ions are responsible for the lasing action in Ti:sapphire. [38, 39, 40, 41] The electronic ground state of the Ti^{3+} ion is split into a pair of vibrationally broadened levels as shown in Fig. 2.2. Absorption transitions occur in a broad range of wavelengths, in the range 400–600 nm, and fluorescence transitions occur from the lower vibrational levels of the excited state to the upper vibrational levels of the ground state (600–1000 nm). The bandwidth in the lasing action is generally tuned around 720–850 nm because of the interference of the absorption transitions, mirror coating, turning element losses, atmospheric (oxygen or water vapor) absorption, and pump power and pump mode quality.

Chirped pulse amplification (CPA) is used for the amplification of the femtosecond laser pulse from the mode-locked Ti:sapphire laser, because an intense beam traveling through a Ti:sapphire crystal can induce permanent damage to the crystal. [42, 43] It is necessary to limit the peak power of a pulse in this crystal to less than 10 GW/cm^2; however, CPA enables a Ti:sapphire crystal to be used for amplified pulses beyond this peak power. CPA is accomplished in three steps. In the first step, the femtosecond seed pulse is stretched and its peak power is reduced, which gently reduces the probability of damage to the Ti:sapphire amplifier crystal. Devices such as a prism-pair, diffraction-grating-pair, or multi-layer mirrors that can delay certain a wavelength relative to others can stretch or compress a short pulse. The phenomenon of delaying or advancing some wavelengths relative to others is called Group velocity dispersion (GVD) or chirp. A pulse has positive GVD (or chirp) when the shorter wavelength leads the longer wavelength. Conversely, when the shorter wavelength is delayed more than the longer wavelength, it has negative GVD. The second step amplifies the stretched

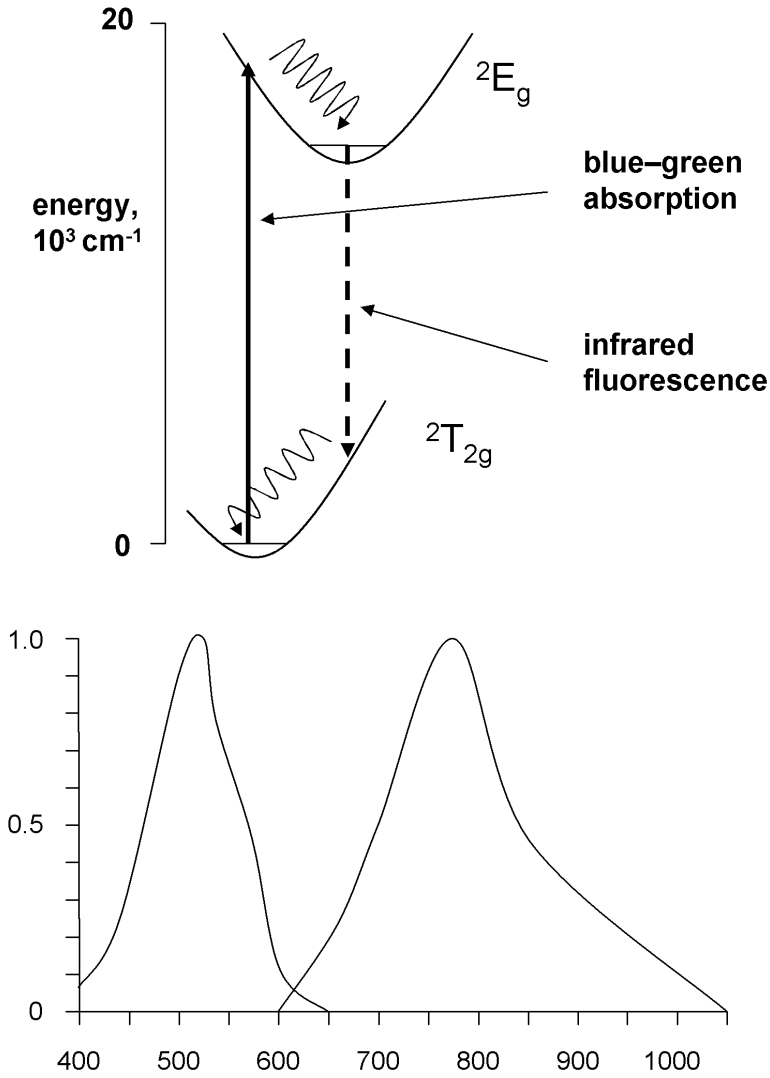

Figure 2.2: Absorption and emission spectra of Ti:sapphire

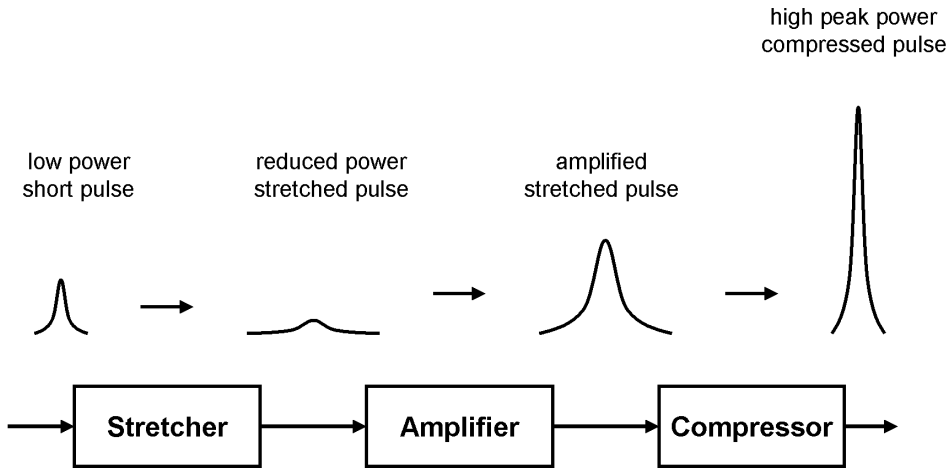

Figure 2.3: The principle of chirped pulse amplification

pulse: a pump laser provides a synchronous energy pulse to the Ti:sapphire crystal to excite it just prior to the arrival of the stretched seed pulse. The seed pulse causes stimulated emission, which amplifies the pulse at the same wavelength and direction. The third step recompressed the stretched and amplified pulse to its original pulse duration with a negative GVD diffraction-grating pair. Figure 2.3 shows schematically this process.

2.2 Femtosecond laser system

The femtosecond laser system was assembled with a diode-pumped cw (continuous wave) visible laser (Millennia Pro 5sf/ Spectra-Physics), a mode-locked Ti:sapphire laser (Tsunami/ Spectra-Physics), an intracavity-doubled diode-pumped Nd:YLF laser (Empower/ Spectra-Physics), and a Ti:sapphire regenerative amplifier (Spitfire Pro XP/ Spectra-Physics). [44] Figure 2.4 is the photo of the femtosecond laser system, and the schematic setup of the laser system is shown in Fig. 2.5. A brief explanation of the working principles of these lasers is mentioned in this section.

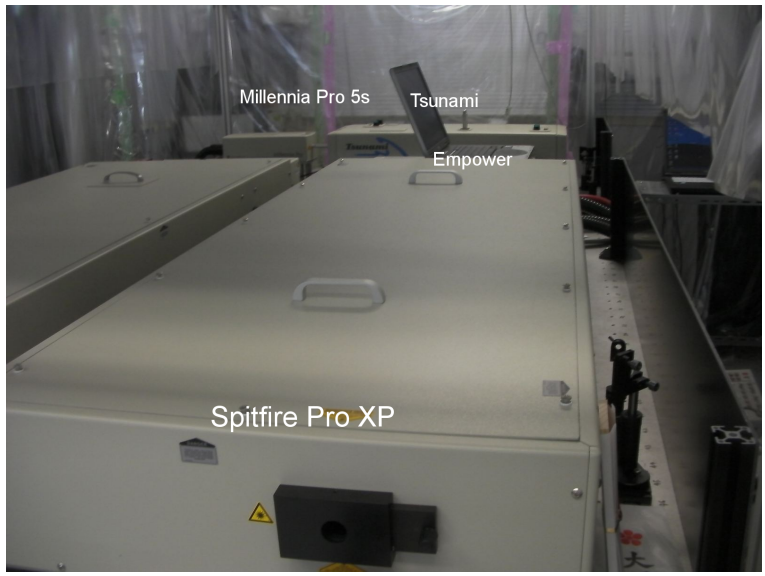

Figure 2.4: Photograph of the femtosecond laser system

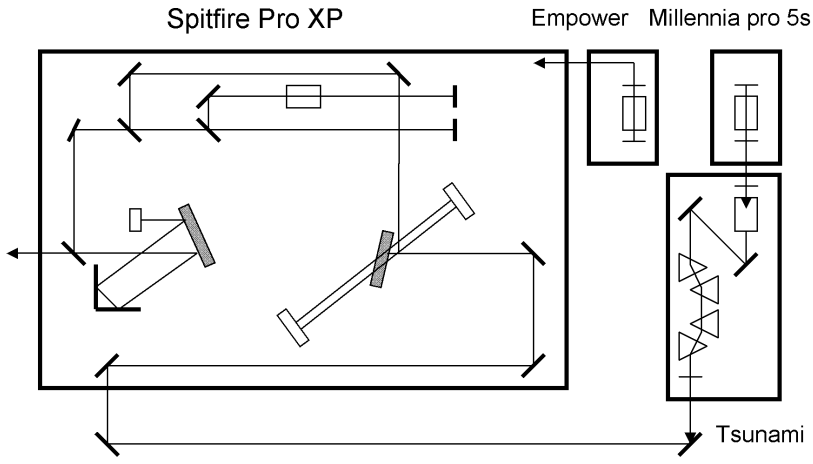

Figure 2.5: Schematic drawing of the femtosecond laser system

2.2.1 Mode-locked Ti:sapphire laser

Figure 2.6 shows a schematic drawing of the diode-pumped cw visible laser and the mode-locked Ti:sapphire laser.

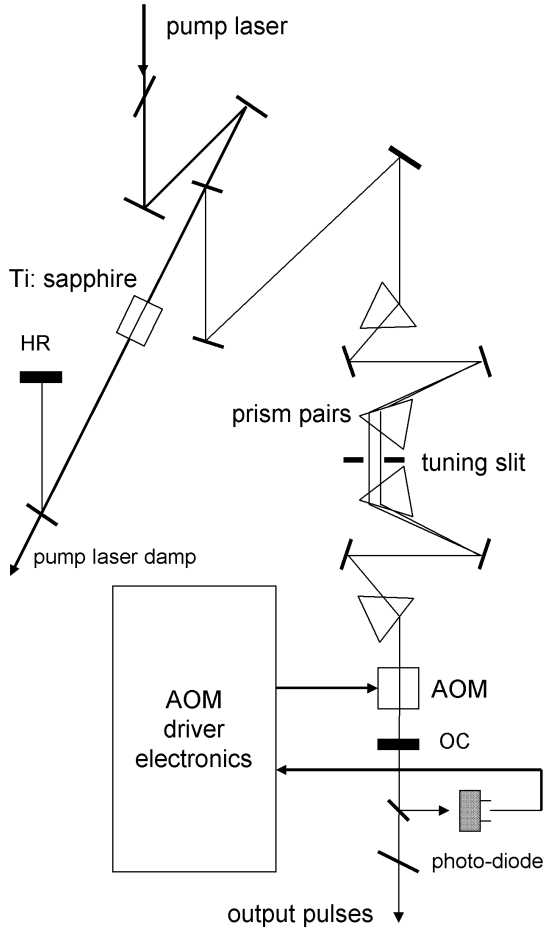

Figure 2.6: Schematic drawing of the mode-locked Ti:sapphire laser (Tsunami)

The diode-pumped cw visible laser emitting continuous 532 nm optical wave was used for excitation of a Ti:sapphire crystal in the mode-locked Ti:sapphire laser.

The mode of operation is as follows. The diode pump laser excites the Nd:YVO_4 crystal and emits an infrared laser beam at 1064 nm in the diode-pumped cw visible laser cavity. Frequency-doubling lithium triborate (LBO) crystal converts the 1064 nm light from the laser crystal to the green light with 532 nm wavelength. The intensity of the output of the laser is 5.00 W. The green 532 nm light excites the Ti:sapphire crystal in mode-locked Ti:sapphire laser which generates a broadband optical wave at the medium wavelength of 800 nm (794–806 nm). The broadband optical wave has to be mode-locked with an acousto-optic modulator (AOM) in the laser cavity. The AOM ensures normal mode-locked operation at about 80 MHz. The output intensity of the mode-locked Ti:sapphire laser was 700 mW. The pulse duration of the pulses from the mode-locked Ti:sapphire laser were compressed into about 100 fs with two prism-pairs.

2.2.2 Ti:sapphire regenerative amplifier

Figure 2.7 shows the schematic drawing of the Ti:sapphire regenerative amplifier (Spitfire Pro XP). This device amplifies individual laser pulses selected from a stream of pulses produced by the mode-locked Ti:sapphire laser (Tsunami). The intracavity-doubled diode-pumped Nd:YLF laser (Empower) emits 20 mJ optical pulses at a wavelength of 527 nm in the Q-switch method and latter pulses are used to excite the Ti:sapphire crystal of the regenerative amplifier. The Ti:sapphire regenerative amplifier consists of a positive GVD diffraction-grating pair for pulse extension, a Ti:sapphire crystal for amplification and a negative GVD diffraction-grating-pair for pulse compression.

A femtosecond optical pulse from the mode-locked Ti:sapphire laser is stretched into 1 ns by the positice GVD diffraction-grating-pair and focused onto the excited Ti:sapphire crystal in the cavity of the Ti:sapphire regenerative amplifier. An amplified broadband optical pulse is generated through the stimulated radiation, and output from the cavity by changed the polarization with Pockels cells. The amplified broadband optical pulse was compressed with the negative GVD diffraction-grating-pair into about 130 fs. The output intensity of the Ti:sapphire regenerative amplifier was about 3.5 mJ/pulse with the repetition rate of 1 kHz.

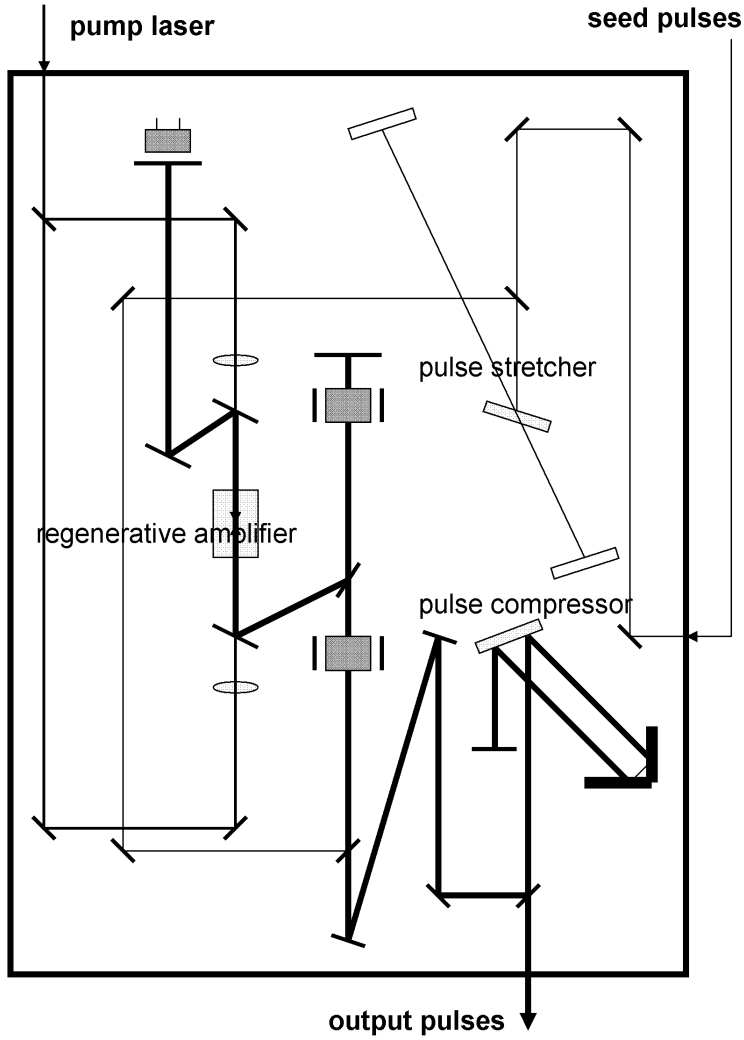

Figure 2.7: The schematic drawing of the regenerative Ti:sapphire laser amplifier (Spitfire Pro XP)

2.3 Optical pump-probe measurements

The development of ultrafast optical technology enables us to measure phenomena in the femtosecond time-scale. We constructed an ultrafast pump-probe spectrum system using the femtosecond laser. In pump-probe measurements, pump pulses are first focused onto the sample surface and induce observable physical phenomena such as lattice vibration or phase transition. In the second stage, the probe pulses having passed through an optical delay line are focused onto the same spot ofn the sample surface. The phenomena were observed by the changes in optical refractive index of the reflected light of the probe pulse. In this section, we present optical pump-probe measurements of the lattice vibration in a bismuth film (repeatable reversible reaction) and the ultrafast liquid-to-solid phase transition in silicon (irreversible reaction).

2.3.1 Autocorrelation function method for the ultrafast laser pulse

The pulse duration of the femtosecond laser is one of the most important parameters for pump-probe measurements. However, the duration of the femtosecond optical pulse cannot be measured with a set of a high-speed photo-diode and an oscilloscope because the time-resolution of the electronic device is at most 1 ns. The autocorrelation function method is generally used to measure the femtosecond pulse duration. [45, 46, 47] The fundamentals for the autocorrelation are described in this section and the autocorrelation function method was demonstrated to measure the pulse duration of the femtosecond laser pulse and also to determine the position of time-zero between the pump pulse and probe pulse in the optical time delay line.

A femtosecond laser pulse can be described as a function of $\mathrm{sech}^2(t)$ as shown in Fig. 2.8. The intensity of the optical pulse I is proportional to the square of the electric-field E; therefore, the optical pulse $I(t)$ as a function of time can be expressed by the following equation:

$$I(t) = \int_{-\infty}^{+\infty} \mid E(t) \exp i(\omega t + \Phi t) \mid^2 dt, \tag{2.3}$$

where, ω and Φ are the angular frequency from the wavelength and pulse duration of the femtosecond laser, respectively.

In order to obtain the autocorrelation function, two optical pulses with the same intensity, wavelength and pulse duration are mixed in a nonlinear crystal, and generate a second harmonic wave. The time separation of the

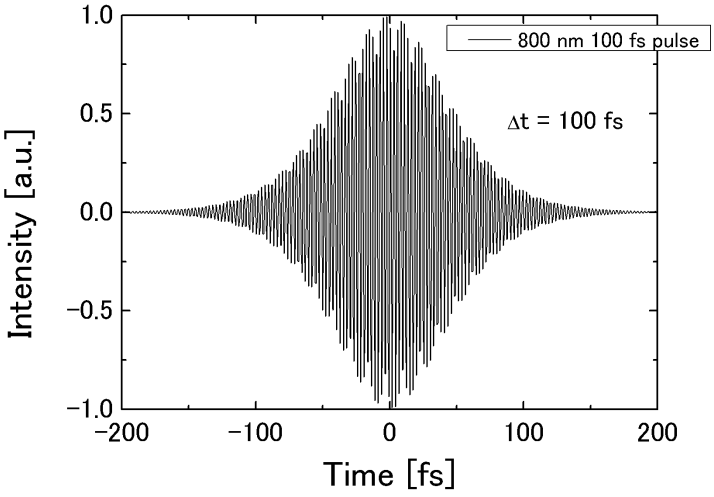

Figure 2.8: A femtosecond laser pulse described as the function of $\mathrm{sech}^2(t)$

two pulses is defined as τ. The intensity of the second harmonic wave can be expressed with the convolution of the two pulses; therefore,

$$G(\tau) = \int_{-\infty}^{+\infty} \mid \{E(t)\exp i(\omega t + \Phi t) + E(t-\tau)\exp i[\omega(t-\tau) + \Phi(t-\tau)]\}^2 \mid^2 dt, \qquad (2.4)$$

$$G(\tau) = \int_{-\infty}^{+\infty} \mid 2E^4(t) + 4E^2(t)E^2(t-\tau) + 4E(t)E(t-\tau)[E^2(t) + E^2(t-\tau)]\cos[\omega\tau + \Phi(t) - \Phi(t-\tau)] + 2E^2(t)E^2(t-\tau)\cos\{2[\omega\tau + \Phi(t) - \Phi(t-\tau)]\} \mid dt. \qquad (2.5)$$

When the time separation τ is much longer than the pulse duration, the two pulses cannot be mixed in the nonlinear crystal and the second harmonic generation occurs separately. The intensity of the autocorrelation function $I_2(\pm\infty)$ is expressed as,

$$G(\pm\infty) = 2\int I^2(t)dt. \qquad (2.6)$$

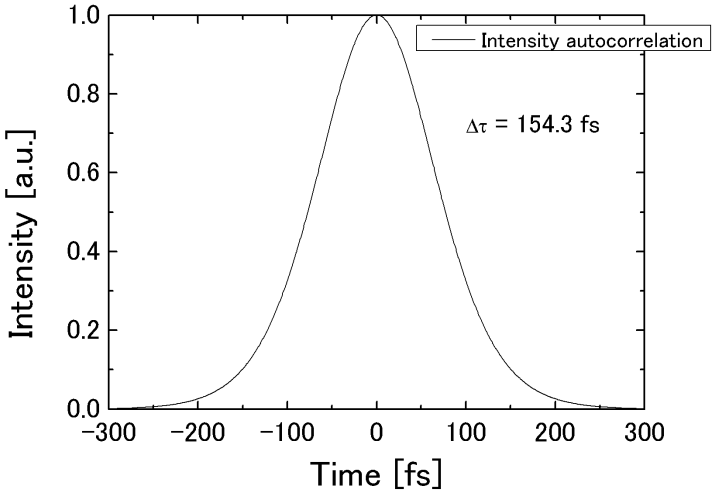

Figure 2.9: The autocorrelation function of a femtosecond laser pulse at the pulse duration of 100 fs.

When the separation time between the two pulses is zero (time-zero), the intensity of the autocorrelation function $G(0)$ can be calculated as;

$$G(0) = 2^4 \int I^2(t)dt = 8G(\pm\infty). \tag{2.7}$$

The function of the optical pulse intensity $I(t)$ is $\mathrm{sech}^2(t)$; therefore, the autocorrelation function can be reduced to the following equation:

$$\begin{aligned} G(\tau) = \int_{-\infty}^{+\infty} \mid & 2\mathrm{sech}^4(t,\Phi) + 4\mathrm{sech}^2(t,\Phi)\mathrm{sech}^2(t-\tau,\Phi) \\ & +4\mathrm{sech}(t,\Phi)\mathrm{sech}(t-\tau,\Phi)[\mathrm{sech}^2(t,\Phi) \\ & +\mathrm{sech}^2(t-\tau,\Phi)]\cos\omega\tau \\ & +2\mathrm{sech}^2(t,\Phi)\mathrm{sech}^2(t-\tau,\Phi)\cos 2\omega\tau \mid dt. \end{aligned} \tag{2.8}$$

The intensity of the autocorrelation function as a function of time is shown in Fig. 2.9. The pulse duration of the autocorrelation function reflects that of the convolution of the two pulses; therefore, the autocorrelation function should be deconvoluted to obtain the pulse duration. When the laser intensity (I) and the full width half maximum (FWHM: Δt) are defined

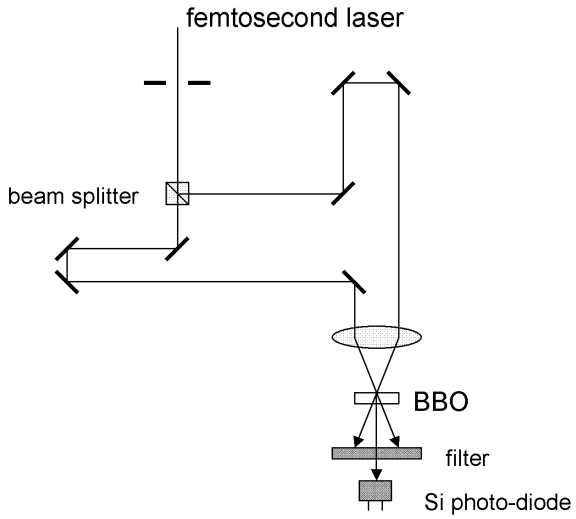

Figure 2.10: The experimental setup for the autocorrelation function method.

as $I(t) = \mathrm{sech}^2(t)$ and $\Delta t = 1.763$ respectively, the autocorrelation function can be expressed as a simple equation as follows;

$$G(\tau) = \frac{\int I(t)I(t-\tau)}{|\int I^2 dt\ |} = \frac{3[\tau\cosh(\tau) - \sinh(\tau)]}{\sinh^3(\tau)}. \tag{2.9}$$

The FWHM of the autocorrelation function ($\Delta\tau$) can be calculated to be 2.720; therefore the relation equation of $\Delta\tau/\Delta t = 1.543$ in the pulse duration is obtained.

Figure 2.10 shows the experimental setup for the autocorrelation function method for measurements of pulse duration. A femtosecond laser pulse at the wavelength of 800 nm is split into two pulses os same intensity with 1:1 cubic beam splitter. The reflected light at the beam splitter was focused on the Beta-Barium Borate (BBO) nonlinear crystal with an achromatic lens. The transmitted light was passes through an optical delay line and is focused onto the same spot in the BBO crystal. According to the autocorrelation function theory, the sum frequency (wavelength: 400 nm) pulse is generated when the pulse separation time between the two pulses (τ) is around zero. The sum frequency pulses were passed through the filter which entirely absorbs 800 nm light and were detected with a photodiode. The autocorrelation function of the femtosecond laser (Spitfire Pro XP) is shown

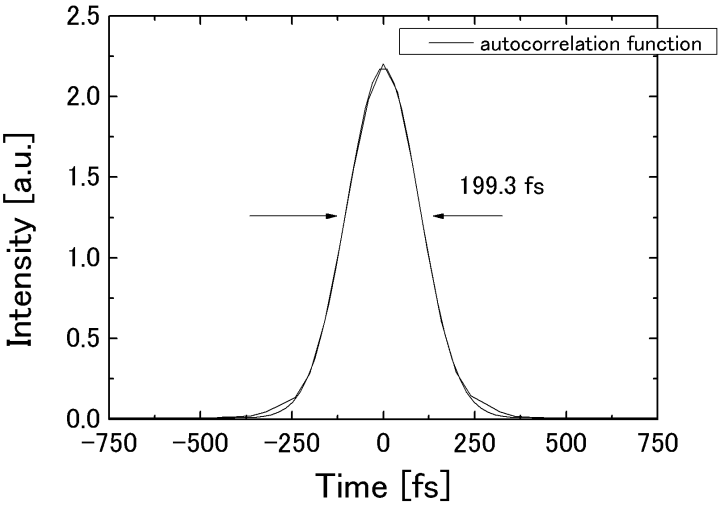

Figure 2.11: The autocorrelation function of the femtosecond laser (Spitfire Pro XP/ Spectra Physics).

in Fig. 2.11. The FWHM of the autocorrelation function was about 200 fs; therefore the pulse duration of the femtosecond laser was determined to be about 130 fs.

2.3.2 Observation of bismuth A_1g coherent phonon

A coherent phonon in bismuth is one of the most representative phenomena in femtosecond time-scale.[11, 12] In this section, we report on repeatable optical pump-probe measurements for the observation of phonon vibration in femtosecond time scale.

Figure 2.12 shows the experimental setup for pump-probe measurements of optically induced reflectivity changes. A mode-locked Ti:sapphire laser generated femtosecond laser pulses at a central wavelength of 780 nm. The repetition rate of the laser pulse was 80 MHz and the pulse duration was about 120 fs. The output laser pulse was split into a strong pump pulse and a weaker probe pulse. The repetition of the pump pulse was modulated into 1 kHz using an optical chopper, and the pump pulse was focused onto a bismuth thin film sample to induce coherent phonon vibration. The laser fluence to excite the sample was about 0.7 mJ/cm^2. The probe pulse passed

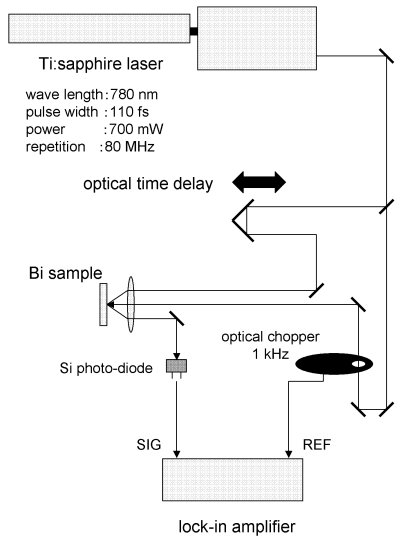

Figure 2.12: The experimental setup for pump-probe measurements of optically induced reflectivity changes.

through an optical delay line and was focused onto the same spot on the sample surface. The reflected light of the probe pulse was detected with a photo-detector. The signal modulated as 1 kHz was selectively detected by the lock-in-amplifier. The optical delay line caused a time delay of -1 ps to $+10$ ps between the pump pulse and probe pulse with the position of the motorized stage. The reflectivity change (ΔR/R) in the probe pulse was measured as a function of the delay time between the two pulses. The time-zero was determined with the autocorrelation function method described in the previous section. The bismuth film was deposited onto a single-crystal silicon substrate. The thickness of the bismuth film was measured to be about 300 nm using a stylus profilometer (ULVAC Dektak3).

The time evolution of the reflectivity after excitation by the pump pulse is shown in Fig. 2.13. As shown in the magnified view in Fig. 2.13, the reflectivity changes as a function of the times. Figure 2.14 is the Fourier transform of the pump-probe data in Fig. 2.13. The frequency of the oscillation in Fig. 2.14 was 2.9 $\pm$ 0.1 THz and agreed well with the A_{1g} mode phonon frequency (2.93 THz) obtained through spontaneous Raman scattering in bismuth.[48] The reflectivity changes during 1–10 ps can be considered as a coherently excited phonon oscillation (coherent phonon).

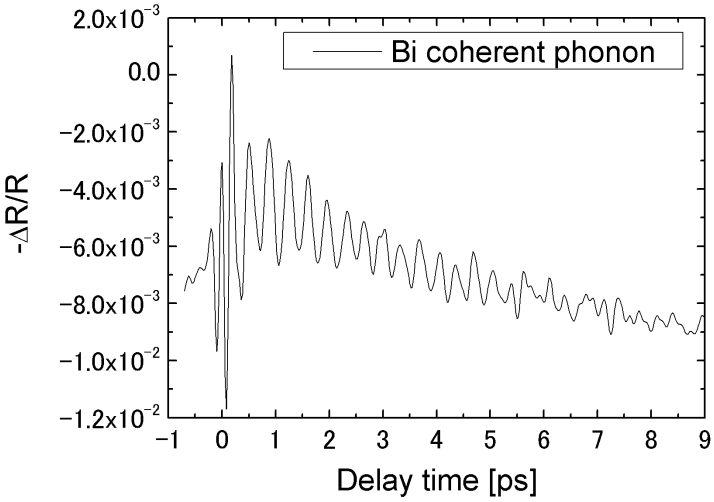

Figure 2.13: The reflectivity changes in bismuth thin film as a function of the delay time

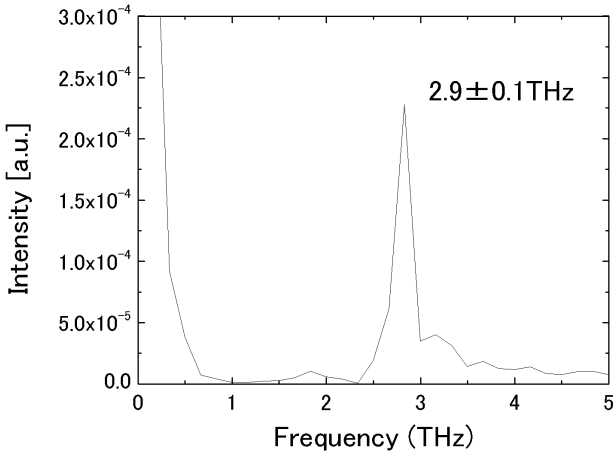

Figure 2.14: The Fourier transform of the pump-probe data

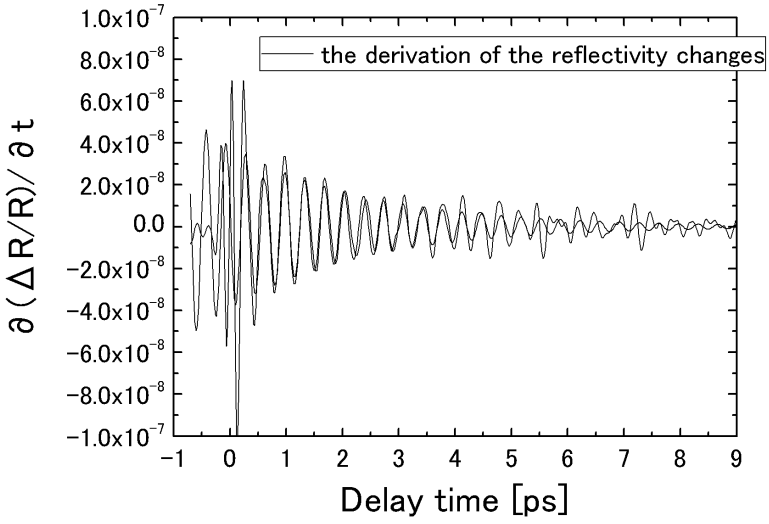

Figure 2.15: The time derivation of the reflectivity changes

The reflectivity changes shown in Fig. 2.13 can be decomposed into two parts: a dephasing oscillatory part due to excitation of the coherent phonon, and a damping background as a result of the Debye–Waller thermal effect. The damping background part is much slower than the dephasing coherent phonon oscillation; therefore the de-phasing oscillation part can be obtained by the derivation of the reflectivity changes with time, as shown in Fig. 2.15. In general, the coherency of the coherent phonon diminishes through the random atomic movements, which occurs with the thermal coupling of the coherent phonon. The decay constant of the coherent phonon shown in Fig. 2.15 was about 3.1 ps, which was corresponded well with the results obtained by M. Hase et al. [49, 50] We performed the wavelet analysis on the derivative of the reflectivity changes to examine the frequency shift of the coherent phonon oscillation in detail, as shown in Fig. 2.16. In Fig. 2.16, the frequency of the coherent phonon stayed constant in the interval 0–5 ps, which suggested that the potential surface of the coherent phonon was harmonic at this excitation level. M. Hase et al. showed that the potential surface of the coherent phonon took the function of anharmonic at a more higher excited level (7.6 mJ/cm^2). [51]

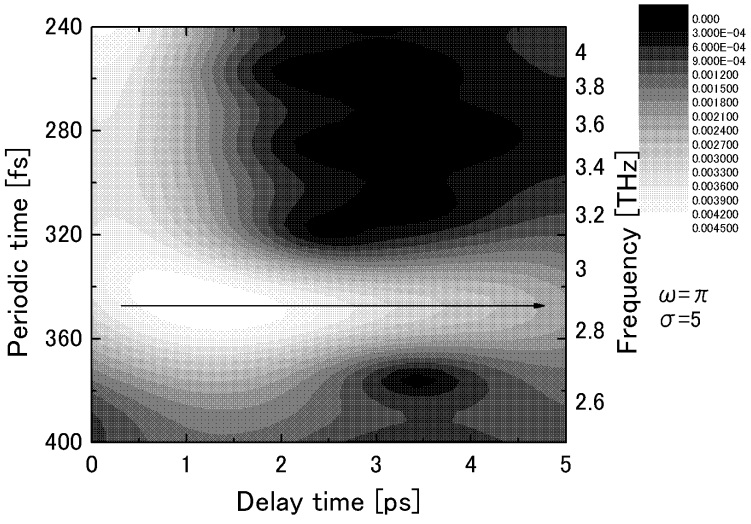

Figure 2.16: The wavelet transform of the reflectivity changes

2.3.3 Observation of ultrafast melting in silicon

Semiconductor silicon, is widely used in large scale integrated circuits, and has been studied extensively. In optoelectronics and display technology, the silicon annealing process with melting has attracted much attention. In this section, we report on single-shot optical pump-probe measurements for the ultrafast phase change of silicon in the femtosecond time scale.

Figure 2.17 shows the experimental setup for pump-probe measurements of optically induced reflectivity changes. A mode-locked Ti:sapphire laser generated femtosecond optical pulses of about 130 fs duration and these pulses were amplified at about 2 mJ per pulse through a regenerative amplifier with a repetition rate of 10 Hz. The output pulse from the regenerative amplifier was split into a strong pump pulse and a weaker probe pulse. The *s*-polarized pump pulse passed through an optical delay line and was focused onto the n-doped Si (100) single crystal sample surface with a 25° incident angle. The *p*-polarized probe pulse was focused onto the same spot on the sample surface with a 70.7° incident angle. A different position on the sample was used for each shot of the laser pulse. The time delay between pulses was varied from −2 ps to +1 ns to measure reflectivity change as a function of the time between pulses. Figure 2.18 shows the pump and probe pulse

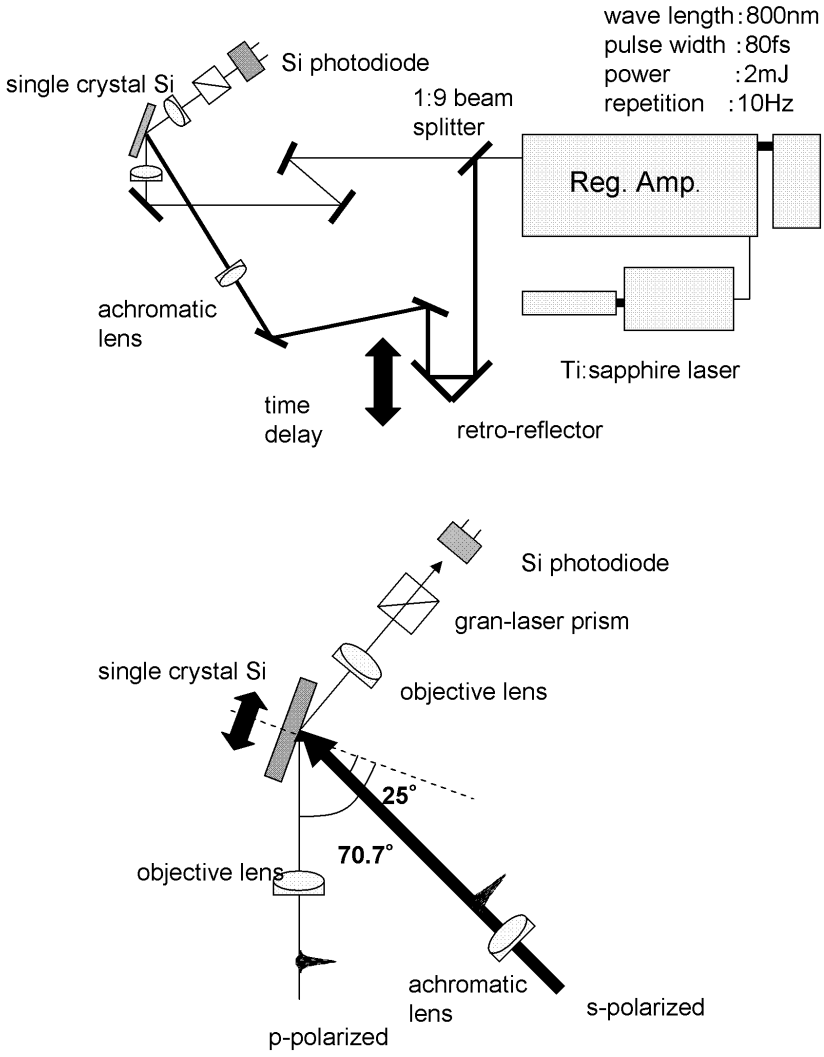

Figure 2.17: The Experimental setup for the single shot pump-probe measurement

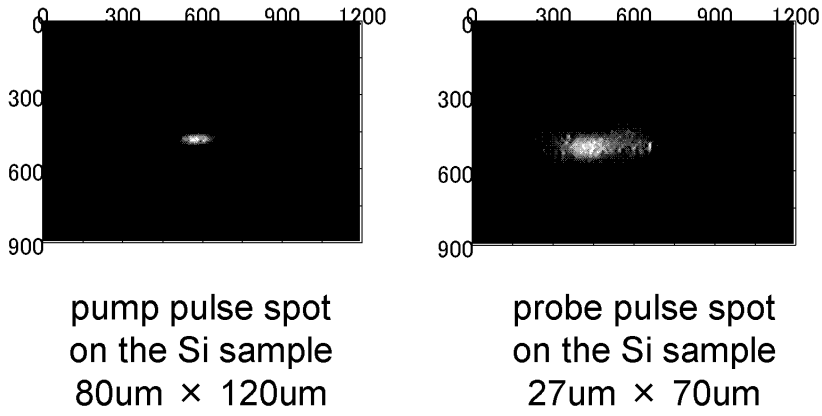

Figure 2.18: Pump and probe pulse spot sizes on the Silicon sample

spots on the Si sample obtained with an infrared CCD microscope. The pump pulse spot size on the Si sample was 80 μm × 120 μm and the probe pulse spot size was 27 μm × 70 μm. The laser fluence for the Si melting threshold was about 170 mJ/cm^2 (Fm), and the pump pulse fluence on the Si sample ware 1.4 or 2.9 Fm. [52)]

The changes in reflectivity with time after irradiation wiht the pumping laser pulse at a fluence of 1.4 Fm are shown in Fig. 2.19. The observed behavior appears to be consistent with the expected behavior of a solid–liquid phase transformation, i.e., an increase in reflectivity. The complex index of refraction for solid Si at 800 nm wavelength is n = 3.7, k = 6.0 × 10^{-3}, and that for liquid Si is n = 3.1, k = 5.2. [53)] Thus, solid Si irradiated by laser pulses changed into liquid Si in the femtosecond time scale, and the liquid phase transformation continued for a few ns. In Fig. 2.19, two distinct stages of transformation, denoted as I and II, can be distinguished. Stage I corresponds to the first a few hundred fs, and a rapid increase in the reflectivity was observed. Stage II is the time period after stage I, and the reflectivity of the Si surface gradually increased for a few ns. In stage I, because of strong nonthermal electron excitation with the ultrafast and high-energy laser pulse, the ultrafast (sub-ps) solid–liquid transformation is considered to have occurred. In stage II, the molten liquid area formed in

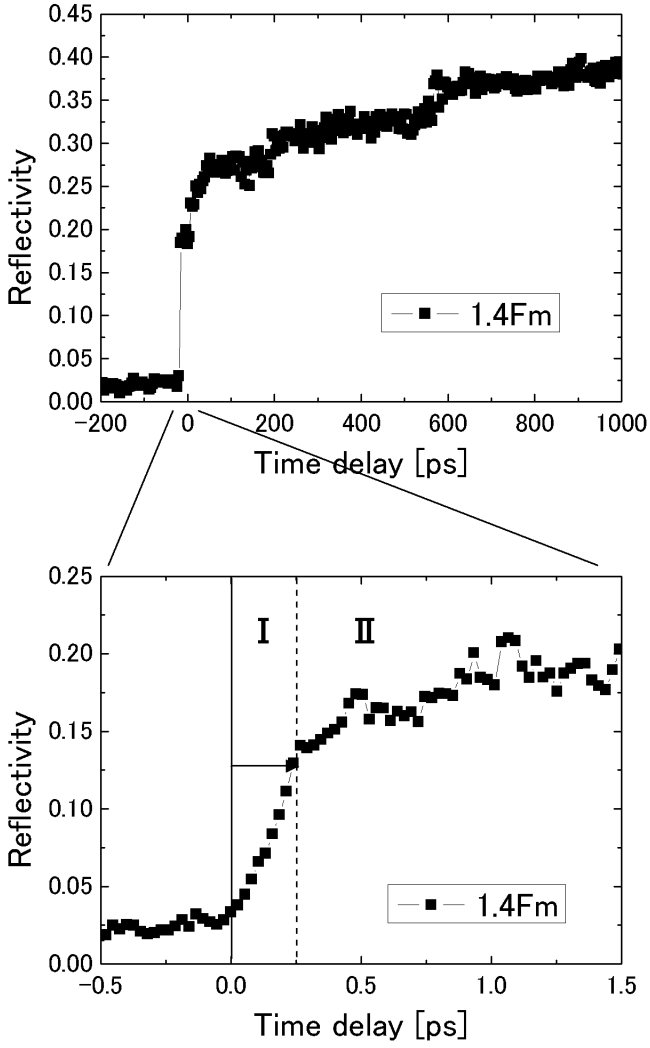

Figure 2.19: Silicon reflectivity changes under 1.4 Fm laser fluence

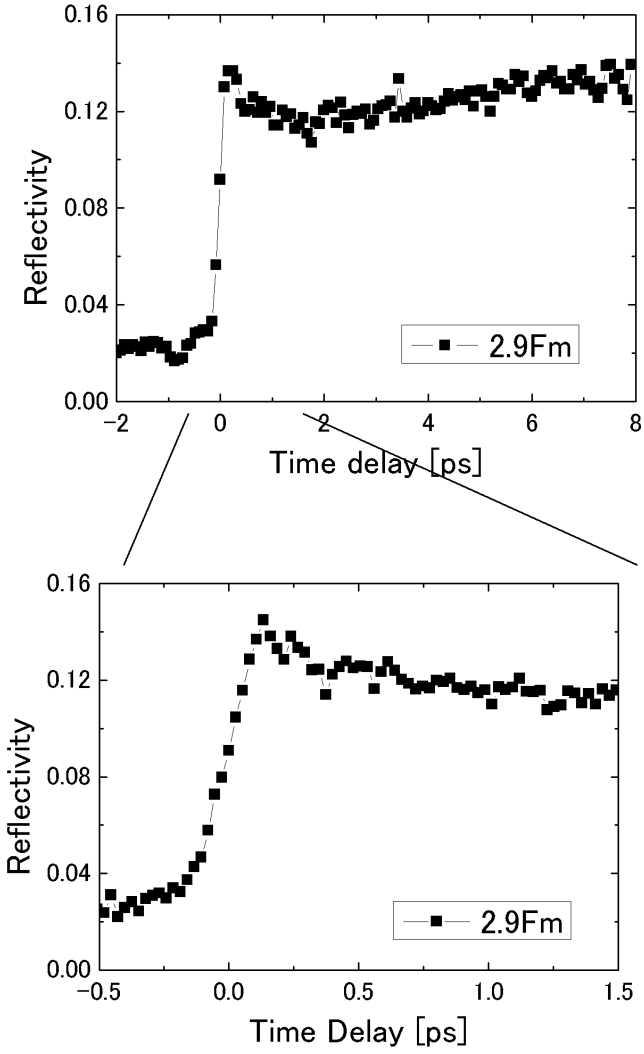

Figure 2.20: Silicon reflectivity changes under 2.9 Fm laser fluence

the stage I is considered to have expanded thermally in the lateral direction. Figure 2.20 shows the reflectivity changes on the Si sample irradiated with 2.9 Fm laser fluence. Only the rapid increase in reflectivity could be obtained here, and no thermal expansion of the liquid area could be observed. Thus, high fluence laser induces the ultrafast solid-liquid transformation over the whole area of the Si surface in a few hundred fs. [54)]

2.4 Summary

In this chapter, the theoretical view of the generation of femtosecond laser pulses was described with the experimental system. The optical pump-probe measurements of the repeatable reversible reaction and the irreversible reaction were also described. The following are summarizing remarks of this chapter.

1. The duration of the optical pulses emitted by the mode-locked Ti:sapphire laser or the regenerative Ti:sapphire amplifier was measured using the autocorrelation function method with a BBO crystal and found to be about 130 fs.

2. The repeatable optical pump-probe measurement was performed for the observation of phonon vibration in bismuth thin film. The frequency of the observed oscillation was 2.9 $\pm$ 0.1 THz which agreed with the A_{1g} mode phonon frequency (2.93 THz) obtained through spontaneous Raman scattering in bismuth.

3. Laser–induced phase transition in silicon was studied by means of single-shot femtosecond time-resolved measurements of the optical reflectivity changes. Nonthermal and thermal phase transformations of Si single crystal solid to metal-like liquid were observed, and these non-thermal and thermal transformations were observed to depend on the intensity of the laser excitation.

Chapter 3

Ultrafast X-ray Radiation in Helium Ambient

The use of hard X-ray from femtosecond laser-produced plasma has gained much interest in the scientific community, because experiments with this unique time-resolved X-ray diffraction method demonstrate and reveal the atomic dynamics of chemical reactions, phase transitions and coherent phonon vibrations. This chapter provides the mechanism of the ultrafast X-ray generation, and also the possibility of a vacuum-free high-intensity X-ray source in helium at atmospheric pressure. The vacuum-free X-ray source may be a promising tool for the laboratory-based X-ray diffraction experiments.

3.1 Introduction

A variety of femtosecond X-ray sources has been developed, such as laser-produced plasma X-ray, ultrafast hard X-ray produced by synchrotron and X-ray free electron laser (XFEL). The intensity or coherency of X-ray in synchrotrons or XFEL is quite high; however, the instruments are very expensive and require huge and complex facilities. Moreover, the availability of such huge facilities is limited. [55, 56, 57] In comparison, laser-produced plasma X-ray sources need to be small, lab-scale facilities. Laser-produced plasma X-ray sources consist of high-power (above 100 mJ) and low-repetition rate (about 10 Hz) lasers and the Kα X-ray intensity using this large size laser was reported to be 10^8–10^{11} cps/sr with conversion efficiency of 10^{-4}–10^{-5}. [58, 59, 60, 61] Generally an X-ray intensity of more than several 10^8 cps/sr is required for time-resolved X-ray diffraction experiments, and a laser-plasma X-ray of 10^9–10^{11} cps/sr is desirable. [62] This intensity is sufficiently high for X-ray radiographic applications; however, the utilization of such ultrafast pulsed X-ray has been limited because of the complexity of the huge vacuum system

and difficulty in managing a high-power laser. To date, a huge laboratory-top laser and a large size vacuum chamber are prerequisites for generation of ultrafast pulsed X-ray radiation. In this laboratory-scale ultrafast X-ray source, there are also some problems with target shapes and debris from the target caused by laser ablation. Regarding the target shape, thin tape or wire type targets have been used because the space in the vacuum chamber is limited. The small tape or wire target can be put in a vacuum chamber; however target lifetime is quite short at about several hours or at most a few days. It is difficult to control the surface of the thin tape or wire within a few micrometers. There is also the problem of debris from the target. When the high-power laser is focused onto the target, target material is blown off and deposited on the focusing lens, windows, and other optics. Thin polymer tape covers have been employed to avoid the debris problem. Thus, such ultrafast pulsed X-ray sources were required to be more compact, easier to access, and have higher conversion efficiency into characteristic X-ray.

Recently, the compact-designed tabletop submillijoule-to-several-millijoule femtosecond laser has been reported to be available for generating hard X-ray with an intensity of about 10^8–10^{10} cps/sr with Kα X-ray conversion efficiency of 10^{-5}–10^{-6}.[63, 64, 65] Although the experimental scale of a femtosecond laser could be successfully reduced with a tabletop femtosecond laser, difficulties with using a huge and complex vacuum chamber system; such as target manipulation, target lifetime, and debris emissions remain. Therefore, a high-intensity X-ray source that can operate in atmospheric pressure (1.05×10^5 Pa) with a tabletop laser could be a more desirable tool for ultrafast time-resolved measurements. Laser-induced plasma X-ray sources operating in helium atmospheric conditions have been reported, however the X-ray intensity from these sources was quite low.[66] Very recently, J. A. Nees et. al. have developed a high intensity X-ray source ($\sim 5 \times 10^9$ cps) operating in helium atmospheric conditions at high plasma intensity of above 1.0×10^{18} W/cm^2. Nevertheless, the high laser intensity above 1.0×10^{18} W/cm^2 could extend the X-ray pulse duration up to picosecond order.[67, 68] At the laser intensity of 1.0×10^{16} W/cm^2 and 1.0×10^{18} W/cm^2, the extension of pulse duration was ~100 fs and ~1 ps respectively. Therefore, laser-induced plasma source with lower (at most 5.0×10^{16} W/cm^2) laser intensity is required for femtosecond time-resolved X-ray diffraction applications.

In this study, we demonstrated a compact and high-intensity ultrafast pulsed X-ray source constructed to operate in a helium atmosphere with low laser intensity (about 5.0×10^{16} W/cm^2). It is possible to reduce the overall size of the X-ray source system without the complexity of a vacuum system

	synchrotron X-ray	laser-induced plasma X-ray		
		High Power (>100mJ)	Low Power (~1mJ)	
size of the facility	facility-top	laboratory-top	table-top	
Laser forcsing condition		in vacuum condition		in atomspheric condition
X-ray intensity	$10^{15} \sim 10^{17}$ cps/mm^2·(mrad)^2·0.1%	$10^{8} \sim 10^{11}$ cps/sr	$10^{8} \sim 10^{10}$ cps/sr	$10^{8} \sim 10^{9}$ cps/sr
X-ray conversion efficiency (Kα X-ray)		$10^{-4} \sim 10^{-5}$	$10^{-5} \sim 10^{-6}$	$\sim 10^{-6}$
Available pulse duration (estimation)	100 fs - 100 ps	200 fs - 2 ps	100 fs - 2 ps	100 fs - 2 ps
cost	extremely high	high	low	low
user-convenience	huge facility limitation of utilities	huge laser system complexity in utility of vacuum	compact laser system complexity in utility of vacuum	compact laser system no vacuum system

Figure 3.1: General comparison of the laser-induced plasma X-ray with low-power femtosecond laser with X-ray from synchrotron and high-power femtosecond laser.

and it is also feasible to set a long-lived and large-sized target regardless of the vacuum chamber in air. The samples measured with time-resolved X-ray diffraction are placed close to the X-ray generating spot without a vacuum system, enabling more and more efficient use of the generated X-ray. This vacuum-free X-ray system allows us to avoid the debris problem. At atmospheric pressure, the debris cannot reach the focusing lens or other optics, which are placed some ten millimeters away from the focusing spot. With helium or other gas jet, the debris can be easily collected with a filter. Moreover, the pulse duration of the X-ray can be suppressed at about a few hundred femtosecond with low laser intensity. In Fig. 3.1, we summarized a general comparison of various X-ray sources from synchrotron and laser-induced plasma X-ray with high power to low power femtosecond laser.

3.2 General description for the ultrafast X-ray radiation

When a high-intensity laser pulse is focused onto a metal target, ionization of the target material turns the surface into near-solid-density plasma. The

absorption of the laser pulse into the surface material varies with the intensity of the laser-produced plasma. The plasma intensity generated on the laser focusing spot, is the key parameter for the pulse duration of the laser-induced plasma X-ray. The plasma intensity is calculated from the laser power of a single pulse, its pulse duration and the diameter of focusing spot. Plasma intensity is expressed as $I\lambda^2$, where I and λ are the laser intensity and wavelength, respectively. In the range of lower plasma intensity, $I\lambda^2 < 1 \times 10^{15}$ Wμ m^2/cm^2, almost all of the absorbed laser energy transfers through collisional processes, such as inverse-bremsstrahlung. [69, 70, 71] In the plasma intensity range of 1×10^{15}–4×10^{16} Wμm^2/cm^2, laser-produced plasmas are reportedly absorbed into the target via a more complicated collisionless process, such as resonant absorption. [71, 72, 73, 74, 75] In the higher plasma intensity range, $I\lambda^2 > 4\times10^{16}$ Wμm^2/cm^2, the dominant absorption processes of laser-produced plasma are turned into vacuum heating. [76] Some other processes are important above plasma intensities of $I\lambda^2 > 1 \times 10^{17}$ Wμm^2/cm^2, such as Raman heating or the two-dimensional effect. [77, 78] Hot electrons are created in the near surface region of the target with energy of 1–5 keV. [79] The hot electrons in the laser plasma interact with the incident laser pulse and are accelerated into the solid target. As the high-energy electrons penetrate into the target material, X-rays are generated via ionization of the target material, or bremsstrahlung. The pulse duration of these laser-produced X-rays is similar to the incident laser pulse, i.e., several hundred fs, because they occur when the hot electron is on the target surface. [80]

3.2.1 Intensity estimation of the ultrafast X-ray

Kα X-ray generated from the metal target was used for the time-resolved X-ray diffraction measurements. Kα X-ray is emitted when the electron transits from the L-shell to K-shell, and is classified as Kα1 X-ray and Kα2 X-ray which correspond to the electron transition from the $P_{3/2}$ state in the L-shell to the $S_{1/2}$ state in the K-shell and one from the $P_{1/2}$ state in the L-shell to the $S_{1/2}$ state in the K-shell, respectively. In this section, the X-ray intensity from laser plasma was briefly estimated with the electron entry time into the solid and the photon generating time.

Analytically, the Kα X-ray yield from a hot electron distribution can be expressed as an energy integral over the properties of monoenergetic electrons: [81]

$$N = \int n_{\mathrm{hot}} f_{\mathrm{hot}}(E) N_{\mathrm{gen}}(E) f_{\mathrm{em}}(E) dE \tag{3.1}$$

where N is the number of emitted photons, n_{hot} is the total number of hot

electrons, and $f_{\rm hot}(E)$ is their energy distribution; $N_{\rm gen}(E)$ is the number of Kα photons generated by an electron with incidence energy E, and $f_{\rm em}(E)$ is the fraction of these photons that escapes from the solid. The number of Kα photons generated by an electron of incidence energy ($N_{\rm gen}(E)$) was obtained by M. Green *et.al.* as:[82)]

$$N_{\rm gen}(E) = 4 \times 10^{-3} Z^{-1.67} E^{\frac{3}{2}}, \tag{3.2}$$

where Z is the atomic number and the energy is expressed in keV. The incident electron energy is normalized to the K-shell ionization energy of the target because the emission factor shows a universal behavior with the normalized energy U.

$$U = \frac{E}{E_k}. \tag{3.3}$$

At $U = 20$, the mean depth of Kα generation in the target is comparable to the absorption length for self-emitted Kα radiation, so that for $U < 20$ most of the generated photons can escape from the target. For $U > 20$, both electron penetration depth and reabsorption both increase, so that $f_{\rm em}(E)$ decreases. To facilitate the integration of Eq. (3.1), the emission factor was approximated by the step function:

$$f_{\rm em} = \begin{cases} 1 & (U \leq 20) \\ 0 & (U > 20) \end{cases} \tag{3.4}$$

The total number of hot electrons ($n_{\rm hot}$) and the energy distribution ($f_{\rm hot}(E)$) was simulated by Reich *et.al.* as a function of laser intensity. The energy distribution ($f_{\rm hot}(E)$) was best fitted with the one-dimensional Maxwellian energy distribution,

$$f(E)dE = \frac{1}{\sqrt{EkT}} \exp(\frac{-E}{kT})dE \tag{3.5}$$

$$kT \approx 130({\rm keV}) \sqrt{\frac{I}{10^{17}({\rm W/cm^2})}}, \tag{3.6}$$

while the number of generated electrons was:

$$n_{\rm hot} \approx 1.9 \times 10^{20} I^{\frac{1}{2}}. \tag{3.7}$$

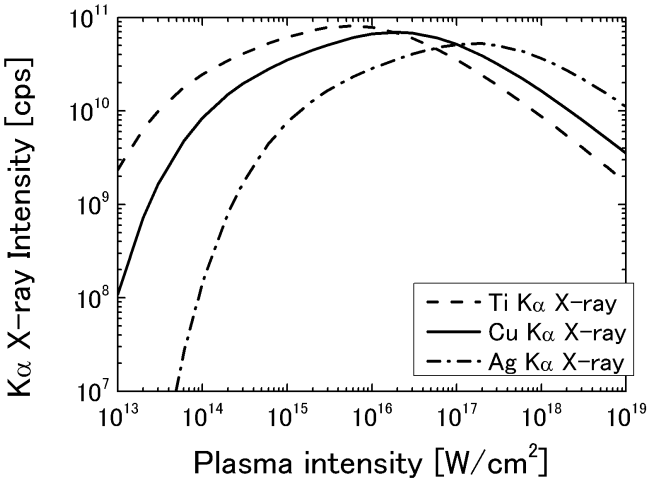

Figure 3.2: Simulated Kα X-ray yield from bulk titanium, copper, and silver targets for a laser with energy of 1 mJ and laser repetition rate of 1 kHz.

Integrating $\int n_{\rm hot} f_{\rm em} EdE$ and applying Eq. (3.6) for the hot electron temperature gives the total energy of the hot electrons. This product is independent of the laser intensity. Gathering these results together, the total Kα X-ray yield of Eq. (3.1) in the interval $1 \leq U \leq 20$ is:

$$N = 3.5 \times 10^{16} \frac{Z^{2.73}}{I^{\frac{3}{4}}} \int_1^{20} U \exp\left(-\frac{U}{U_{kT}}\right) dU, \tag{3.8}$$

with the shape of the integrand being determined by the normalized electron temperature

$$U_{kT} = \frac{kT}{E_{kT}} = 7.6 \times 10^{-5} \frac{\sqrt{I}}{Z^{2.2}}. \tag{3.9}$$

U_{kT} is also the electron energy at which most of the Kα photons are produced. In Fig. 3.2, the number of Kα X-ray emission from copper target with 1 mJ and 1 kHz femtosecond laser is shown as a function of laser intensity.

3.2.2 Pulse width estimation of ultrafast X-ray

The duration of the Kα X-ray pulse is the most critical parameter for the applications involving time-resolved X-ray diffraction or spectroscopy. [81)] Experimental methods for the pulse duration measurement are the ultrafast streak camera measurement and the pump-probe measurement of ultrafast dynamics. The pulse duration of ultrafast X-ray is directly measured with the streak camera. In the streak camera light is changed into electrons and the electrons are accelerated and detected with the detector. In this process, the generated electrons have wide-range energy and it makes the pulse duration resolution of streak camera last more than a few picoseconds. Thus until now, in order to measure the pulse duration of ultrafast X-ray precisely, one had to observe the ultrafast change of X-ray diffraction patterns. In this section, a simulation for the estimation of X-ray pulse duration produced by laser plasma is introduced. The pulse duration of laser-produced plasma X-ray was extended with increase in the laser plasma intensity.

Kα X-ray is generated shortly after the first hot electrons are generated and enter the solid. After the laser pulse has gone, it continues until the energy of the last hot electron in the solid has dropped below the K-shell ionization energy. The total duration of the X-ray emission (τ_z) is thus the sum of the durations of the laser pulse (τ_l) and of the"afterglow "emission (τ_a).

$$\tau_x \approx \tau_l + \tau_a. \tag{3.10}$$

Above the plasma intensity of 1.0×10^{16} W/cm^2, a small fraction of superhot electrons can produce a long-lasting Kα afterglow with low intensity.

The pulse duration of Kα X-ray is strongly depend on the time duration the hot electron spends in the target material. With increasing incidence energy, this excursion time initially increases, since faster electrons need more scattering events to lose their energy; therefore, the Kα pulse duration increases with the higher laser intensity. Thus, the pulse duration of the Kα X-ray at laser intensity of about 10^{16} W/cm^2 was simulated by Reich *et.al.* with the Monte Carlo code as:

$$\tau_a \sim 100 Z^{-0.4} l^{0.8}, \tag{3.11}$$

where the units are fs, mm, and keV. The $1/e$ penetrating depth in copper material for 8.05 keV photons is about 5.6 μm, and for example, the pulse duration of the Kα X-ray at plasma intensity of 4.0×10^{16} Wμm^2/cm^2 was estimated to be about 200 fs.

3.3 In-air X-ray source

3.3.1 System for the in-air X-ray source

Figure 3.3 and Fig. 3.4 show the schematic experimental setup and photograph for ultrafast pulsed X-ray generation. The mode-rocked Ti: sapphire laser generated femtosecond optical pulses of about 100 fs duration with wavelength at 800 nm, and the optical pulses were amplified at about 3.5 mJ/pulse through the regenerative amplifier (Spectra Physics) described in chapter 3. The laser pulse profile was TEM_{00}. The optical pulse had a

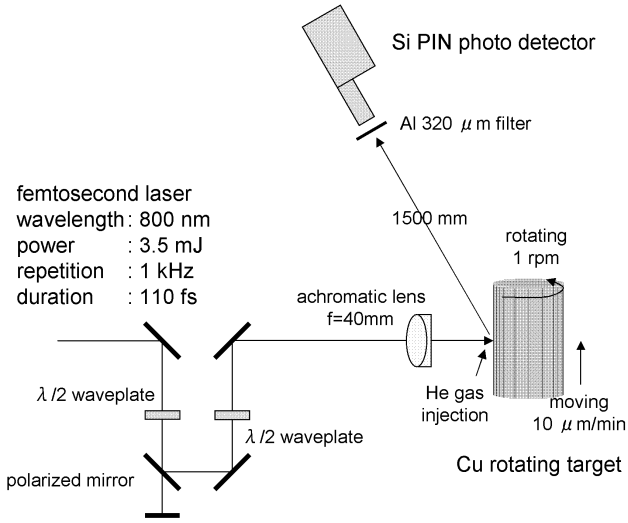

Figure 3.3: The experimental setup for ultrafast pulsed X-ray generation at ambient pressure.

prepulse, which was generated in the regenerative amplifier of the laser system itself as leakage through the Pockels cell before the final pulse of the pulse train was switched off. The prepulse contrast to the main pulse was measured to be 8×10^4, and the time separation between the prepulse and main pulse was 20 ns. The effect of a 10 ns prepulse plasma on X-ray generation can be negligible even if the prepulse generates preplasma on the target surface. The p-polarized optical pulse was focused into a rotating copper target with an infrared achromatic lens (f = 40 mm). The focusing spot size was 4.8 μm, which was measured by the crater size of the focusing spot.

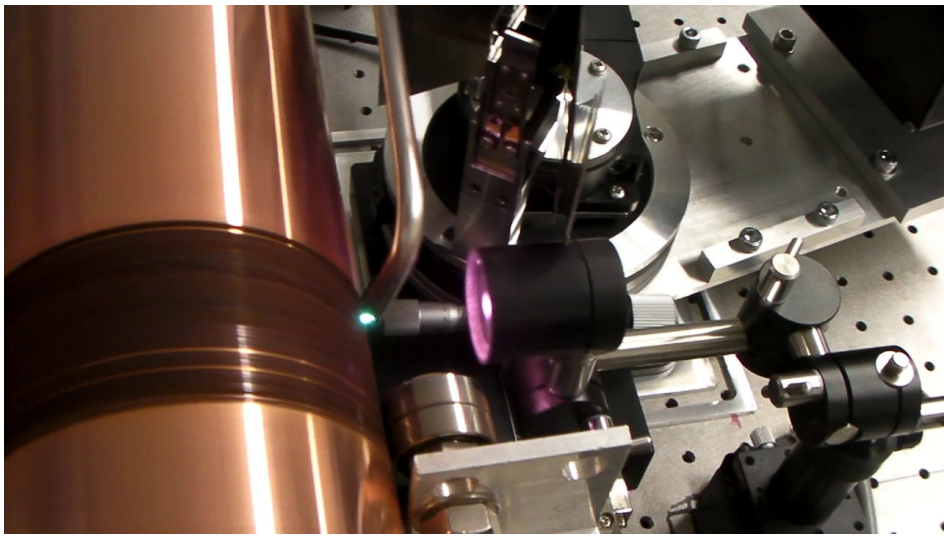

Figure 3.4: The photograph of ultrafast pulsed X-ray generation at ambient pressure.

The pulse duration of the laser pulse on the surface of copper target was 110 fs. The power of the optical main pulse was 0.06–1.46 mJ. The copper target was a circular cylinder of 100 mm diameter and 300 mm length. The surface position of the rotating copper target was controlled within ± 1 μm with precision bearings and adequate tension of springs, and was measured with a micrometer during rotation. The copper target rotated at a rate of 1 (> 0.96) rpm, which could be varied in the range 0.24–1 rpm and moved in the axial direction at the rate of 10 (> 4.8) μm/min, which gave a fresh copper surface with each laser shot. An X-ray generating operation of more than 20 days can be available with this long-life copper target. The atmosphere in the copper target system near the focus point could be changed between air and helium. The helium gas was introduced with 1/4 inches gas nozzle and the flow rate of helium gas was 500 ml/min.

The X-ray generated from focusing the laser pulse onto a copper target was measured with a p-intrinsic-n (PIN) Si photo detector (Amptek, XR-100CR), equipped with a 300 μm-thick, 7 mm^2 square silicon detector with detection efficiency of approximately 100% for 8 keV X-rays. The detector was sealed with a 25 μm-thick Be window in which an 8 keV X-ray penetrates without any loss. The signal from the detector was amplified with a spectroscopy amplifier (CANBERRA, 2022 Spectroscopy Amplifier) and

was processed with a multichannel analyzer (SEIKO EG&G, TRUMPMCA-2k). The detector was placed 1500 mm away from the focusing spot at an angle of 60°. The attenuation value in ∼1500 mm atmospheric air is 85% for Cu Kα X-ray. In He ambient, a 320 μm thin aluminum filter was placed before the detector, and this reduces the intensity of Cu Kα X-rays by 1.72%. The long distance between the X-ray focusing spot, the detector and the Al filter allowed us to measure the X-ray photons as a Poisson distribution for single photon counting. A Si photo detector and a multichannel analyzer cannot detect two photons at once in a period on the order of 1 ms. If more than one photon is present at the same time, the total detected energy in the Si photo detector is doubled. For all conditions, it took 40 s to obtain each X-ray spectrum.

3.3.2 High intensity X-ray radiation

A typical X-ray spectrum obtained with the Si-PIN photo detector is shown in Fig. 3.5. The dashed line with square symbols is the X-ray spectrum measured with the Si-PIN photo detector. The X-ray generated on the focusing spot went through 1500 mm of air and an Al filter of 320 μm (in He atmosphere), thus the X-ray intensity was reduced depending on the energy to obtain the single photon counting. The solid line with circle symbols is the calculated X-ray spectrum. X-ray radiation from p-polarized laser is regarded as isotropic radiation. [83] As shown by the solid line in Fig. 3.5, a strong Cu Kα X-ray line (8.05 keV), Kβ X-ray line (8.91 keV) and a small part of the bremsstrahlung X-ray were found in the energy range of several keV.

The Kα intensity as a function of plasma intensity in various atmospheric conditions is shown in Fig. 3.6 for the range 1.5×10^{15}–4.0×10^{16} Wμm^2/cm^2. The plasma intensity was varied to change the incident laser pulse energy in the range 0.06–1.46 mJ/pulse by rotating the first $\lambda/2$ waveplate of the main pulse line in Fig. 3.3. At this plasma energy, the laser absorption process into the target is collisionless. The polarized mirror in the main pulse line lets p-polarized light pass through and s-polarized light be reflected. In this condition, the prepulse line was blocked and the effect of the preplasma was negligible. We obtained high intensity Cu Kα X-rays with 2.6–5.4 $\times$ 10^9 photons/sr/s above the plasma intensity of 2.0×10^{16} Wμm^2/cm^2 in He atmosphere. This intensity was more than 60 times that in air. Generally, a value of at least several 10^8 cps/sr characteristic X-ray is required for time-resolved X-ray diffraction or other applications. In Fig. 3.6, the horizontal dashed line shows the X-ray intensity of 1.0×10^9

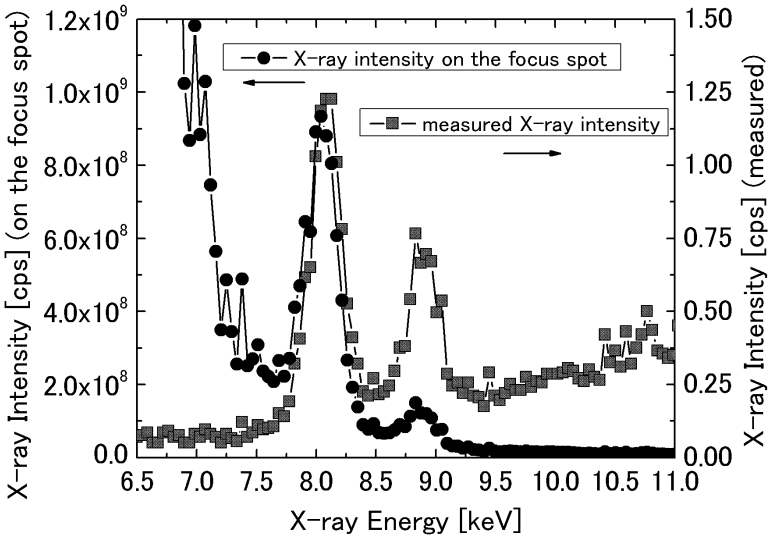

Figure 3.5: Typical X-ray spectrum.

cps/sr. The intensity of X-ray radiation in helium atmosphere is sufficient for time-resolved X-ray measurements.

3.4 Effect of ambient pressure on ultrafast X-ray generation

In this section, we demonstrate the use of Kα X-ray radiation in air, helium or vacuum (2.7–1.3 $\times$ 10^4 Pa) ambient in the study of the relationship between Kα X-ray intensity (or conversion efficiency) and atmospheric conditions. The relationship was explained with a simple electron collision model, in which the hot electrons generated by the laser pulse interact with the target atoms unless they interact with the ambient atoms. The model suggested that the electron mean free path is an important parameter in the generation of ultrafast pulsed X-rays in any ambient condition, and the helium is the most suitable gas for the ambient condition.

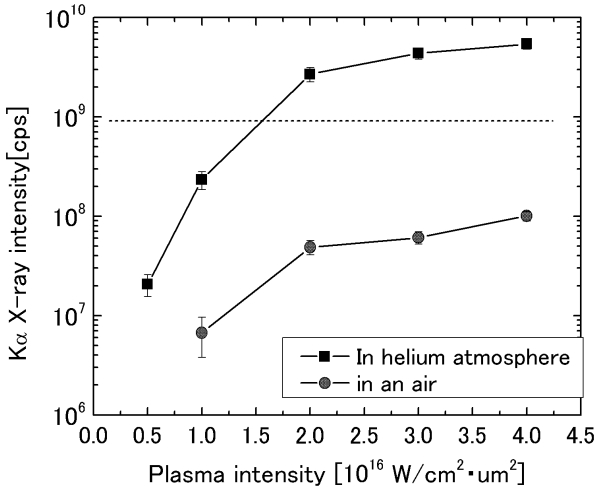

Figure 3.6: Kα X-ray intensity in ambient pressure of helium and air, as indicated.

3.4.1 Systems for ultrafast X-ray radiation in various atmospheres

A schematic drawing of the experimental setup for ultrafast pulsed X-ray generation in various ambient atmospheres, i.e., air, helium or vacuum (pressure range 2.7–1.3 $\times$ 10^4 Pa) is presented in Fig. 3.7. Optical pulses by the regenerative amplifier were focused into a moving copper target with infrared achromatic lens (f = 40 mm) with a spot size of 4.8 μm. The energy of the optical pulse was varied in the range 0.18–1.46 mJ. The moving copper target was placed in a vacuum chamber equipped with two leak valves used for varying the vacuum level. The surface position of the copper target was controlled within $\pm$1 μm, which could be measured with a micrometer during motion. The ambient near the focus point in the Cu target system could be varied between air, helium or vacuum. For samples immersed in helium ambient, the gas was introduced through a 1/4-inch gas nozzle and was blown onto the Cu target surface at a flowrate of 500 ml/min. For vacuum conditions, the chamber was evacuated with a dry pump with the leak valves closed (2.7 Pa) and with the leak valves opened (1.3 $\times$ 10^3 Pa or 1.3 $\times$ 10^4 Pa). The signal from the detector was amplified with the

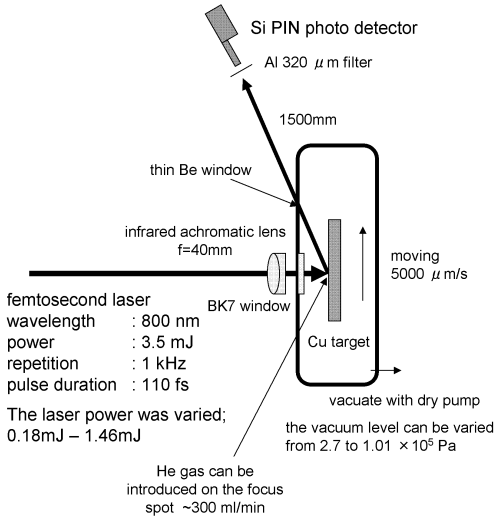

Figure 3.7: Schematic drawing of the experimental setup for ultrafast pulsed X-ray generation in various ambient conditions.

spectroscopy amplifier and was processed with the multichannel analyzer. The detector was placed 1500 mm away from the focusing spot at an angle of 60∘. Under vacuum conditions, the X-ray traveled 3 mm in a vacuum and 1497 mm in air. In He ambient or under vacuum conditions, a 320 μm thin aluminum filter was placed before the detector.

3.4.2 Ultrafast X-ray radiation in ambient pressure

Figure 3.8 shows the typical X-ray spectra generated at the focusing spot in vacuum and in air. The X-ray radiation from a p-polarized laser is regarded as an isotropic radiation hemisphere and therefore, the X-ray spectra were computed into 2π. In the spectra presented in Fig. 3.8, a strong Cu Kα X-ray line (8.05 keV), a Kα X-ray line (8.91 keV) and a small part of bremsstrahlung X-ray were observed in the energy range of several keV. A rapid decline in Kα X-ray intensity occurred as the pressure increased above 1.3×10^4 Pa. Figure 3.9 shows the spectra of high-energy bremsstrahlung emission in the range of 10–14 keV in helium at atmospheric conditions at a plasma intensity of 4.0×10^{16} Wμm^2/cm^2. The hot electron temperature can be derived from Fig. 3.9. The Kα X-ray emission is produced

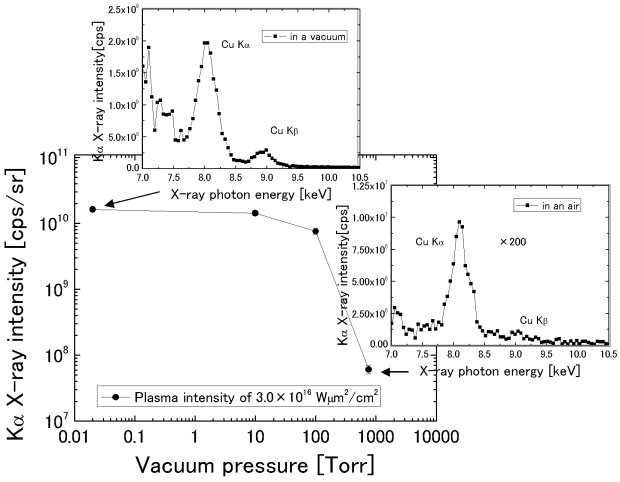

Figure 3.8: Cu K α X-ray intensity at a plasma power of 3.0×10^{16} Wμm^2/cm^2 as a function of pressure. Two X-ray spectra are shown, in vacuum and in air.

by a distribution function of hot electrons characterized by a temperature of about 3.4 keV, which corresponds well to the previously reported hot electron temperatures of 1–5 keV. [79)]

The Kα X-ray conversion efficiency ($\eta_{\mathrm{K}\alpha}$) is defined as:

$$\eta_{\mathrm{K}\alpha} = nh\nu_{\mathrm{K}\alpha}/E_{\mathrm{pulse}}, \tag{3.12}$$

where n is the number of Kα X-ray photons generated per pulse, $h\nu_{\mathrm{K}\alpha}$ is Kα X-ray energy, and E_{pulse} is the single pulse energy of incident laser. At these plasma energies, the laser-produced plasma is absorbed into the target via a collisionless process such as resonant absorption. For all ambient conditions vacuum (2.7–1.3 $\times$ 10^4 Pa), He and air at atmospheric pressure, the conversion efficiency increased as a power function in the plasma intensity range of 1.0–2.0 $\times$ 10^{16} Wμm^2/cm^2, because more hot electrons were generated and their energy increased with plasma intensity; a plateau was reached at 2.0 $\times$ 10^{16} Wμm^2/cm^2. These tendencies are similar to the experimental data obtained by other groups with high-repetition laser in a vacuum. [63, 64, 65)] The conversion efficiency in helium at atmospheric pressure was 5.0×10^{-6}, which was 30% of that at 2.7 Pa; in a vacuum of 1.3×10^4 Pa, the conversion efficiency was 50%–60% of that at 2.7 Pa. Overall, in vacuum conditions

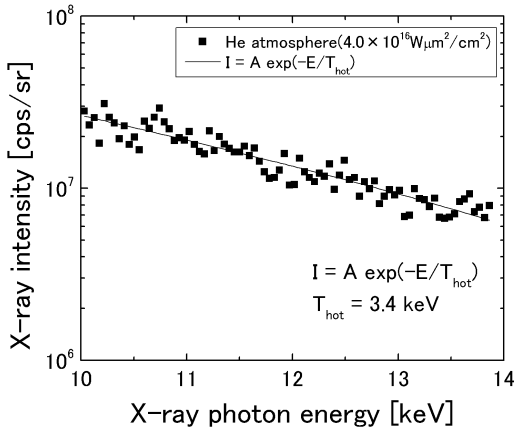

Figure 3.9: Spectra of high-energy bremsstrahlung emission in the range 10–14 keV (in helium at atmospheric conditions; plasma intensity: 4.0×10^{16} Wμm^2/cm^2). The X-ray intensity was fitted by a Maxwellian electron distribution; the hot electron temperature (T_{hot}) was found to be about 3.4 keV

(2.7–1.3 $\times$ 10^4 Pa) and in a helium atmosphere, the conversion efficiency of the Kα X-ray was two orders of magnitude higher than in air.

3.4.3 Electron collision model

The laser power loss in air or helium plasmas was quite low, below 10% and 1%, respectively. Moreover, the incident pulse duration of the laser was not extended in air or helium plasmas. The changes in pulse profile, in helium atmosphere, i.e., wavelength and pulse duration, were reported to be quite small for plasma intensities on the order of 1.0×10^{16} Wμm^2/cm^2. [84, 85, 86] This suggests that for air or helium at atomspheric pressure the effect of reduction in plasma intensity or a breakdown in the ambient gases on the X-ray conversion efficiency in air or helium at atmospheric pressure was negligible. Some authors have indicated that the decrease in X-ray conversion efficiency in ambient atmosphere was caused by the defocusing effect of the laser pulse in helium or in air. [87, 88, 89] Defocusing of the laser pulse on the focusing spot has occurred, but it is difficult to explain quantitatively the X-ray intensity reduction in ambient atmosphere only with the defocusing effect. The interactions between the generated electrons and the ambient

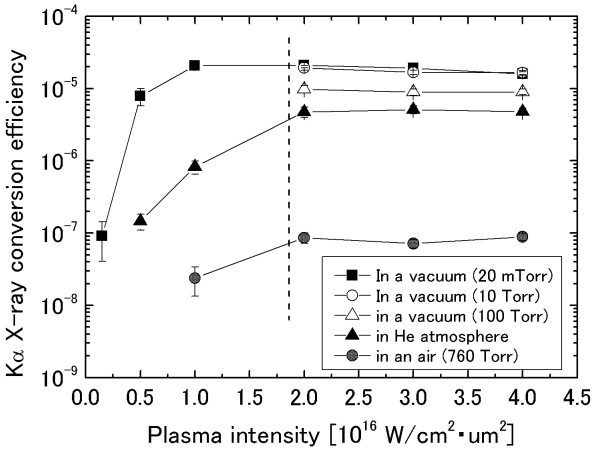

Figure 3.10: Kα X-ray conversion efficiency, plotted as a function of plasma intensity under various conditions. Symbols are indicated in the inset legend. The dashed line shows the boundary of the intensity increasing region and the plateau

atoms/molecules should be also considered in describing a proper model for the generation of laser-plasma-induced X-ray.

The Kα X-ray conversion efficiency in air or a vacuum of 1.3×10^3 Pa or 1.3×10^4 Pa was normalized with that in a vacuum of 2.7 Pa for the plasma intensities of 2.0–4.0 $\times$ 10^{16} Wμm^2/cm^2 and was plotted as a function of pressure and electron mean free path (Fig. 3.10). Regarding the electron generation and acceleration process, the target surface on the focusing spot changes into nearsolid- density plasma by the incident laser pulse. The expansion region of the electrons in plasma is on the order of the incident pulse wavelength from the surface, within the time scale of several fs. After traveling through the expansion region, the electrons are accelerated by the incident laser pulse into the target. When there are atoms/molecules of ambient gas near the focusing spot, the electron can interact with these atoms/molecules before and while being accelerated. The electron traveling distance without interaction with the ambient gases is the electron mean free path in this atmosphere. The interaction cross-section between the electron and atoms/molecules is given by the simple electron collision model. The electron mean free path is expressed as the equation

$$\lambda = kT/(\pi r^2 p), \tag{3.13}$$

where λ is the electron mean free path in the ambient, k is the Boltzmann constant, r is the radius of the molecule and T and p are temperature (20°C) and pressure of the ambien gas. In air the pressure is 1.01×10^5 Pa and λ is 0.34 μm. At 1.3×10^4 Pa, 1.3×10^3 Pa and 2.7 Pa, the values of λ were 2.6 μm, 26 μm and 13 mm, respectively (Fig. 3.11, lower horizontal axis). In the simple electron collision model, electrons collide with the atoms/molecules in the ambient gas before or during their acceleration by the incident pulse. The electrons that collided with the ambient gas cannot reach the surface of the target material and therefore do not participate in the generation of Kα X-ray of the target materials. The energy of hot electrons in the plasma is in the range of 1–5 keV, and ions of the target materials in the plasma also have almost the same energy. In the first several fs, the ions in the plasma do not have enough velocity and remain near the target surface. The number of electrons accelerated by the incident pulse decreases exponentially as the electrons move into the ambient atmosphere as a result of the interaction between electrons and atoms/molecules in the ambient atmosphere. The number of X-ray photons is proportional to the number of accelerated electrons that arrived near the target material surface. Thus, the X-ray intensity can be expressed by the equation

$$I = I_0 \exp(-A/\lambda), \tag{3.14}$$

where I_0 is the intensity of the generated X-ray on the target, I is the intensity of the measured X-ray in the ambient and A and λ are average traveling length and electron mean free path in the atmosphere as described in Fig. 3.12. In Fig. 3.11, the solid line represents the modified form of Eq. 3.14, i.e.,

$$I/I_0 = \exp(-A/\lambda), \tag{3.15}$$

with $A = 1.47$ μm.

The normalized X-ray conversion efficiency was well fitted with the equation of the simple electron collision model. At plasma energies of 2.0×10^{16}, 3.0×10^{16} and 4.0×10^{16} Wμm^2/cm^2, the values of A were fitted as 1.76 $\pm$ 0.13, 1.67 $\pm$ 0.21 and 1.31 $\pm$ 0.13 μm, respectively. This means that the electrons in the plasma traveled 1–2 μm in the atmosphere before incidence with the target surface or with the near-solid-density plasma of the target materials. Figure 3.11 also shows the relationship between the normalized X-ray conversion efficiency and the electron mean free path reported by Serbanescu et. al. at a plasma intensity of 6.9×10^{16} W/cm^2, which also fit well with the equations of the simple electrons collision model. [90] The value

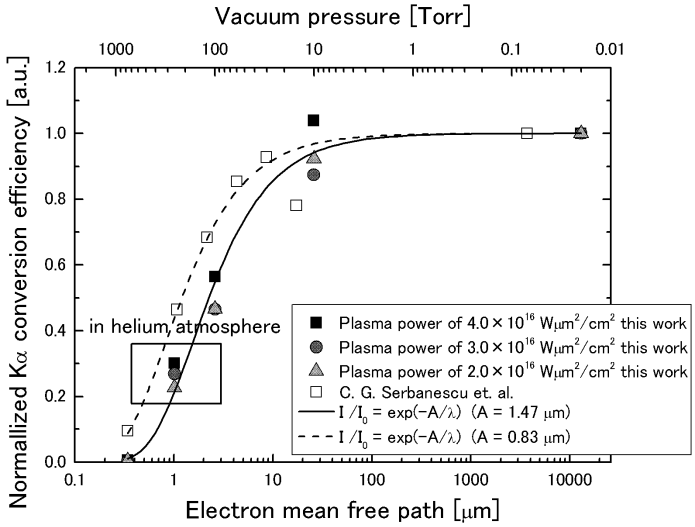

Figure 3.11: Comparison between the normalized Kα X-ray conversion efficiency in this work and in Serbanescu et. al.. Symbols are indicated in the inset legend.

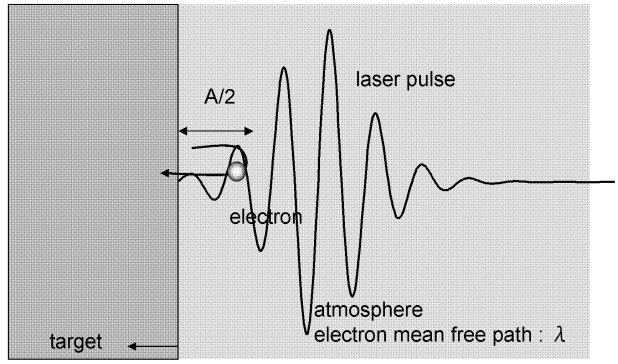

Figure 3.12: Schematic drawing of the electron collision model.

of A in atmosphere was 0.83 ± 0.11 μm (Fig. 3.11, dotted line). Regarding the helium ambient, λ was calculated to be 1.01 μm at 1.01×10^5 Pa in air. The normalized X-ray conversion efficiency in helium ambient could also be fitted successfully with the equations of the simple electron collision model (Fig. 3.11), meaning that Eq. (3.15) described the X-ray conversion efficiency regardless of the specific atoms/molecules in the atmosphere. The electron mean free path at atmospheric pressure is also suggested as an important parameter in generating ultrafast pulsed X-ray in any ambient at atmospheric pressure.

The electron traveling length in a specific atmosphere should vary with the focusing conditions and the plasma intensity on the focusing spot. Generally, the gradient of the electrical field increases with plasma intensity, and the focusing spot size and the Rayleigh length of the incident pulse on the spot vary with focusing optics. Above a plasma intensity of 2.0×10^{16} Wμm^2/cm^2, the average electron traveling length in the atmosphere was 1–2 μm and the electron mean free path of helium at atmospheric pressure was 1.01 μm. The X-ray intensity in helium ambient at atmospheric pressure was calculated to be 20%–40% of its value in vacuum conditions. We also obtained an X-ray conversion efficiency of 5.0×10^6, which was 30% of that at 2.7 Pa, suggesting that a high-intensity ultrafast pulsed Kα X-ray source in helium operating at 1.01×10^5 Pa can be realized without vacuum. [91, 92)]

3.5 Effect of prepulse for ultrafast X-ray radiation

The generated X-ray intensity is enhanced with prepulse, which produces very weak plasma on the target surface prior to the main pulse. [65, 93, 94, 95, 96)] The mechanism of X-ray intensity enhancement with prepulse is explained by the strong interaction between electrons in the preplasma and the main laser pulse. The prepulse produces weak plasma on the surface of the target and electrons in the plasma gradually expand from the surface within a distance of more than a few micrometers in the time scale of 10–100 ps. Then, the main pulse enters the plasma and the dispersed electrons are accelerated into the target surface. It has been reported that the X-ray intensity with prepulse enhancement is three to ten times higher than with only a main pulse, and the time separation between prepulse and main pulse is on the order of 10–100 ps. [65, 96)] Regarding prepulse, there is an advantage and a disadvantage; the advantage is improved the X-ray yield and the disadvantage is the extended the X-ray pulse duration. The electrons in plasma can expand from the surface to a distance of more than 30 μm even in a low

vacuum pressure of 10 torr. A traveling distance of more than 30 μm from the surface at the speed of light indicates that the pulse duration extension was more than 100 fs.

3.5.1 System for the X-ray radiation with prepulse

Figure 3.13 shows the experimental setup for ultrafast pulsed X-ray generation with various prepulse time separations. The optical pulse generated through the regenerative amplifier was separated by the 1:9 beam splitter. The stronger pulse was changed its polarization by the first $\lambda/2$ waveplate and was reflected in the part of the s-polarized pulse by the polarized mirror. The intensity of the main pulse can be varied with this polarized mirror. The main pulse changed its polarization to p by the second $\lambda/2$ waveplate and penetrated a polarized beam splitter that reflected the s-polarized beam 30% and let the p-polarized beam go through. The weaker pulse for inducing preplasma changed its polarization into s, went through an optical delay line, and was reflected by the polarized beam splitter. The main pulse and prepulse were brought in the same line and focused into a rotating copper target with an infrared achromatic lens (f = 40 mm). The focusing spot size was 4.8 μm. The pulse duration of the laser pulse on the surface of copper target was 110 fs. The power of the optical main pulse was 0.37–1.46 mJ and the power of prepluse was fixed, 0.06 mJ. The intensity of the X-ray radiation was measured with the same detection system as previously described.

3.5.2 Effect of prepulse in helium ambient

X-ray intensity can be enhanced with prepulse plasma because of the strong coupling between the laser pulse and preplasma generated with prepulse. The enhancement of prepulse plasma is shown in Fig. 3.14 at a preplasma power of 1.6×10^{15} Wμm^2/cm^2. The power of preplasma was 4%–8% of the main plasma power between 2.0×10^{16} Wμm^2/cm^2 and 4.0×10^{16} Wμm^2/cm^2, and the separation time between the prepulse and the main pulse was 5 ps. The Kα X-ray intensity was plotted as a function of the plasma intensity in helium (Fig. 3.14 (a)) and in air (Fig. 3.14 (b)). Above the plasma intensity of 2.0×10^{16} Wμm^2/cm^2, the obtained X-ray intensities with prepulse were 1.3 times higher in helium and two times higher in air. The Kα X-ray intensity obtained in helium with prepulse was 7.7 $\times 10^9$ cps/sr, which was 40% of the yield in a vacuum without prepulse. In a vacuum, the Kα X-ray intensity with prepulse enhancement has been

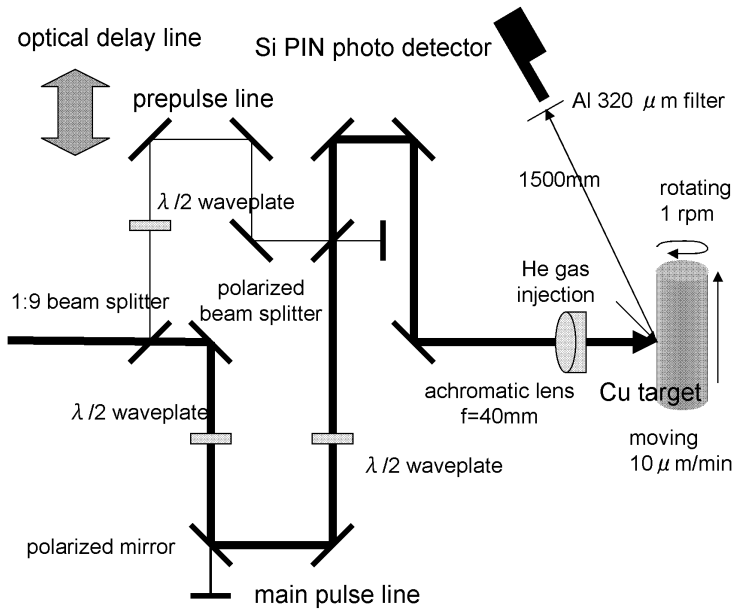

Figure 3.13: Experimental setup for the X-ray radiaton with various prepulse time separations.

reported to be three to ten times higher than with the main pulse only. The prepulse enhancement effect of Kα X-ray intensity in a helium atmosphere was smaller than that in a vacuum.

Figure 3.15 shows the variation in X-ray intensity with prepulse separation time from main pulse at plasma intensity of 3.0×10^{16} Wμm^2/cm^2 in helium at atmospheric pressure. The X-ray intensity with prepulse in helium was almost constant for any separation time during 1–50 ps. However, the prepulse enhancement in vacuum was reported to be higher and to have a peak in the function of the pulse separation time in the range of 30–50 ps.[65, 96] This result can be also explained with collision of diatomic molecules. In vacuum conditions, electrons generated by preplasma can expand from a few to several micrometers from the target surface because of the electron mean free path of below 1 mm to 100 mm. Then, the electrons in preplasma can be accelerated by the main pulse and produce X-rays. However, in helium at atmosphere pressure, the electrons in preplasma can travel only 1–2 μm from the surface because the electron mean free path is 1.01 μm. Almost all electrons in the preplasma interact with helium atoms and lose their energy. A small amount of electrons with very slow velocity remain in the near-surface region of the target and can be accelerated with the main pulse. These electrons produce the X-ray with a prepulse enhancement value of about 1.3. Even though a prepulse enhancement of 1.3 times was observed in helium at atmospheric pressure, it is better to construct the X-ray generation systems without the prepulse line. As shown in Fig. 3.15, there are some optical loss for building the prepulse line because of loss: 10% by the 1:9 beam splitter, 10% by the polarized beam splitter, and a few percents loss by the additional mirrors required to let the main pulse and prepulse pass through the same line. The total loss from constructing such a complex main pulse and prepulse line amounts to more than 30%. Thus, by removing the prepulse line and increasing the main laser power, an X-ray intensity 1.3 times higher than without prepulse with plasma power of 4.0×10^{16} Wμm^2/cm^2 can be obtained in helium at atmospheric pressure. Moreover, the extension oin pulse duration by the prepulse effect was expected under vacuum conditions; however, the pulse duration may not be prolonged by the prepulse effect in helium atmosphere according to the simple electron collision model. The schematic drawings of the model for the prepulse effect are shown in Fig. 3.16

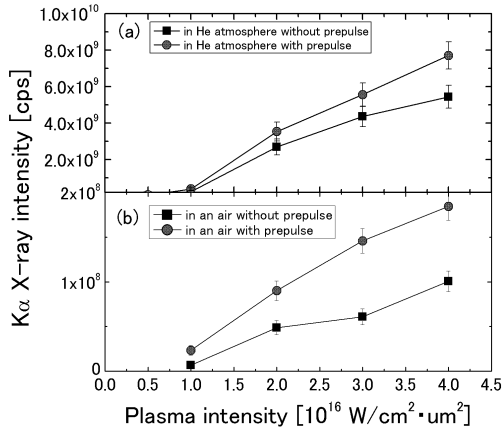

Figure 3.14: Prepulse plasma enhancement of Kα X-ray intensity (a) in helium atmosphere and (b) in air. The solid line with square symbols is the Kα X-ray yield without prepulse and the solid line with square symbol is the Kα X-ray intensity with prepulse enhancement effect.

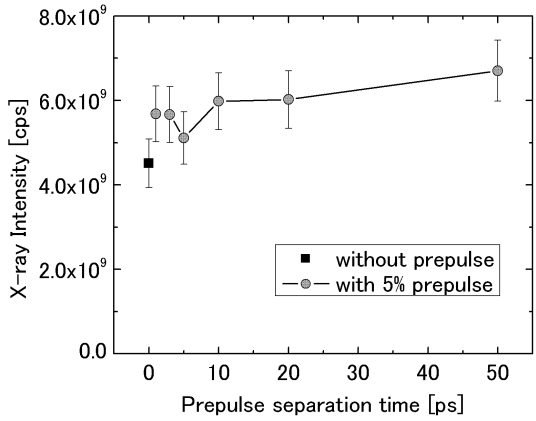

Figure 3.15: X-ray intensity as a function of the separation time between prepulse and main pulse at plasma intensity of 3.0 $\times$ 10^{16} Wμm^2/cm^2 in He at atmospheric pressure. The solid square point is the Kα X-ray yield without prepulse and the solid line with circle symbols is the Kα X-ray intensity with 5% prepulse enhancement effect. With 5% prepulse, the obtained intensity was 1.3 times higher regardless of the prepulse separation time.

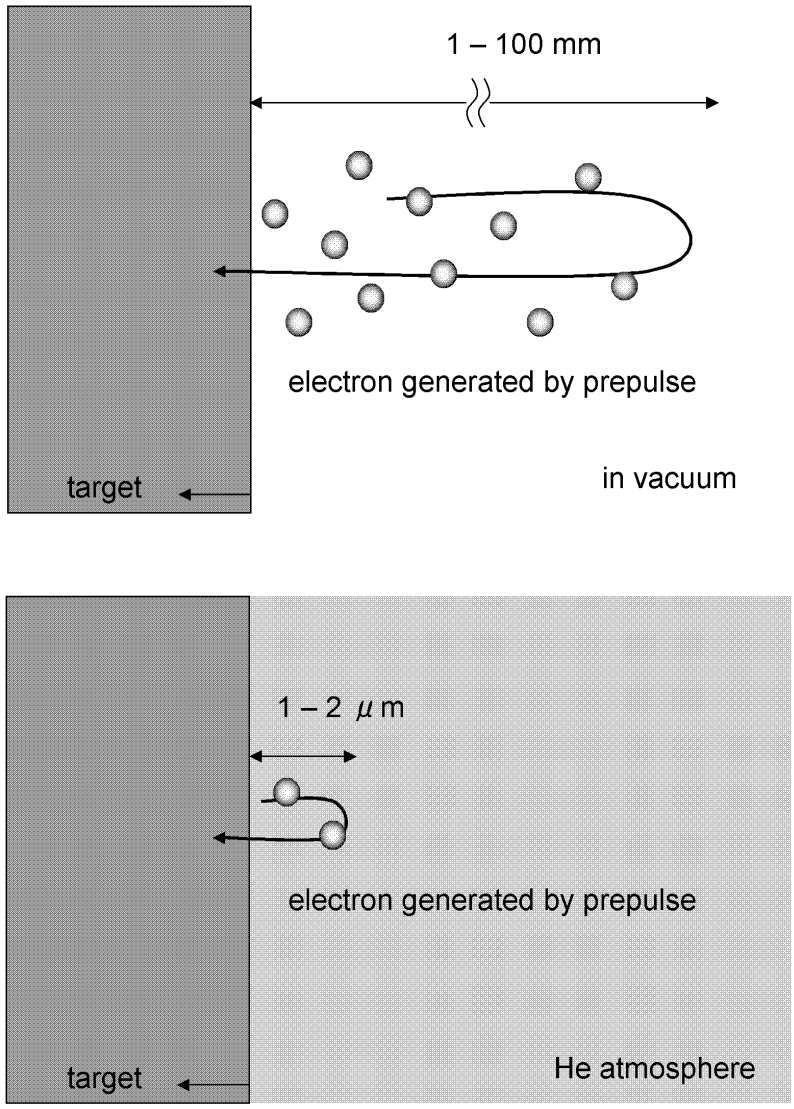

Figure 3.16: The effect of the prepulse considered based on the simple electron collision model.

3.6 Summary

In this chapter, high intensity Kα X-ray generation at a high repetition was demonstrated with table-top commercial ultrafast laser system in helium at atmospheric pressure. The effects of the ambient conditions and the prepulse for the X-ray radiation were also investigated.

1. The intensity of the generated Kα X-ray in helium at atmospheric pressure was 5.4×10^9 cps/sr with 1 kHz repetition rate and conversion efficiency of 5.0×10^{-6}. This X-ray intensity is close to that obtained in vacuum condition and is high enough for the time-resolved X-ray diffraction or other X-ray applications.

2. The normalized Kα X-ray conversion efficiency in various conditions indicated that the simple electron collision model could explain the relationship between the Kα X-ray conversion efficiency and the atmosphere near the target surface. In this model, it is suggested that the electron mean free path in the specific atmosphere and pressure is an important parameter in the generation of the ultrafast pulsed X-ray. The electron traveling length in ambient atmosphere was well fitted to 1–2 μm and the electron mean free path in helium atmospheric pressure was 1.01 μm.

3. It is suggested that the 20%–40% intensity (compared with the vacuum condition) ultrafast pulsed Kα X-ray is generated even in a helium ambient at 1.01×10^5 Pa by the simple electron collision model. It also suggested that helium gas is the most suitable gas for the in-air X-ray source.

4. The Kα X-ray intensity was enhanced with 4%–8% prepulse plasma into 7.7×10^9 cps/sr and 6.8×10^{-6} conversion efficiency. Regarding the prepulse, it would be better to construct a simpler X-ray generation system without the prepulse line because of the optical losses in the system.

5. Such a high-intensity, vacuum-free simple femtosecond X-ray source with a table-top laser could be a promising tool for time-resolved X-ray diffraction or other radiographic applications.

Chapter 4

Observation of Ultrafast Lattice Dynamics

There are two theories of X-ray diffraction: "the kinematic theory" [97, 98, 99] and "the dynamic theory" [100]. The kinematic theory, in the ideal case, describes the interaction of the X-ray with a single atom and derives the intensities of the resulting beams. The dynamic theory takes into account the multiple scattering resulting from the presence of many atoms. This theory requires a wave-mechanical treatment, since the scattering produces a background that very considerably modifies the intensity distributions. X-rays can usually be treated by means of the kinematic theory, unless the sample is very thick and has perfect crystallinity like single crystalline silicon. The first part of this chapter shows some fundamental principles of the kinetic theory of X-ray diffraction. The basic system for the X-ray diffraction measurements is also described. In the latter part of this chapter, the time-resolved X-ray diffraction measurements for cadmium telluride (CdTe) single crystal and vanadium dioxide (VO_2) thin film are presented

4.1 X-ray diffraction

4.1.1 Bragg's law

We cannot discuss X-ray diffraction in depth without mentioning Bragg's law. This gives the geometrical conditions under which a diffracted X-ray can be observed. Figure 4.1 shows rays diffracted from the lattice planes giving constructive interference. From Fig. 4.1, Bragg's law is expressed as:

$$2d \sin\theta = n\lambda, \tag{4.1}$$

where θ is glancing angle of the incident X-ray, which is known as the Bragg's angle, λ is the wavelength of the X-rays and d is the plane spacing. The

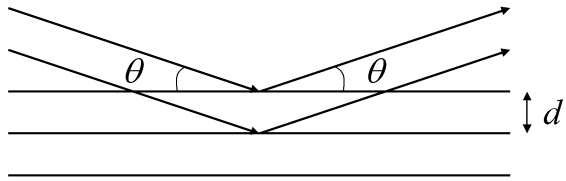

Figure 4.1: Bragg's law

value of n in Bragg's law can always be taken as unity, since any multiples of the wavelength can be accounted for in the diffraction indices h, k, l, which are known as Miller indices, of any particular reflection. For example, $n = 2$ for the planes h, k, l is equivalent to $n = 1$ for the planes $2h$, $2k$, $2l$.

4.1.2 Scattering of X-ray and structure factor

The scattering of X-rays from electrons is called Thomson scattering. It occurs because the electron oscillates in the electric field of the incoming X-ray beam and an oscillating electron charge emits electromagnetic waves. This electromagnetic radiation is called dipole radiation. Thus, X-rays are emitted from the electron at the same frequency as the primary X-rays; however, most electrons radiated π radians (180°) out of the phase with the incoming direction.

The X-ray intensity scattered from a scattering body which has arbitrary electron density can be described as the superposition of the overall scattering X-ray from the electrons in the scattering body. Figure 4.2 shows the X-ray scattering from a given scattering body, where $\vec{k_0}$ and $\vec{k}$ are the wave vectors of the incident X-rays and scattered X-ray. The frequencies of the incident X-ray and scattered X-ray are the same; therefore, the absolute values of $\vec{k_0}$ and $\vec{k}$ are expressed with the wavelength of the X-rays as

$$\mid \vec{k_0} \mid = \mid \vec{k} \mid = k = 1/\lambda. \tag{4.2}$$

The scattering vector $\vec{K}$ is defined with the scattering angle 2Θ as

$$\vec{K} \equiv \vec{k} - \vec{k_0}, \tag{4.3}$$

$$K = \mid \vec{K} \mid = 2k \sin\Theta = \frac{2\sin\Theta}{\lambda}. \tag{4.4}$$

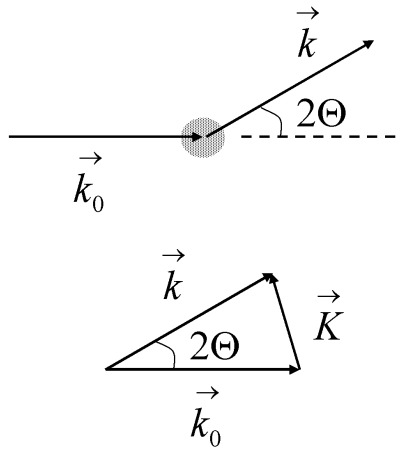

Figure 4.2: X-ray scattering from a given scattering body

As shown in Fig. 4.3, the path difference between the X-ray scattered at the position of origin (O) and at the position $\vec{r}$ away from the origin (P) is expressed as $\overline{\text{O'P}} - \overline{\text{OP'}}$. In Fig. 4.3,

$$\overline{\text{O'P}} = \frac{\vec{k_0} \cdot \vec{r}}{|\vec{k_0}|} = \frac{\vec{k_0} \cdot \vec{r}}{k}, \tag{4.5}$$

$$\overline{\text{OP'}} = \frac{\vec{k} \cdot \vec{r}}{|\vec{k}|} = \frac{\vec{k} \cdot \vec{r}}{k}; \tag{4.6}$$

therefore,

$$\overline{\text{O'P}} - \overline{\text{OP'}} = \frac{(\vec{k_0} - \vec{k}) \cdot \vec{r}}{k} = \frac{\vec{K} \cdot \vec{r}}{k} = -\lambda \vec{K} \cdot \vec{r}. \tag{4.7}$$

The phase difference ϕ between the X-rays scattered at the positions $\vec{r}$ away from each other is,

$$\phi = \frac{2\pi}{\lambda}(-\lambda \vec{K} \cdot \vec{r}) = -2\pi \vec{K} \cdot \vec{r}. \tag{4.8}$$

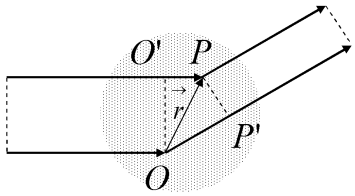

Figure 4.3: The path difference between the X-rays scattered from different points

The oscillation of the scattered X-ray at the position of $\vec{r}$ is proportional to the electron density $\rho(\vec{r})$; therefore, the superposition of the overall scattering X-ray from the electrons in the scattering body can be described as

$$F(\vec{K}) = \int_V \rho(\vec{r}) e^{-2\pi i \vec{K}\cdot\vec{r}} dv, \tag{4.9}$$

where $F(\vec{K})$ is called structure factor. $F(\vec{K})$ is also reduced to scale with the 3 dimensional axes x, y, z as;

$$F(K_x, K_y, K_z) = \int\int\int \rho(x, y, z) e^{-2\pi i(K_x x + K_y y + K_z z)} dxdydz. \tag{4.10}$$

The wave intensity is proportional to the square of the wave amplitude; therefore, the scattered X-ray intensity is proportional to the square of absolute value of the structure factor $\mid F(\vec{K}) \mid^2$.

4.1.3 Scattering from atoms

There is a path difference between X-ray scattered from different parts of the same atom, resulting in destructive interference that depends on the scattering angle. This reduction in X-rays scattered from an atom with increasing angle is described by the atomic scattering factor. The atomic scattering factor is expressed as a function of $K = 2(\sin\Theta)/\lambda$ or $(\sin\theta)/\lambda$. The values of the atomic scattering factor of several atoms and ions are shown in the "International Tables for Crystallography Vol. C". [101] The

scattering factor at zero scattering angle is equal to the number of electron in atoms. Atoms are subject to thermal vibration, and this movement modifies the scattering factor and must be taken into account. The atomic scattering factor of the atoms ranged from hydrogen to neon is shown in Fig. 4.4 and Fig. 4.5.

When the X-ray frequency is close to the resonance frequency of an electron, anomalous scattering takes place and the atomic scattering factor is altered In this case, only some of the electrons in the atom will be affected and scatter the X-ray roughly $\pi/2$ out of the phase with the incident X-ray. Electrons scattering exactly $\pi/2$ out of phase are represented mathematically with an imaginary part of the scattering factor and they cease to contribute to the real part.

Element	H	He	Li	Be	B	C	N	O	F	Ne
Z	1	2	3	4	5	6	7	8	9	10
Method	exact	relativisic Hartree-Fock								
$\sin\theta / \lambda$										
0.00	1.000	2.000	3.000	4.000	5.000	6.000	7.000	8.000	9.000	10.000
0.02	0.991	1.993	2.947	3.950	4.954	5.958	6.963	7.967	8.970	9.973
0.04	0.966	1.972	2.802	3.807	4.820	5.837	6.855	7.869	8.881	9.891
0.06	0.925	1.939	2.606	3.592	4.613	5.645	6.682	7.712	8.736	9.757
0.08	0.872	1.893	2.400	3.336	4.352	5.396	6.453	7.501	8.541	9.576
0.10	0.811	1.837	2.215	3.065	4.060	5.107	6.180	7.245	8.302	9.351
0.12	0.744	1.772	2.065	2.804	3.756	4.794	5.875	6.954	8.026	9.090
0.14	0.676	1.701	1.950	2.569	3.459	4.472	5.551	6.637	7.721	8.799
0.16	0.608	1.624	1.863	2.365	3.179	4.153	5.218	6.304	7.395	8.483
0.18	0.542	1.543	1.796	2.197	2.924	3.847	4.886	5.964	7.055	8.150
0.20	0.481	1.460	1.742	2.060	2.699	3.560	4.563	5.623	6.709	7.805
0.25	0.350	1.254	1.626	1.828	2.263	2.949	3.825	4.808	5.851	6.928
0.30	0.251	1.060	1.513	1.692	1.979	2.494	3.219	4.089	5.054	6.079
0.35	0.180	0.887	1.393	1.600	1.799	2.171	2.747	3.489	4.353	5.302
0.40	0.130	0.738	1.270	1.520	1.681	1.948	2.393	3.006	3.759	4.617
0.45	0.095	0.613	1.149	1.443	1.596	1.794	2.132	2.629	3.270	4.029
0.50	0.071	0.509	1.033	1.362	1.526	1.685	1.942	2.338	2.874	3.535
0.55	0.053	0.423	0.924	1.279	1.463	1.603	1.802	2.115	2.559	3.126
0.60	0.040	0.353	0.823	1.195	1.402	1.537	1.697	1.946	2.309	2.822
0.65	0.031	0.295	0.732	1.112	1.339	1.479	1.616	1.816	2.112	2.517
0.70	0.024	0.248	0.650	1.030	1.276	1.426	1.551	1.714	1.956	2.296
0.80	0.015	0.177	0.512	0.876	1.147	1.322	1.445	1.568	1.735	1.971
0.90	0.010	0.129	0.404	0.740	1.020	1.219	1.353	1.463	1.588	1.757
1.00	0.007	0.095	0.320	0.622	0.900	1.114	1.265	1.377	1.482	1.609
1.10	0.005	0.072	0.255	0.522	0.790	1.012	1.172	1.298	1.398	1.502
1.20	0.003	0.055	0.205	0.439	0.690	0.914	1.090	1.221	1.324	1.418
1.30	0.003	0.042	0.165	0.369	0.602	0.822	1.004	1.145	1.254	1.346
1.40	0.002	0.033	0.134	0.311	0.524	0.736	0.921	1.070	1.186	1.280
1.50	0.001	0.026	0.110	0.263	0.457	0.659	0.843	0.997	1.120	1.218
1.60		0.021	0.091	0.223	0.398	0.588	0.769	0.926	1.055	1.158
1.70		0.017	0.075	0.190	0.347	0.525	0.700	0.857	0.990	1.099
1.80		0.014	0.063	0.163	0.304	0.468	0.636	0.792	0.928	1.041
1.90		0.011	0.053	0.139	0.266	0.418	0.578	0.731	0.868	0.984
2.00		0.010	0.044	0.120	0.233	0.373	0.525	0.674	0.810	0.929

Figure 4.4: Atomic scattering factors for various elements

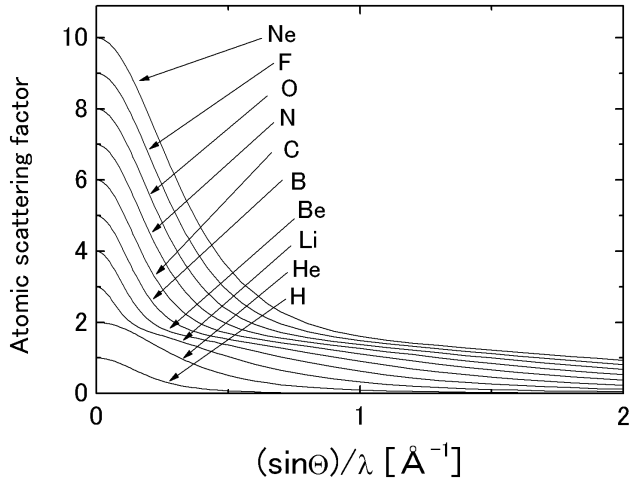

Figure 4.5: The atomic scattering factor as a function of the $\sin\theta/\lambda$ ratio

4.1.4 Scattering from the crystal

A crystal consists of unit cells with periodical repetition. An X-ray diffraction pattern is therefore the product of the scattering from the unit cell and the reciprocal lattice. The axes of the unit cell are expressed as $\vec{a}$, $\vec{b}$, and $\vec{c}$. Representing the average position of the jth atom in the unit cell represents as $\langle\vec{r}_j\rangle$, the average position of the j-th atom in the crystal can be determined as

$$r_{\vec{uvwj}} = u\vec{a} + v\vec{b} + w\vec{c} + \langle\vec{r}_j\rangle \tag{4.11}$$

where u, v, and w are integers. The electron density at position of $r_{\vec{uvwj}}$ can be also described based on the periodical unit cells as $\rho_j(\vec{r} - r_{\vec{uvwj}})$, and the electron density in the crystal can be expressed as

$$\begin{aligned}\rho_{\text{total}} &= \sum_{uvw}\sum_{j=1}^{M}\rho_j(\vec{r} - r_{\vec{uvwj}}) \\ &= \sum_{uvw}\sum_{j=1}^{M}\rho_j(\vec{r} - u\vec{a} - v\vec{b} - w\vec{c} - \langle\vec{r}_j\rangle),\end{aligned} \tag{4.12}$$

where the unit cell contains M atoms.

The intensity of X-ray scattering is represented by the structure factor; therefore,

$$\begin{aligned} F_{\text{total}} &= \int_{R^3} \rho_{\text{total}}(\vec{r}) \exp(2\pi i \vec{K} \cdot \vec{r}) dv, \\ &= \int_{R^3} \exp(2\pi i \vec{K} \cdot \vec{r}) \sum_{uvw} \sum_{j=1}^{M} \rho_j(\vec{r} - u\vec{a} - v\vec{b} - w\vec{c} - \langle \vec{r}_j \rangle) dv, \\ &= \sum_{uvw} \sum_{j=1}^{M} \int_{R^3} \exp(2\pi i \vec{K} \cdot \vec{r}) \rho_j(\vec{r} - u\vec{a} - v\vec{b} - w\vec{c} - \langle \vec{r}_j \rangle) dv. \end{aligned} \tag{4.13}$$

$$\begin{aligned} F_{\text{total}} &= \sum_{uvw} \sum_{j=1}^{M} \int_{R^3} \exp\left[2\pi i \vec{K} \cdot (\vec{r} + u\vec{a} + v\vec{b} + w\vec{c} + \langle \vec{r}_j \rangle)\right] \rho_j(\vec{r}) dv \\ &= \sum_{uvw} \exp\left[2\pi \vec{K} \cdot (u\vec{a} + v\vec{b} + w\vec{c})\right] \\ &\quad \times \sum_{j=1}^{M} \exp\left[2\pi \vec{K} \cdot \langle \vec{r}_j \rangle\right] \int_{R^3} \rho_j(\vec{r}) \exp(2\pi i \vec{K} \cdot \vec{r}) dv, \end{aligned} \tag{4.14}$$

after performing the substitution of $\vec{r}$ into $\vec{r} + u\vec{a} + v\vec{b} + w\vec{c} + \langle \vec{r}_j \rangle$. In this equation, the term $\int_{R^3} \rho_j(\vec{r}) \exp(2\pi i \vec{K} \cdot \vec{r})$ is the atomic scattering factor, defined as

$$\int_{R^3} \rho_j(\vec{r}) \exp(2\pi i \vec{K} \cdot \vec{r}) = f_j(\vec{K}). \tag{4.15}$$

In Eq. (4.14), the term $\sum_{uvw} \exp[2\pi \vec{K} \cdot (u\vec{a} + v\vec{b} + w\vec{c})]$ is known as Laue's law, which is equivalent to Bragg's law:

$$\sum_{uvw} \exp\left[2\pi \vec{K} \cdot (u\vec{a} + v\vec{b} + w\vec{c})\right] = G(\vec{K}). \tag{4.16}$$

Accordingly, the X-ray scattering factor from the crystal, F_{total} can be expressed by:

$$F_{\text{total}} = G(\vec{K}) \sum_{j=1}^{M} f_j(\vec{K}) \exp\left[2\pi \vec{K} \cdot \langle \vec{r}_j \rangle\right]. \tag{4.17}$$

The Bragg angle of the diffraction line depends on the Laue function $G(\vec{K})$; more specifically, it depends on the size and geometry of the unit cell. The intensity of the diffraction line strongly depends on the term of $\sum_{j=1}^{M} f_j(\vec{K}) \exp[2\pi \vec{K} \cdot \langle \vec{r}_j \rangle]$ in Eq. (4.17).

4.1.5 Isotropic thermal effect

Atoms or molecules in a crystal vibrate thermally and randomly at a given temperature. The effect of this thermal effect should be taken into account for the Eq. (4.17). The isotropic random displacement of atoms by the thermal effect Δr_{uvwj} can contribute to Eq. (4.11), and r_{uvwj} can be expressed as

$$r_{uvwj} = u\vec{a} + v\vec{b} + w\vec{c} + \langle \vec{r}_j \rangle + \Delta r_{uvwj}. \tag{4.18}$$

Therefore, F_{total} (Eq. (4.17)) is converted to the following equation,

$$\begin{aligned} F_{\text{total}} &= G(\vec{K}) \sum_{j=1}^{M} f_j(\vec{K}) \exp\left[2\pi \vec{K} \cdot (\langle \vec{r}_j \rangle + \Delta r_{uvwj})\right] \\ &= G(\vec{K}) \sum_{j=1}^{M} f_j(\vec{K}) \exp\left[2\pi \vec{K} \cdot \langle \vec{r}_j \rangle\right] \exp\left[2\pi \vec{K} \cdot \Delta r_{uvwj}\right]. \end{aligned} \tag{4.19}$$

If the probability density distribution of the displacement of the j-th atom in a unit cell (Δv) can be expressed to be $g_j(\Delta \vec{r})$ as a function of the normalized atomic displacement (Δr), Eq. (4.19) is reduced to:

$$\begin{aligned} F_{\text{total}} = G(\vec{K}) &\sum_{j=1}^{M} f_j(\vec{K}) \exp\left[2\pi \vec{K} \cdot \langle \vec{r}_j \rangle\right] \\ &\times \int_{R^3} g_j(\Delta \vec{r}) \exp\left[2\pi \vec{K} \cdot \Delta \vec{r}_j\right] d(\Delta v), \end{aligned} \tag{4.20}$$

where the thermal atomic displacements for each atom are independent of each other. The term $\int_{R^3} g_j(\Delta \vec{r}) \exp[2\pi \vec{K} \cdot \Delta \vec{r}_j] d(\Delta v)$ in Eq. (4.20) represents the thermal effect and is called the "temperature factor", the " Debye-Waller factor " or the "atomic displacement factor". The temperature factor is defined as $T_j(\vec{K})$,

$$T_j(\vec{K}) \equiv \int_{R^3} g_j(\Delta \vec{r}) \exp[2\pi \vec{K} \cdot \Delta \vec{r}_j] d(\Delta v). \tag{4.21}$$

The simplest model for thermal vibration is the harmonic oscillator, which is simple harmonic motion with a certain frequency. The energy of the harmonic oscillator is represented as $\frac{1}{2} k x_{\max}^2$, where $x_{\max}$ is the amplitude of vibration and k is the force constant in an elastic body. The energy of vibration (E) in a crystal at a given temperature T can be described with the Maxwell–Boltzmann distribution as follows:

$$f_{\text{MB}}(E) = e^{-E/k_B T}, \tag{4.22}$$

where k_B is the Boltzmann constant ($1.3806503 \times 10^{-23}$ J/K). Therefore, the distribution of the atomic vibration in the crystal can be described with the following Gaussian distribution:

$$f_{\mathrm{MB}}(\Delta r) = \exp\left[-\frac{k\Delta r^2}{2k_B T}\right]. \tag{4.23}$$

The standard deviation of this distribution is $\sqrt{k_B T/k}$.

When the atomic vibration is considered as an isotropic 3-dimensional harmonic oscillation, the probability density distribution of the displacement of the j-th atom in a unit cell ($g_j(\Delta\vec{r})$) is represented with the mean-square displacement (U_j):

$$g_j(\Delta\vec{r}) = \frac{1}{(2\pi)^{3/2} U_j^{3/2}} \exp\left[-\frac{\Delta r^2}{2U_j}\right] \tag{4.24}$$

$$\begin{aligned} T_j(\vec{K}) &\equiv \int_{R^3} g_j(\Delta\vec{r}) \exp\left[2\pi i\vec{K}\cdot\Delta\vec{r}\right] d(\Delta v), \\ &= \exp\left[-2\pi^2 K^2 U_j\right], \\ &= \exp\left[-\frac{8\pi^2 U_j sin^2\Theta}{\lambda^2}\right]. \end{aligned} \tag{4.25}$$

In the kinetic theory, the intensity of X-ray diffraction (I) is expressed as the square of the structure factor and is reduced to:

$$\begin{aligned} I &= \left\langle F_{\mathrm{total}}(\vec{K})\right\rangle^2 \\ \left\langle F_{\mathrm{total}}(\vec{K})\right\rangle &= G(\vec{K}) \sum_{j=1}^{M} f_j(\vec{K}) T_j(\vec{K}) \exp\left(2\pi i\vec{K}\cdot\langle\vec{r}_j\rangle\right). \end{aligned} \tag{4.26}$$

In contrast, the intensity of X-ray diffraction is proportional to the structure factor in the dynamical theory [100].

4.1.6 Anisotropic thermal effect

When the atoms vibrate anisotropically in a crystal, the mean-square displacement (U_j) is defined as a 3-dimentional matrix:

$$\boldsymbol{U_j} = \begin{pmatrix} U_{jxx} & U_{jxy} & U_{jxz} \\ U_{jyx} & U_{jyy} & U_{jyz} \\ U_{jzx} & U_{jzy} & U_{jzz} \end{pmatrix}, \tag{4.27}$$

where

$$\begin{aligned} U_{jxx} &\equiv \int_{R^3} x^2 g_j(\vec{r}) d\vec{v}, \\ U_{jyy} &\equiv \int_{R^3} y^2 g_j(\vec{r}) d\vec{v}, \\ U_{jzz} &\equiv \int_{R^3} z^2 g_j(\vec{r}) d\vec{v}, \\ U_{jxy} = U_{jyx} &\equiv \int_{R^3} (xy) g_j(\vec{r}) d\vec{v}, \\ U_{jxz} = U_{jzx} &\equiv \int_{R^3} (xz) g_j(\vec{r}) d\vec{v}, \\ U_{jyz} = U_{jzy} &\equiv \int_{R^3} (yz) g_j(\vec{r}) d\vec{v}. \end{aligned} \tag{4.28}$$

The eigenvalue and the eigenvector of the matrix can be defined as U_1,U_2,U_3 and $\vec{p}_1$, $\vec{p}_2$, $\vec{p}_3$, respectively, where the eigenvectors are normalized and chosen as orthogonal to each other; therefore,

$$\vec{p}_1 \equiv \begin{pmatrix} p_{1x} \\ p_{1y} \\ p_{1z} \end{pmatrix}, \vec{p}_2 \equiv \begin{pmatrix} p_{2x} \\ p_{2y} \\ p_{2z} \end{pmatrix}, \vec{p}_3 \equiv \begin{pmatrix} p_{3x} \\ p_{3y} \\ p_{3z} \end{pmatrix}, \tag{4.29}$$

$$\begin{aligned} \vec{p}_1^t \boldsymbol{U_j} \vec{p}_1 &= U_1, \\ \vec{p}_2^t \boldsymbol{U_j} \vec{p}_2 &= U_2, \\ \vec{p}_3^t \boldsymbol{U_j} \vec{p}_3 &= U_3, \end{aligned} \tag{4.30}$$

$$\boldsymbol{P}^t \boldsymbol{U_j} \boldsymbol{P} = \begin{pmatrix} U_1 & 0 & 0 \\ 0 & U_2 & 0 \\ 0 & 0 & U_3 \end{pmatrix}, \tag{4.31}$$

where

$$\boldsymbol{P} = \begin{pmatrix} p_{1x} & p_{2x} & p_{3x} \\ p_{1y} & p_{2y} & p_{3y} \\ p_{1z} & p_{2z} & p_{3z} \end{pmatrix}. \tag{4.32}$$

The matrix $\boldsymbol{P}$ is an orthonormal matrix ($\boldsymbol{P}^t = \boldsymbol{P}^{-1}$); therefore,

$$\boldsymbol{U_j} = \boldsymbol{P} \begin{pmatrix} U_1 & 0 & 0 \\ 0 & U_2 & 0 \\ 0 & 0 & U_3 \end{pmatrix} \boldsymbol{P}^t. \tag{4.33}$$

The scattering vector $\vec{K} = (K_x, K_y, K_z)$ can be converted with the eigenvectors to $\vec{K}' = (K_X, K_Y, K_Z)$:

$$\vec{K} = \begin{pmatrix} K_x \\ K_y \\ K_z \end{pmatrix} = K_X\vec{p_1} + K_Y\vec{p_2} + K_Z\vec{p_3} = \boldsymbol{P}\begin{pmatrix} K_X \\ K_Y \\ K_Z \end{pmatrix}. \quad (4.34)$$

When the atoms in a crystal vibrate in (X, Y, Z) directions at the mean-square displacement of (U_1, U_2, U_3) as harmonic oscillator, the probability density distribution of the displacement of the jth atom in a unit cell $(g_j(\Delta\vec{r}))$ is represented as:

$$g_j(\Delta\vec{r}) = \frac{1}{(2\pi)^{3/2}U_1^{1/2}U_2^{1/2}U_3^{1/2}} \exp\left[-\frac{\Delta X^2}{2U_1} - \frac{\Delta Y^2}{2U_2} - \frac{\Delta Z^2}{2U_3}\right]. \quad (4.35)$$

The isotropic temperature factor can be calculated analytically as:

$$\begin{aligned}
T_j(\vec{K}) &= \iiint g_j(\Delta\vec{r}) \exp\left(2\pi i\vec{K}\cdot\Delta\vec{r}\right) d\Delta X d\Delta Y d\Delta Z \\
&= \frac{1}{(2\pi)^{3/2}U_1^{1/2}U_2^{1/2}U_3^{1/2}} \iiint \exp\left[-\frac{\Delta X^2}{2U_1} - \frac{\Delta Y^2}{2U_2} - \frac{\Delta Z^2}{2U_3}\right] \\
&\quad \times \exp\left[2\pi i\left(K_X\Delta X + K_Y\Delta Y + K_Z\Delta Z\right)\right] d\Delta X d\Delta Y d\Delta Z \\
&= \exp\left[-2\pi^2\left(K_X^2U_1 + K_Y^2U_2 + K_Z^2U_3\right)\right] \\
&= \exp\left[-2\pi^2\begin{pmatrix} K_X & K_Y & K_Z \end{pmatrix}\begin{pmatrix} U_1 & 0 & 0 \\ 0 & U_2 & 0 \\ 0 & 0 & U_3 \end{pmatrix}\begin{pmatrix} K_X \\ K_Y \\ K_Z \end{pmatrix}\right] \\
&= \exp\left[-2\pi^2\begin{pmatrix} K_x & K_y & K_z \end{pmatrix}\boldsymbol{P}^t\begin{pmatrix} U_1 & 0 & 0 \\ 0 & U_2 & 0 \\ 0 & 0 & U_3 \end{pmatrix}\boldsymbol{P}\begin{pmatrix} K_x \\ K_y \\ K_z \end{pmatrix}\right] \\
&= \exp\left[-2\pi^2\begin{pmatrix} K_x & K_y & K_z \end{pmatrix}\begin{pmatrix} U_{jxx} & U_{jxy} & U_{jxz} \\ U_{jxy} & U_{jyy} & U_{jyz} \\ U_{jxz} & U_{jyz} & U_{jzz} \end{pmatrix}\begin{pmatrix} K_x \\ K_y \\ K_z \end{pmatrix}\right] \\
&= \exp[-2\pi^2(U_{jxx}K_x^2 + U_{jyy}K_y^2 + U_{jzz}K_z^2 \\
&\quad + 2U_{jxy}K_xK_y + 2U_{jyz}K_yK_z + 2U_{jzx}K_zK_x)]. \quad (4.36)
\end{aligned}$$

4.1.7 Laue condition

In Eq. (4.17), $\vec{K}$ can be reduced as

$$\vec{K} = h\vec{a}^* + k\vec{b}^* + l\vec{c}^* \quad (4.37)$$

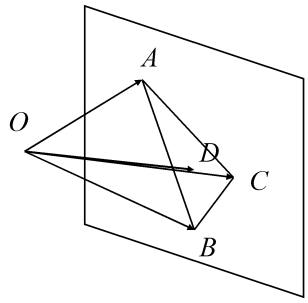

Figure 4.6: The relationship between the $\vec{K}$ vector and a given lattice spacing of a unit cell

where

$$\begin{aligned}\vec{a}^* &= \frac{\vec{b}\times\vec{c}}{\vec{a}\cdot(\vec{b}\times\vec{c})}\\ \vec{b}^* &= \frac{\vec{c}\times\vec{a}}{\vec{b}\cdot(\vec{c}\times\vec{a})}\\ \vec{c}^* &= \frac{\vec{a}\times\vec{b}}{\vec{c}\cdot(\vec{a}\times\vec{b})}.\end{aligned} \tag{4.38}$$

The relationship of the $\vec{K}$ vector and a given lattice spacing of a unit cell is shown in Fig. 4.6.

In Fig. 4.6, the lattice spacing is $\overrightarrow{OD}$, the perpendicular line from O to the plane ABC. Thus, $\overrightarrow{OD}$ is perpendicular to $\overrightarrow{AB}$, $\overrightarrow{BC}$ and $\overrightarrow{CA}$, and therefore,

$$\begin{aligned}\overrightarrow{OD} &\parallel (\overrightarrow{AB}\times\overrightarrow{BC})\\ &\parallel (\overrightarrow{OB}-\overrightarrow{OA})\times(\overrightarrow{OC}-\overrightarrow{OB})\\ &\parallel (\frac{\vec{b}}{k}-\frac{\vec{a}}{h})\times(\frac{\vec{c}}{l}-\frac{\vec{b}}{k})\\ &\parallel \frac{\vec{b}\times\vec{c}}{kl}-\frac{\vec{a}\times\vec{c}}{hl}-\frac{\vec{b}\times\vec{a}}{hk}\\ &\parallel \frac{\vec{a}\cdot(\vec{b}\times\vec{c})}{hkl}(h\vec{a}^*+k\vec{b}^*+l\vec{c}^*)\parallel\vec{K}.\end{aligned} \tag{4.39}$$

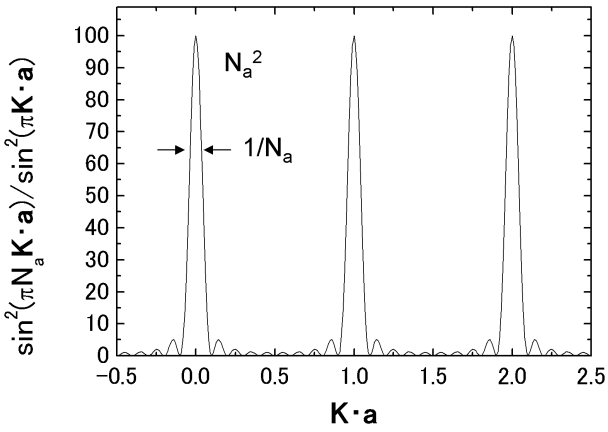

Figure 4.7: The Laue function

$\overrightarrow{OD}$ is parallel to $\vec{K}$ vector. The length of $\overrightarrow{OD}$ is

$$|\overrightarrow{OD}| = d_{hkl} = \frac{\vec{a}}{h}\frac{\vec{K}}{K} = \frac{\vec{a}\cdot\vec{K}}{h}\frac{1}{K} = \frac{1}{K} = \frac{\lambda}{2\sin\Theta}, \tag{4.40}$$

$$2d_{hkl}\sin\Theta = \lambda. \tag{4.41}$$

Thus, Laue's law is equivalent to Bragg's law.

When the crystal has finite size, i. e., the unit cell size of N_a, N_b, N_c to $\vec{a}$, $\vec{b}$, $\vec{c}$ directions, the Laue function is calculated as

$$\begin{aligned} G(\vec{K}) &= \sum_{u=0}^{N_a-1}\sum_{v=0}^{N_b-1} sum_{w=0}^{N_c-1} \exp\left[2\pi i\vec{K}\cdot\left(u\vec{a}+v\vec{b}+w\vec{c}\right)\right] \\ &= \sum_{u=0}^{N_a-1}\exp\left(2\pi iu\vec{K}\cdot\vec{a}\right)\sum_{v=0}^{N_b-1}\exp\left(2\pi iv\vec{K}\cdot\vec{b}\right)\sum_{u=0}^{N_c-1}\exp\left(2\pi iw\vec{K}\cdot\vec{c}\right) \\ &= \frac{\exp\left(2\pi iN_a\vec{K}\cdot\vec{a}\right)-1}{\exp\left(2\pi i\vec{K}\cdot\vec{a}\right)-1}\frac{\exp\left(2\pi iN_b\vec{K}\cdot\vec{b}\right)-1}{\exp\left(2\pi i\vec{K}\cdot\vec{b}\right)-1}\frac{\exp\left(2\pi iN_c\vec{K}\cdot\vec{c}\right)-1}{\left(\exp 2\pi i\vec{K}\cdot\vec{c}\right)-1}. \end{aligned} \tag{4.42}$$

The intensity of the X-ray diffraction is proportional to $|G(\vec{K})|^2$; therefore,

$$\begin{aligned}\frac{|\exp\left(2\pi i N_a \vec{K}\cdot\vec{a}\right)-1|^2}{|\exp\left(2\pi i \vec{K}\cdot\vec{a}\right)-1|^2} &= \frac{\left[\exp\left(-2\pi i N_a \vec{K}\cdot\vec{a}\right)-1\right]\left[\exp\left(2\pi i N_a \vec{K}\cdot\vec{a}\right)-1\right]}{\left[\exp\left(-2\pi i \vec{K}\cdot\vec{a}\right)-1\right]\left[\exp\left(2\pi i \vec{K}\cdot\vec{a}\right)-1\right]} \\ &= \frac{2-2\cos\left(2\pi N_a \vec{K}\cdot\vec{a}\right)}{2-2\cos\left(2\pi \vec{K}\cdot\vec{a}\right)} \\ &= \frac{1-1\cos\left(2\pi N_a \vec{K}\cdot\vec{a}\right)}{1-1\cos\left(2\pi \vec{K}\cdot\vec{a}\right)} \\ &= \frac{\sin^2\left(\pi N_a \vec{K}\cdot\vec{a}\right)}{\sin^2\left(\pi \vec{K}\cdot\vec{a}\right)}, \end{aligned} \tag{4.43}$$

$$|G(\vec{K})|^2 = \frac{\sin^2\left(\pi N_a \vec{K}\cdot\vec{a}\right)}{\sin^2\left(\pi \vec{K}\cdot\vec{a}\right)}\frac{\sin^2\left(\pi N_b \vec{K}\cdot\vec{b}\right)}{\sin^2\left(\pi \vec{K}\cdot\vec{b}\right)}\frac{\sin^2\left(\pi N_c \vec{K}\cdot\vec{c}\right)}{\sin^2\left(\pi \vec{K}\cdot\vec{c}\right)}. \tag{4.44}$$

The term $\frac{\sin^2\left(\pi N_a \vec{K}\cdot\vec{a}\right)}{\sin^2\left(\pi \vec{K}\cdot\vec{a}\right)}$ is shown in Fig. 4.7 as a function of $\vec{K}\cdot\vec{a}$. In Fig. 4.7, the peak intensity of the Laue function was calculated to be N_a and the full width half maximum (FWHM) is $\sim 1/N_a$. The integral intensity of the Laue function is proportional to N_a. In the case of $N_a \sim 1000$, the FWHM of the Laue function is enough small and the FWHM of the diffraction line is determined by the crystallinity of the crystal.

4.2 X-ray diffraction systems

4.2.1 Static X-ray diffractometer

Prior to performing time-resolved X-ray diffraction measurements we performed static X-ray diffraction measurements. The schematic design of the static X-ray diffractometer (ATX-G from Rigaku Co.) is shown in Fig. 4.8. Electrons emitted from the tungsten filament (300 mA) are accelerated to 50 keV with static electric field and focused onto a rotating copper target, where the Cu (K_α and K_β) X-ray and bremsstrahlung X ray are emitted. The X-rays are aligned with a boron carbide (B_4C) and tungsten (W) multilayer X-ray mirror, collimated with slits and focused onto the sample. The diffracted X-ray is detected by a solid scintillation counter. The divergence angle of the X-ray is about 0.05°.

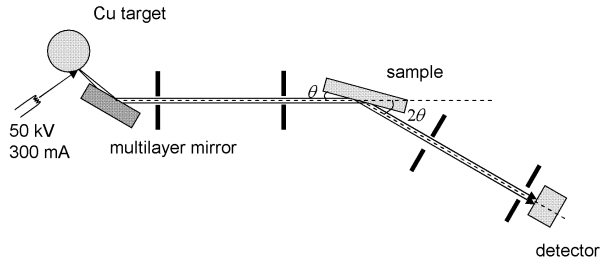

Figure 4.8: The experimental setup for static X-ray diffraction

4.2.2 Ultrafast X-ray diffraction system

Time-resolved X-ray diffraction measurements were performed in air using a laser-plasma-induced X-ray source of Cu Kα_1 and Kα_2 radiation at 1 kHz, generated by focusing a millijoule femtosecond laser onto a rotating copper target in helium ambient, as described in chapter 3. The experimental setup for the time-resolved X-ray diffraction is shown in Fig. 4.9. The femtosecond optical pulses at wavelength of 800 nm generated from the mode-rocked Ti: sapphire laser and regenerative amplifier were split into pump pulse and probe pulse with a polarized beam splitter. The contrast of the pump and probe pulse intensity was changed continuously from 3:7 to 1:9 by rotating the polarization with a $\lambda/2$ waveplate. The probe pulse at a laser intensity of $\sim$2 mJ/pulse was focused into the rotating copper target with an infrared achromatic lens (f = 40 mm) as described in section 3.3. The probing X-ray radiation emitted over a range of 2π steradians was collimated using slits with 0.3 mm width and 1 mm height, and was focused on a sample. The pulse width of the pulsed X-ray was estimated to be about 200 fs, and the time-resolution was about 1–3 ps, determined by considering the geometry of the X-ray divergence angle as shown in Fig. 4.9. The diffracted X-ray was detected using a charge coupled device camera and its intensity was monitored with a PIN-Si photodiode. The pump pulse passed through an optical delay line and was focused with a telescope. The area excited by the pump pulse had a 1.7 mm diameter and was larger than the X-ray-probed area.

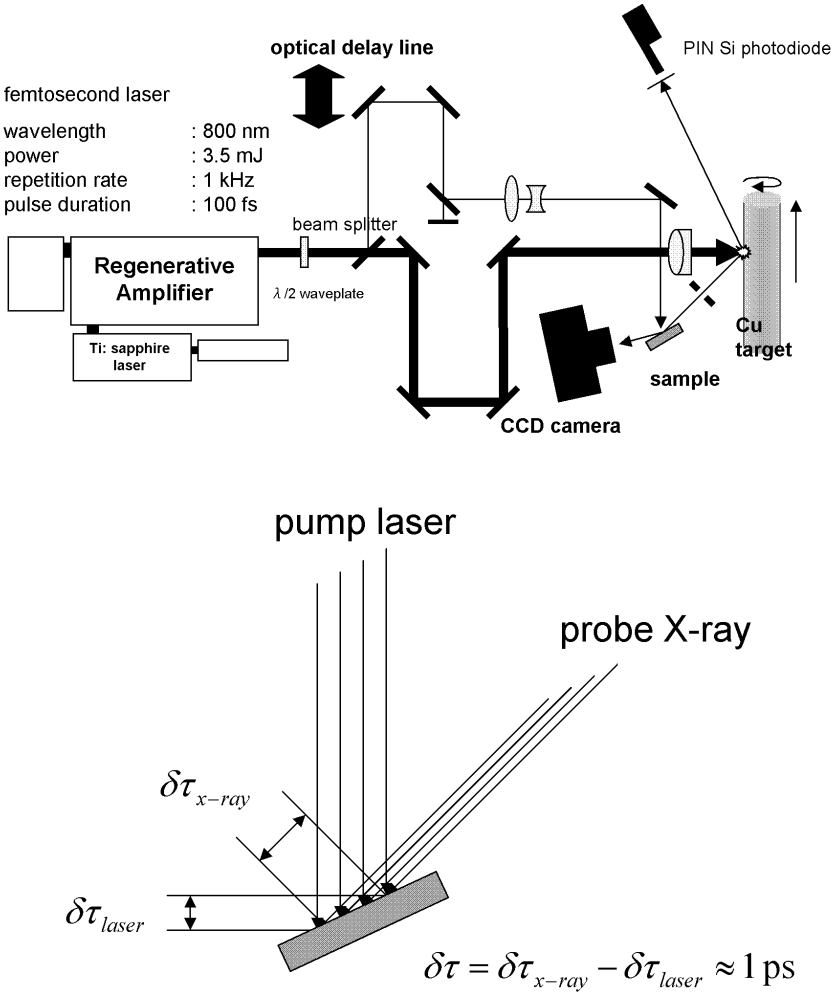

Figure 4.9: The experimental setup for the time-resolved X-ray diffraction

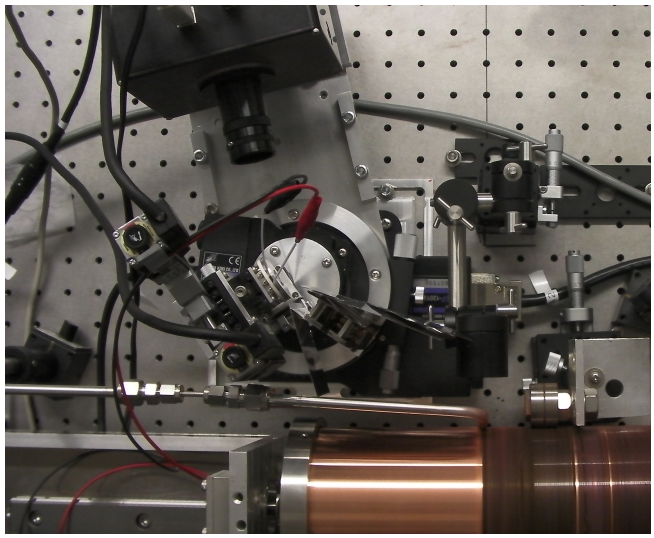

Figure 4.10: The photograph of the time-resolved X-ray diffraction system

4.3 Thermal effect in CdTe single crystal

In this section, we describe the characterization of the photo-excited thermal process in a cadmium telluride (CdTe) single crystal using the tabletop in-air time-resolved X-ray diffraction measurement. This study is the first application of an in-air ultrafast pulsed X-ray source with a tabletop laser for the time-resolved X-ray diffraction measurements. CdTe is a suitable material for time-resolved X-ray diffraction because the penetrating depths of probing X-ray and pumping infrared light are almost the same, about 1 μm. [80, 102] CdTe is also one of the promising materials for the solar cells, and the photo-electrical and photo-thermal properties have been extensively studied. [103, 104, 105]

The crystallinity of the sample can be estimated by the X-ray diffraction line width. The line width of X-ray diffraction from the single crystalline Si(111) plane was measured to be ∼0.002, which well corresponded to the value from the dynamical theory of X-ray diffraction. [106, 107] In contrast, the line width of X-ray diffraction from the single crystalline CdTe(111) plane was measured to be ∼0.017. The CdTe(111) sample had non-perfect but good crystallinity; therefore, both the kinetic theory and dynamical theory of X-ray diffraction could be applied. In the following passage, the kinetic theory of X-ray diffraction was applied for the analysis of the lattice

dynamics of CdTe.

Diffraction lines were captured before and during excitation with a varying delay between pump and probe pulses ranging between -360 and +360 ps, with 30 ps steps. X-ray pulses of 60,000 shots were accumulated to take each diffraction image. The Kα_1 and Kα_2 X-ray diffraction lines from CdTe (111) plane are shown in Fig. 4.11; and a clear image with sufficient signal-to-noise ratio was obtained. Figure 4.12 shows the changes in the integrated intensity of Kα X-ray diffraction lines as a function of the delay time. The CdTe (111) crystal was excited by about 200 fs pump pulse at the power density of 3 mJ/cm^2. As shown in Fig. 4.12, the intensity deceased by 4%–5% in the time scale of ∼200 ps, consistent with previously reported lattice dynamics in CdTe single crystal with time-resolved X-ray diffraction. The probing depth of the CdTe crystal was about 0.68 μm in kinetic theory, which is mentioned in the following passage. Therefore, the photo-excitation has propagated into the CdTe crystal at a velocity of about 3400 m/s, which corresponds well to the longitudinal acoustic velocity in CdTe crystal (3440 m/s). [108] The exciting depth and probing for the CdTe crystal with laser and X-ray were calculated with the extinction coefficient and mass attenuation factor.

The laser intensity, I_l, after passing a distance x in a medium is equal to:

$$I_l = I_{l0} \exp(-\alpha x) \tag{4.45}$$

where I_{l0} is the intensity at $x = 0$ and α is called the absorption coefficient. The $1/e$ penetrating depth can be defined as $1/\alpha$ from Eq. (4.45). For many applications, the extension coefficient, k, defined as

$$\begin{aligned} k &= \alpha \frac{\lambda}{4\pi} \\ \frac{1}{\alpha} &= \frac{\lambda}{4\pi k} \end{aligned} \tag{4.46}$$

(where λ is the wavelength of the laser), is more commonly used for characterization of the electromagnetic loss in materials. The refractive index $(n - ik)$ of the CdTe is $2.877 - 0.065i$ at a wavelength of 800 nm [109]; therefore, the $1/e$ penetrating depth of the infrared light is calculated to be about 0.9 μm with the incident angle of 45°. The mass attenuation coefficient of CdTe is 2.4×10^2 cm^2/g and the linear absorption coefficient (μ_0) is 1.42×10^3 cm^{-1} for 8 keV X-ray. Therefore, the $1/e$ penetrating depth of CdTe is 0.68 μm with an X-ray incident angle of 11.88° in the kinetic

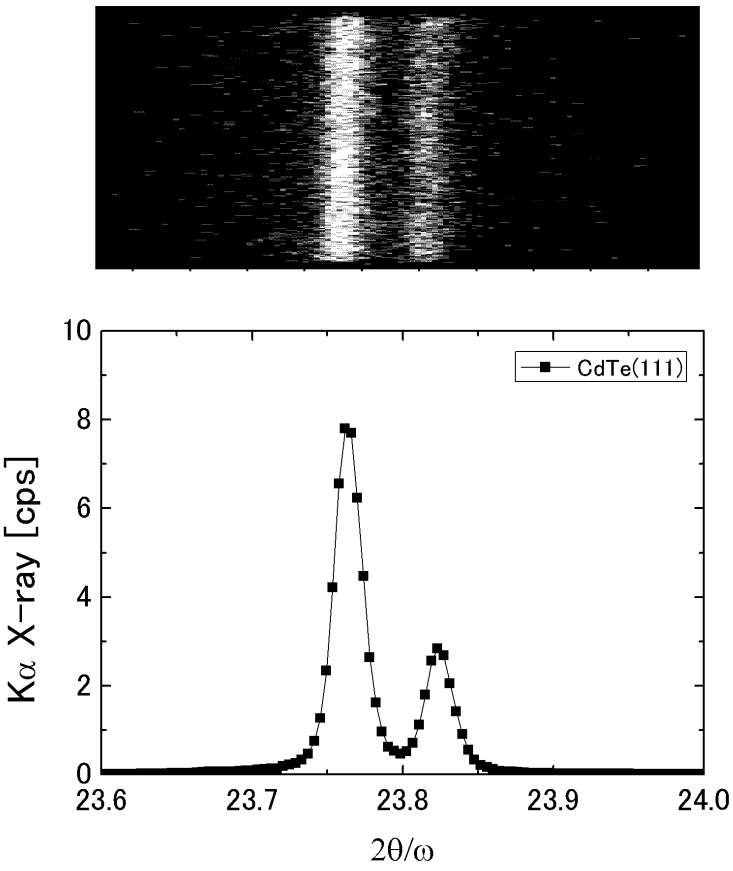

Figure 4.11: Typical X-ray diffraction lines from (111) CdTe

theory of X-ray diffraction.[109] In the dynamical theory, the penetrating depth of X-ray (μ) can be modified as the following equation:[100]

$$\mu = \mu_0 \sqrt{1 - T_j \cos^2 \Phi}, \tag{4.47}$$

where, Φ is the phase angle of the structure factor, and the phase angle of structure factor of CdTe is expressed as,

$$\Phi = \tan^{-1} \frac{\Sigma_j f_j(\vec{K}) \sin 2\pi(u\vec{a} + v\vec{b} + w\vec{c})}{\Sigma_j f_j(\vec{K}) \cos 2\pi(u\vec{a} + v\vec{b} + w\vec{c})}. \tag{4.48}$$

The penetrating depth of CdTe in the dynamical theory is 0.94 μm with an

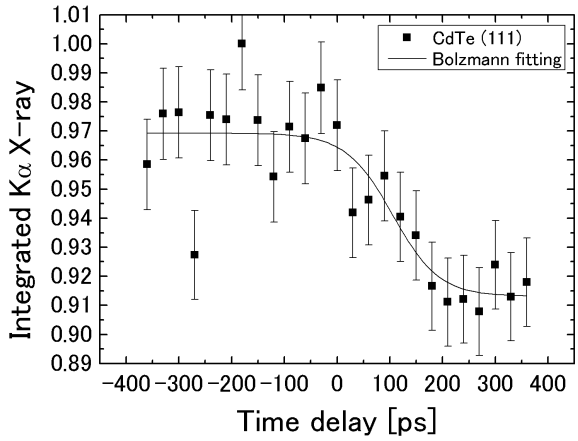

Figure 4.12: The changes in integrated intensity of the diffraction lines as a function of the time delay (The inserted fitting curve is guide for the eye).

X-ray incident angle of 11.88°, which is close to the value from the kinetic theory.

In the thermal process, the change in diffraction line is attributed to the Debye–Waller effect. As mentioned in section 4.1, the intensity of diffraction lines (I) at temperature T is

$$\begin{aligned} I(T) &= I(0)\exp\left[-2\cdot 2\pi^2 K^2 U_j(T)\right] \\ &= I(T_R)\exp\left[-2\cdot 2\pi^2 K^2\left(U_j(T)-U_j(T_R)\right)\right] \end{aligned} \tag{4.49}$$

where T_R is room temperature. The displacement parameter at the temperature T was estimated assuming the thermal vibration as the isotropic harmonic oscillator. The energy of vibration (E) in a crystal at a given temperature (T) can be described with the Maxwell–Boltzmann distribution as:

$$f_{MB}(E) = e^{-E/k_B T}. \tag{4.50}$$

Therefore, the distribution (x) of atomic vibration in the crystal can be described with the following Gaussian distribution

$$f_{MB}(x) = \exp\left(-\frac{kx^2}{2k_B T}\right) \tag{4.51}$$

where k is the force constant in an elastic body and is estimated with linear compressibility (B) and atomic distance (a_0) as

$$k = \frac{a_0}{B}. \tag{4.52}$$

The standard deviation of the distribution corresponds to the displacement by the thermal vibration

$$U(T) \sim \frac{k_B T}{k} \tag{4.53}$$

The linear compressibility (B) and atomic distance (a_0) of CdTe is 7.41 $\times$ 10^{-12} Pa^{-1} and 2.81 Å, respectively. [110] Thus, thermal displacement at T = 293 K (room temperature) was calculated to be ∼0.103 Å. The intensity loss of 4%–5% corresponded to an isotropic thermal displacement of ∼0.165 Åat a temperature of about 700 K. The CdTe crystal would be oxidized and significantly damaged when heated repeatedly to about 700 K in air. However, after the multiple excitations, the CdTe crystal presented no degradation on the surface. [111, 112] Moreover, the optical pulse at an intensity of ∼3 mJ/cm^2 induced a temperature increase in the CdTe crystal of 100 K at most. When the thermal vibration mode along to the [111] direction was selectively excited with optical pulses, the thermal displacement caused by the temperature increase of about 100 K was enhanced to be about 0.147 Åin the [111] direction, which in the CdTe crystal corresponds to the longitudinal direction of thermal propagation. On the picosecond timescale, a longitudinal optical (LO) phonon will be excited selectively and an LO phonon will be coupled with a longitudinal acoustic (LA) phonon and expand the thermal effect into the depth area of the crystal. [113, 114] The intensity loss with the anisotropic thermal displacement was calculated to be ∼3% and agreed well with the relative magnitudes of the experimental results. Thus, an anisotropic thermal vibration would have occurred in the CdTe crystal in the picosecond timescale and the thermal effect would propagate into the depth area of the crystal with acoustic velocity.

4.4 Ultrafast phase transition of VO_2 thin film

Vanadium dioxide (VO_2) is a representative material for the metal-insulator phase transition and exhibits the transition at a temperature of ∼340 K. Several papers on optical [115, 116, 117], THz [118, 119] and soft X-ray [120] spectroscopic pump–probe measurements of the phase transition in VO_2 have been reported, and a few reports on time-resolved crystallography reveled

the intriguing nature of the structural dynamics of the phase transition in VO_2.[121, 122] Phase transition was observed for a bulk sample by the intensity changes of X-ray diffraction lines from around the (011) plane and for thin film sample by intensity changes of several electron diffraction spots. In this study, we performed time-resolved X-ray diffraction measurements of the photo-induced phase transition in epitaxial VO_2 thin film on c-Al_2O_3. The analysis was based on complicated X-ray diffraction data separated into the parts of motion in the VO_2 film, lattice unit cells and atoms in the unit cell enabled us to directly observe not only the phase transition of the unit cell but also the displacement of atoms in the unit cell in the picosecond time scale. A series of direct structural observations shows the intermediate states of phase transition materials and in the future will be able to reveal the nature of photo-induced nonequilibrium processes.

4.4.1 Lattice parameters and atomic coordinates of epitaxial VO_2 thin film

A highly (010) oriented VO_2 film (280 nm thickness) was epitaxially grown on a c-Al_2O_3 (0001) substrate at a temperature of 673 K.[123, 124] Static out-of-plane and in-plane X-ray diffraction measurements were performed at a temperature of 293 K (low-temperature phase) and 343 K (high-temperature phase). The monoclinic and tetragonal VO_2 structures reside in the space group of $P2_1/C$ (No. 14)[125] and $P4_2/mnm$ (No. 136)[126], respectively. Figure 4.13 shows the lattice parameters and atomic coordinates estimated from the static X-ray diffraction lines of (020), (040), (200), (022) and (40-2). The lattice parameters were calculated from the Bragg equation and the Bragg angle of the static X-ray diffraction results. The atomic coordinates in the unit cell were calculated based on reference[127], using the relative integral intensity of each diffraction line and computer simulation using CrystalMaker 8.2.[128] The details of the calculation are shown in the following section. These lattice parameters were slightly different (0.1%–0.6% with each axis) from those of the powder VO_2, because of the effect of tension from the substrate.[125, 126, 127]

The static X-ray diffraction measurements also indicated the VO_2 structural changes before and after the transition. As shown in Eq. (4.26), the intensity of the diffraction line (I) can be defined as:

$$I = G(\vec{K})^2 F(\vec{K})^2, \tag{4.54}$$

$$G(\vec{K}) = \sum_{u,v,w} \exp[2\pi i \vec{K} \cdot (u\vec{a} + v\vec{b} + w\vec{c})], \tag{4.55}$$

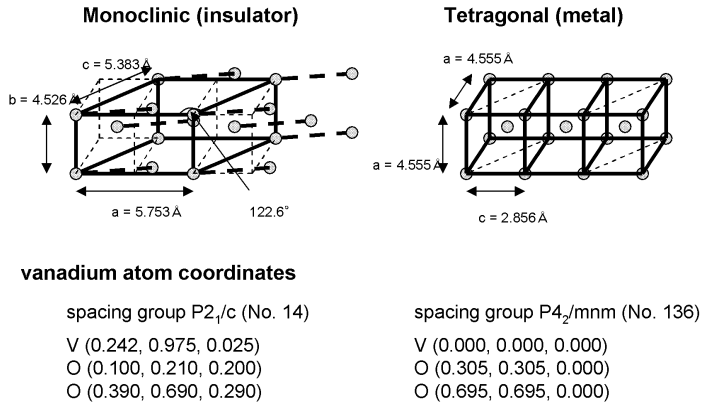

Figure 4.13: The lattice parameters and positions of vanadium atoms in the unit cell of the epixially grown VO_2 thin film.

$$F(\vec{K}) = \sum_{j=1} f_j(\vec{K}) T_j(\vec{K} \exp[2\pi i \vec{K} \cdot \vec{r_j}], \tag{4.56}$$

where $\vec{K}$, $G(\vec{K})$, $F(\vec{K})$, $f_j(\vec{K})$, and $T_j(\vec{K})$ are wave vector, Laue function, crystal structure factor, atomic scattering factor and temperature factor, respectively.The atomic position in the unit cell is represented as $\vec{r_j}$. The Bragg angle of the diffraction line depends on the Laue function (Eq. (4.55)), more specifically the size of the unit cell. In contrast, the intensity of the diffraction line depends strongly on the crystal structure factor (Eq. (4.56)). The difference in the atomic scattering and temperature factors before and after the transition is negligible; therefore, the intensity of the diffraction line will mainly depend on the position of atoms in the unit cell. Figure 4.14 shows the Cu Kα X-ray diffraction lines from the VO_2 (020) plane at low temperatures and high temperatures (2θ : 39.86° and 39.77°, respectively). The changes in Bragg angle and intensity were relatively large in the diffraction lines from the (020) plane among the observed diffraction lines. In Fig. 4.14, the diffraction lines shifted 0.09° toward the lower angle in the high-temperature phase as a result of the "swelling" of the unit cells, which was estimated to be 1.0 pm on the y-axis. The integral intensity of the diffraction lines increased ∼2.2 times in the high-temperature phase mostly as a result of the improvement in the symmetry of the atomic position in the unit cell. The change in atomic positions can be estimated from the atomic coordinates, as shown in Fig. 4.13. There are four vanadium atoms in a

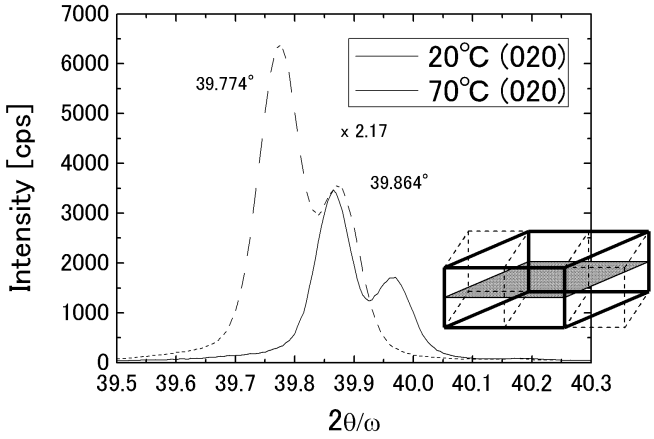

Figure 4.14: The spectra of the static out-of-plane X-ray diffraction lines from the (020) plane of the VO_2 sample at 293 K (monoclinic phase) and 343 K (tetragonal phase).

unit cell; V1 around the corner of the unit cell and V2 nearby the center of (011) the plane moved ∼16.3 pm along the y-direction in an opposite way, and V3 and V4 changed the positions by moving a distance of ∼42.4 pm, which agreed well with the order of the results in the references [127]; the moving distance of V1 and V2 was ∼10 pm and that of V3 and V4 was ∼22 pm. The atomic pairs of V1–V3 and V2–V4 in the monoclinic phase had the twist movements.

Calculation of atomic coordinates

The atomic coordinates in the unit cell of a sample in powder form can be generally determined by comparing the relative intensity of the X-ray diffraction lines from several different lattice planes. However, when the sample is an epitaxial thin film, the X-ray diffraction lines can be obtained only from a few lattice planes. Moreover, the diffraction condition of one lattice plane in an epitaxial thin film is very different from that of another lattice plane; therefore, it is impossible or hard to compare the relative intensity of the X-ray diffraction lines from the different lattice planes. The atomic coordinates in the unit cells of the VO_2 thin film before and after the

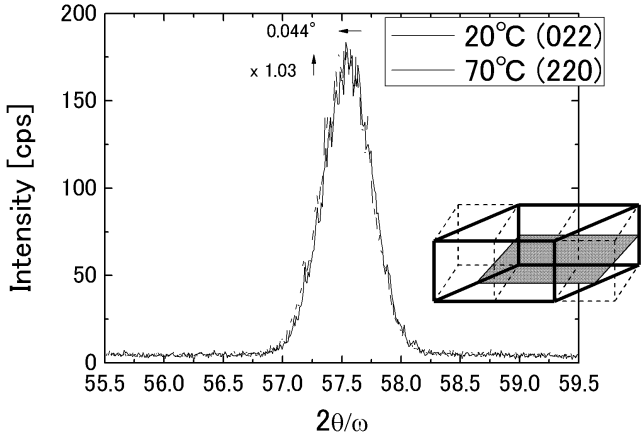

Figure 4.15: The spectra of the static out-of-plane X-ray diffraction lines from the (022) plane of the VO_2 sample at 293 K (monoclinic phase) and 343 K (tetragonal phase).

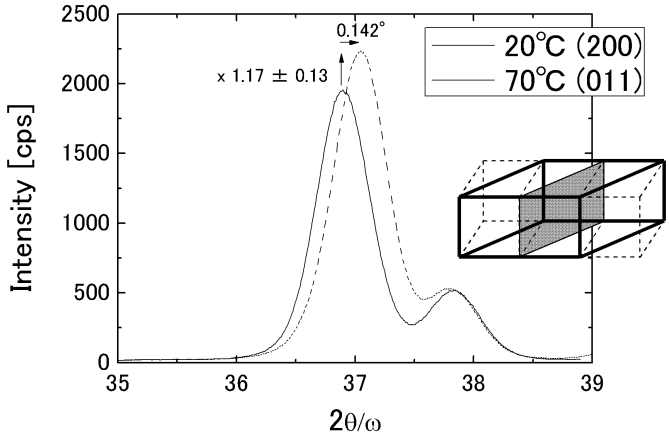

Figure 4.16: The spectra of the static out-of-plane X-ray diffraction lines from the (200) plane of the VO_2 sample at 293 K (monoclinic phase) and 343 K (tetragonal phase).

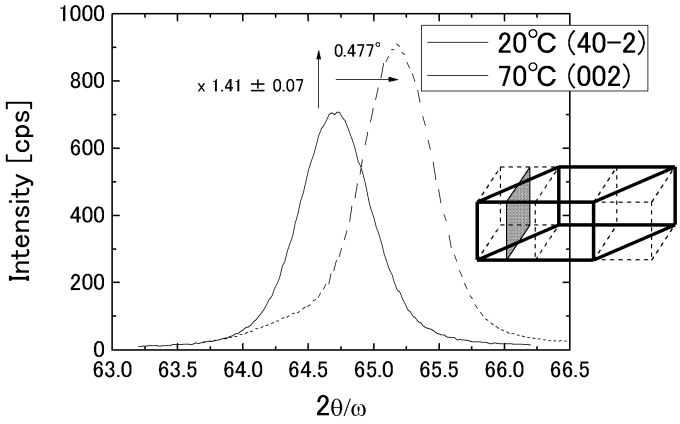

Figure 4.17: The spectra of the static out-of-plane X-ray diffraction lines from the (40-2) plane of the VO_2 sample at 293 K (monoclinic phase) and 343 K (tetragonal phase).

transition also cannot be determined simultaneously only with the diffraction lines from (020), (040), (200), (022) and (40-2) planes before and after the transition. However, it is possible to determine the coordinates of the vanadium atom in the unit cell of either phase. Therefore, in order to stimate the coordinates of the vanadium atom in the unit cell of VO_2 thin film in the low temperature phase VO_2 thin film, we made some assumptions, as follows.

1. The space group of the VO_2 at low temperature would reside in $P2_1/C$, and that at high temperature in $P4_2/mnm$.

2. The coordinates of vanadium atom and oxygen atoms in the unit cell of the VO_2 at high temperature would be the theoretical values: V (0.000, 0.000 ,0.000) O1 (0.305, 0.305, 0.000) O2 (0.695, 0.695, 0.000).

3. The coordinates of oxygen atoms in the unit cell of the VO_2 at low temperature would be the theoretical values: O1 (0.106, 0.212, 0.209) and O2 (0.401, 0.703, 0.299).

Assumption 1 would be valid because the space group of the material does not change with the form of the sample (powder or epitaxially grown film).

	simulate	experimental
(020)	x 2.20	x 2.17
(022)	x 1.07	x 1.03
(200)	x 1.16	x 1.17
(40−2)	x 1.62	x 1.41

Figure 4.18: Comparison of the changes in diffraction intensity obtained from experiment and the simulated.

Assumption 2 means that the atomic coordinates in the unit cell would be more distorted in low temperature phase than in the high temperature phase. This is because the symmetry of atomic coordinates of VO_2 in the low temperature phase is worse than in high temperature phase. In assumption 3, X-ray scattering from vanadium atoms is more than 8 times stronger than that from oxygen atoms; therefore the effect of the oxygen in the intensity of the X-ray diffraction lines can be negligible.

The coordinates of the vanadium atom in the unit cell of $P2_1/C$ are (0.239, 0.979, 0.027) and it should be modified with the experimental results. Figures 4.14 – 4.17 show the X-ray diffraction lines from the (020), (200), (022) and (40-2) planes before and after the transition. The "y" value of the atomic coordinates was determined to compare the changes in the intensity of the (020) X-ray diffraction lines before and after the transition obtained from the experiment and from the simulation using CrystalMaker 8.2. In a similar way, the "x" and "z" values were determined using the diffraction lines from the (200) and (022) planes, respectively. Thus, the coordinates of the vanadium atom were determined to be (0.216, 0.962, 0.000). The diffraction lines from (40-2) was used to revalidate the assumptions. Fig. 4.18 shows the comparison of the changes in diffraction intensity obtained from the experiment and the simulation. As shown in Fig. 4.18, the changes were corresponded well; therefore the assumption and the estimation of the atomic coordinates were considered valid.

4.4.2 Phase transition of VO_2 thin film

Time-resolved X-ray diffraction measurements were performed in air using a laser-plasma-induced X-ray source of Cu Kα_1 and Kα_2 radiation at 1 kHz,

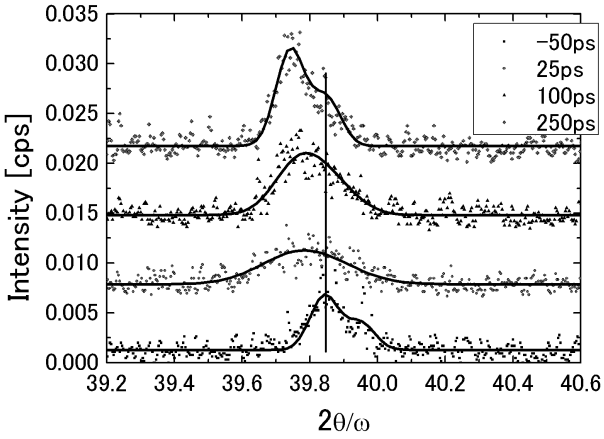

Figure 4.19: The typical spectra of the time-resolved X-ray diffraction lines from tne (020) plane of the VO_2 sample; the vertical line shows the Bragg angle of VO_2 for negative time delay. The solid lines are fitting curves of the double Gaussian, where the Kα_1 and Kα_2 X-ray diffraction lines are represented.

generated by focusing a millijoule femtosecond laser onto a rotating copper target in helium ambient. The measurements were collected with a compactly designed X-ray diffraction system with a tabletop femtosecond laser. The probing X-ray radiation emitted over a range of 2π steradians was collimated using slits with 0.3 mm width and 1 mm height, and was focused on the VO_2 sample at an incident angle of 19.91° to detect diffraction lines from the (020) plane. The pulse width of the pulsed X-ray was estimated to be about 200 fs and the time-resolution was about 1 ps, determined by considering the geometry of the X-ray divergence angle. The diffracted X-ray was detected using a charge coupled device camera. The VO_2 sample was mounted on a thermal heater, the temperature of which was controlled at 316 K. The sample was photo-excited using an 800-nm-wavelength femtosecond optical pulse. The area excited by the optical pulse had a 1.7 mm diameter and was larger than the X-ray-probed area. The intensity of the pumping pulse was 8.7 mJ/cm^2, higher than the phase transition threshold (6–7 mJ/cm^2) [121, 122] and much lower than the single-shot damage threshold (63 mJ/cm^2) [121].

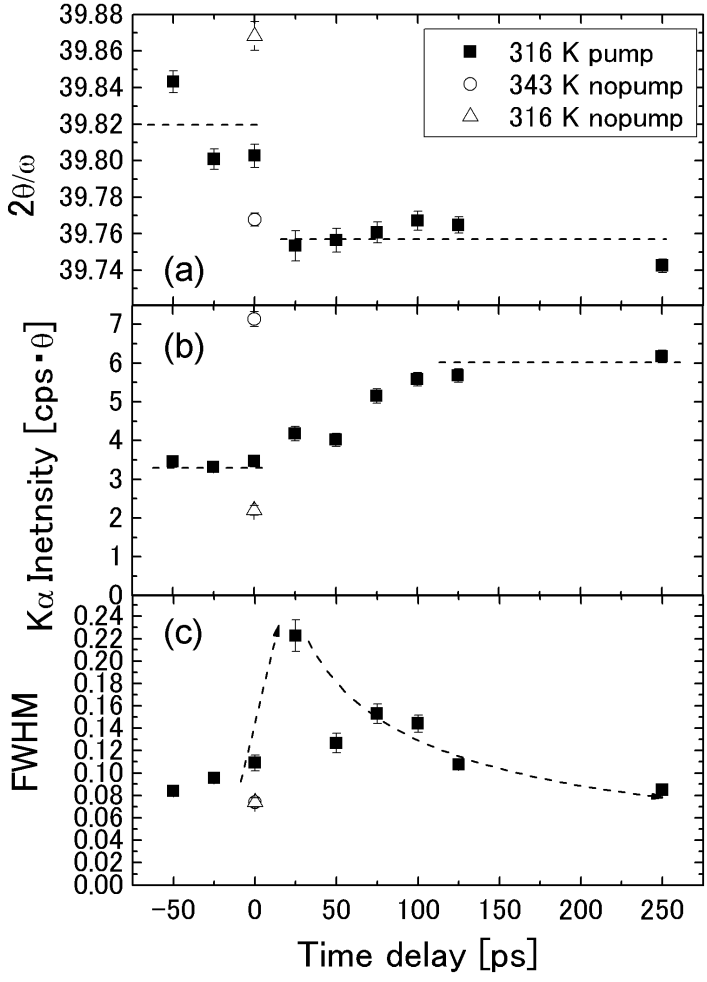

Figure 4.20: The changes in Bragg angle (a), integral intensity (b) and FWHM (c) of the (020) X-ray diffraction lines. The dotted lines are guides to the eye.

The typical X-ray diffraction spectra at time delays of –50, 25, 100 and 250 ps are shown in Fig. 4.19. As shown in the figure, the Bragg angle of the diffraction lines was higher for negative delay time, and shifted toward a markedly lower angle at 250 ps. The integral intensity of the diffraction lines has doubled through the transition. These changes corresponded well to those observed in static X-ray diffraction measurements. The time-resolved measurements enabled us to obtain information on the disequilibrium state of VO_2, i.e., the diffraction lines at 25 ps. Figure 4.20 (a, b, c), which was derived from Fig. 4.19, shows the changes in Bragg angle, integral intensity and FWHM of the diffraction lines as a function of delay time. The Bragg angle of the diffraction lines shifted toward a lower angle within 25 ps and on the other hand, the integrated intensity gradually increased up to ∼100 ps (Figs. 4.20 (a, b)). The FWHM of the diffraction lines increased by a factor of 2–3 in the first 25 ps then gradually decreased during the following ∼100 ps (Fig. 4.20 (c)). This change in the Bragg angle suggests that the VO_2 monoclinic unit cell transformed into a tetragonal unit cell extremely rapidly (within 25 ps). To analyze the changes in the intensity and the FWHM of the diffraction lines, the fluctuation in film depth should be considered because the penetration depth of the optical pulse at a wavelength of 800 nm was shallower than the film thickness. The complex refractive index of VO_2 in the insulator phase was $2.9 - 0.385i$ (the wavelength: 800 nm) [128]; therefore, the $1/e$ penetration depth of the optical pulse was calculated to be 163 nm at an incident angle of 30°. Regarding the fluctuation in film depth, we made the simple assumption that the upper half of the film was excited and underwent a transition to the tetragonal phase, whereas the lower half remained in the monoclinic phase in the transition state. The photo-excited layer propagated to the deeper part of the film at the acoustic velocity of ∼100 nm per ∼100 ps, which was consistent with previously reported results [121, 122, 129]. With this assumption, the diffraction line in the transition state should be a combination of diffraction lines from the monoclinic and tetragonal phases in the ultrafast time scale. The increase in the FWHM value of the diffraction lines may have been induced with the propagation of photo-excited layer. However, the peak intensity of the diffraction lines from the tetragonal phase in the upper half of the film and the monoclinic phase in the lower half should be higher than those from the monoclinic phase and lower than those from the tetragonal phase. Therefore, the reduction in peak intensity of the diffraction lines shown in Fig. 4.19 (at 25 ps) cannot be explained only by this photo-excited layer propagation. Changes in the Bragg angle occurred on the ultrafast time scale (<10 ps) also in the X-ray diffraction measurements performed by Cavalleri *et al.* [121],

and the corresponding changes of Bragg angle corresponded well to our results. However, it was difficult to discuss the atomic motion, which can be estimated from the change in intensity, because the film in the reference [121] was much thicker ($\sim$2 μm) than the $1/e$ penetration depth.

The increase in the FWHM of the diffraction lines may have be attributed to the fluctuation of the unit cells. The superposition of unit cells of different sizes can also produce diffraction lines with an increased FWHM according to Eq. (4.55). This fluctuation between unit cells was driven by the relatively long ($\sim$10 pm) atom displacements in the unit cell in a short time (less than 25 ps). If the fluctuation in the unit cell was driven by the displaced atoms, which caused the increase in the FWHM of the diffraction lines, the intensity of the diffraction lines should have be decreased simultaneously, because the atomic fluctuation reduces the intensity of the diffraction lines according to Eq. (4.56). The peak intensity of the diffraction lines at 25 ps was reduced by about half, as shown in Fig. 4.19. The fluctuations of the unit cell and the atoms in it are thought to gradually abate by thermal coupling within $\sim$100 ps, which should lead to a decrease in the FWHM of the diffraction lines and an increase in their peak intensity. The fluctuation or vibration might be of similar nature to that observed in spectroscopic methods. The transition state would be a very complex state involving phase transition, photo-excited layer propagation and fluctuation or vibration. Cavalleri *et al*, [121] and Baum *et al*. [122] showed that the phase transition in VO_2 mainly occurs within $\sim$12 ps and by less than 500 fs respectively, consistent with the phase transition time scale of less than 25 ps. The thermal coupling time scale of $\sim$100 ps also corresponds well to the previously reported time scale of shear motion. Here, it is worth mentioning that in this study the Bragg angle, intensity and FWHM of the diffraction lines from the (020) plane of the VO_2 thin film were measured by stimulatory time-resolved X-ray diffraction, which revealed the fluctuation or vibration of the VO_2 lattice and the atoms in the unit cell. The time-resolved electron diffraction measurements revealed a change in the intensity of several diffraction spots with a very high time resolution; however, the displacement of the VO_2 unit cell was $\sim$1.0 pm, therefore the change in the diffraction angle could be calculated to be $\sim$0.03°. The change in Bragg angle of $\sim$0.03° corresponded to $\sim$180 μm on the multichannel plate at the camera length of 300 mm, which is difficult to resolve with electron diffraction measurements because the electron beam size was $\sim$200 μm. [130]

4.5 Summary

In this chapter, we reported on time-resolved X-ray diffraction measurements for CdTe single crystal and VO_2 thin film performed in air using a tabletop laser-plasma-induced X-ray source. The following are summarizing remarks or this chapter.

1. The integrated intensity of Kα X-ray diffraction lines from the (111) CdTe decreased by 4%–5% in the timescale of $\sim$200 ps. The intensity decrease was consistent with anisotropically excited thermal vibrations calculated with the Debye–Waller factor, and the propagation time agreed well with the acoustic velocity in the CdTe crystal.

2. The transition state in the VO_2 has so far been observed only in the spectroscopic methods, but we could observe it using more direct X-ray diffraction measurement and analyzing changes in intensity and FWHM of the diffraction lines. The photo-excited monoclinic VO_2 was transformed into a tetragonal structure rapidly, but the atoms in the unit cell and the unit cell itself fluctuated or vibrated around the center of the tetragonal coordinates. The atomic fluctuation was coupled with an isotropic thermal phonon and abated in $\sim$100 ps. The propagation of the photo-excited layer would be a competitive process in this time scale.

3. The tabletop time-resolved X-ray diffraction system could be a promising tool for laboratory-based molecular dynamic studies on materials, chemical and biological systems.

Chapter 5

Conclusions and Future Studies

5.1 Summary and conclusions

The first molecular movements in a chemical processes are invoked in the time-scale of femtoseconds to picoseconds, and it is extremely important to observe directly molecular dynamics because the chemical processes are determined by the molecular motions on this time-scale. Different kinds of spectroscopic and crystallographic methods have been tried so far to visualize the molecular dynamics in real time and space, and recent time-resolved X-ray and electron diffraction measurements have made this possible. In this work, we have presented the ultrafast molecular dynamics in solid materials directly using time-resolved X-ray diffraction measurements with a tabletop femtosecond laser.

The theoretical description of the femtosecond laser was discussed in the first part of this thesis and a description of conventional experimental optical pump–probe measurements was also given. The most basic pump–probe experiment is to measure the pulse duration of the femtosecond laser using the autocorrelation method. The duration of the optical pulses emitted from the femtosecond laser was measured to be about 130 fs using the autocorrelation method with a BBO crystal.

A repeatable spectroscopic pump–probe measurement was performed on a thin bismuth film. The A_{1g} mode phonon at frequency of 2.9 $\pm$ 0.1 THz was observed from the modulation of the reflectivity. The laser-induced phase transition in single crystal silicon was studied by means of single-shot spectroscopic pump–probe measurements. Nonthermal and thermal phase transformations of the silicon crystal to metal-like liquid were observed. In the single-shot or unrepeatable pump–probe measurements, each event is unique, it occurs only once; therefore, a change the sample position it is required in order to get a fresh surface for each shot of the laser pulse. A

large and uniform sample is required for this method in order to have a different useful sample position available for each measurement.

One of the most important topics in this thesis is the ultrafast pulsed X-ray generated with laser-produced plasma using a tabletop commercial femtosecond laser in helium at atmospheric pressure. Generally, ultrafast X-ray radiation with intensity of more than 1×10^8 cps/sr is required for time-resolved X-ray diffraction measurements. In this work, the intensity of the Cu Kα X-ray in helium ambient was 5.4×10^9 cps/sr with 1 kHz repetition rate and conversion efficiency of 5.0×10^{-6}. This X-ray intensity is close to that obtained in vacuum conditions and is high enough for the time-resolved X-ray diffraction or other X-ray applications.

Theoretical studies on the X-ray radiation from laser-produced-plasma in vacuum have been conducted with computer simulation; however, there was no interpretation about the relationship between the Kα X-ray conversion efficiency and the ambient atmosphere near the target surface. We constructed a simple model to explain the relationship with the normalized Kα X-ray conversion efficiency in various conditions. This model suggested that the electron mean free path in the specific atmosphere and pressure is an important parameter in the generation of the ultrafast pulsed X-ray and about 20%–40% of the intensity of ultrafast pulsed Kα X-ray in vacuum was obtained even at atmospheric pressure in helium ambient.

Time-resolved X-ray diffraction measurements were performed for CdTe single crystal and VO_2 thin film using the tabletop laser-produced plasma X-ray source. We reported the first time-resolved X-ray diffraction measurements with a tabletop and in-air X-ray diffractometer. CdTe is one of the most suitable materials for time-resolved X-ray diffraction because the penetration depths of infrared light and hard X-ray are almost the same ($\sim$1 μm). The change in intensity of the X-ray diffraction lines indicated the presence of anisotropically excited thermal vibrations in CdTe, and the propagation time was well consistent with the acoustic velocity in the CdTe crystal. The transition state in the photo-excited VO_2 has been observed until now only with the spectroscopic methods; however in this work, it was observed using more direct X-ray diffraction measurements of the changes in the intensity, peak position and FWHM of the diffraction lines. The photo-excited monoclinic VO_2 was rapidly transformed into a tetragonal structure; however, the atoms in the unit cell fluctuated or vibrated around the center of the tetragonal coordinates. The atomic fluctuation was coupled with an isotropic thermal phonon and abated in $\sim$100 ps. It also implies a potential softening in the transition state. The tabletop time-resolved X-ray diffraction system would be a promising tool for laboratory-based reproducible

molecular dynamic studies on materials, chemical and biological systems.

5.2 Future studies

The tabletop time-resolved X-ray diffraction measurements have successfully revealed the nature of the molecular dynamics in real time and real space. However, there remain a handful of problems with this tabletop or laboratory-top X-ray system; only repeatable phenomena or phenomena in well-crystallized samples could be observed with this series of experiments, but there are much more unrepeatable chemical processes and phenomena than repeatable phenomena. In other words, the repeatable phenomena or well-crystallized materials are a rare case. It is a more exciting and important challenge to observe the molecular motion in such the nonrepeatable phenomena. Further attempts to overcome these problems have been performed with two different ultrafast time-resolved crystallographic methods; ultrafast X-ray diffraction with X-ray free electron laser and next generation ultrafast electron diffraction. In this section, the next generation ultrafast time-resolved crystallography is introduced.

5.2.1 X-ray free electron laser

One big stream for the next generation ultrafast time-resolved crystallography is X-ray free electron laser (XFEL). [131, 132] The distinction of XFEL is the high-brightness (higher than 10^{10} photon/pulse), high-coherence ($\sim$100% transverse, $\sim$1% longitudinal) and short-pulse (below 100 fs) with the repetition rate of $\sim$10 Hz. The XFEL facilities are constructed in the U.S. (Linac Coherent Light Source; Stanford Linear Accelerator Center) [133], Europe (The European X-ray Free-Electron Laser; Deutsches Elektronen-Synchrotron) [134] and Japan (X-ray Free Electron Laser; SPring-8) [135]. The first XFEL pulses are already available in the U.S. (since 2009), and the XFEL in Japan will start firing the X-ray pulses in 2011, and the European XFEL will start the operation in 2013–2014.

The XFEL consists of an electron source, accelerators, pulse compressors, and undulators as shown in Fig. 5.1 In the electron source, electrons are emitted from a photo-cathode (in the U.S. and Europe) or a thermo-ionic source (in Japan). The generated electrons are accelerated with microwave cavity (L-band, S-band, C-band or more higher X-band) accelerators and the pulse width is compressed using the electrical and chicane type compressors. Then, the high-energy ($\sim$10 GeV), high-peak-current ($\sim$1 kA) and ultrashort pulsed ($<$100 fs) electron bunches are passed through the

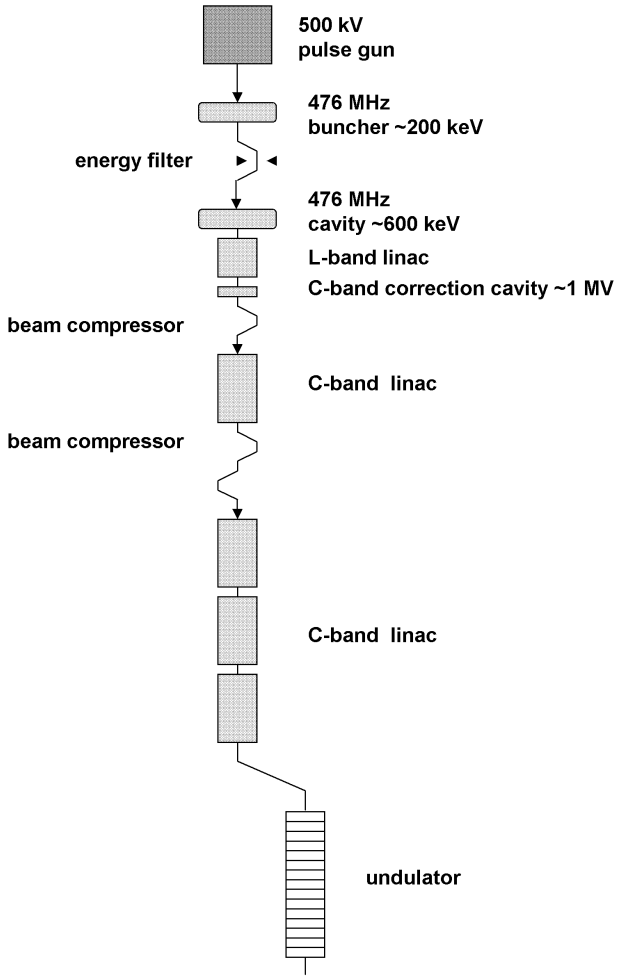

Figure 5.1: X-ray free electron laser.

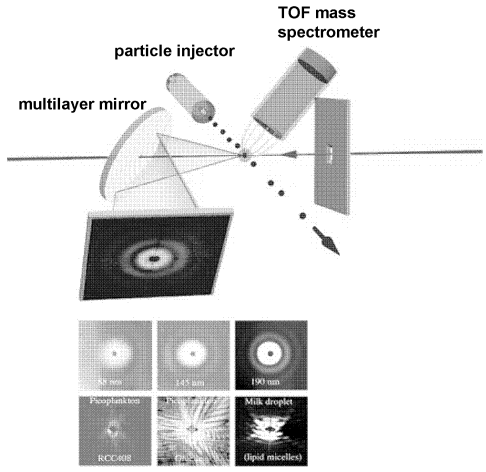

Figure 5.2: Single shot experiment with XFEL.

undulators and generate XFEL radiation. The XFEL radiation is achieved by the self amplification of spontaneous emission (SASE). The visible, infrared or ultraviolet free electron lasers are assembled with high reflectors on the side of the undulators; however, it is difficult to produce high-reflectors for hard X-ray. Instead of using high-reflectors, in XFEL long-aligned undulators are applied, and laser saturation is achieved with a single pass through the long aligned undulators. The generated X-ray pulses are introduced to the beamlines for user experiments. The XFEL in Japan is distinguished by its compactness with the utilization of C-band microwave cavities, and the European XFEL is distinguished by its repetition rate (1–100 kHz) with the use of the superconductor undulators.

A series of experiments that exploit the characteristics of XFEL, high brightness, high coherence and short pulse, are being proposed. One of the most representative and challenging examples is the single-shot observation of the ultrafast dynamics in a single, or nanocrystalline biomolecules. [136] Figure 5.2 shows the coherent X-ray diffraction experiment for the flying an isolated biomolecule in vacuum. These dream experiments will be demonstrated with the accomplishment of the XFEL, and should break new ground of the science.

5.2.2 Next generation ultrafast electron diffraction

Another completely different stream for the ultrafast time-resolved crystallography is ultrafast electron diffraction. [137] A comparison between the time-resolved X-ray diffraction and electron diffraction methods is shown in Fig. 5.3. The time-resolved electron diffraction assembled in a tabletop manner is also a powerful tool for direct atomic motion observation in condensed matter. As shown in the list in Fig. 5.3, the most important characteristic features of electron diffraction is the high interaction cross-section and shorter wavelength.

Electrons	**X-rays**
Strongly scattered (high interaction cross-section)	Weakly scattered (low interaction cross-section)
Tabletop experiment	Tabletop for plasma sources only. Synchrotron/XFEL/large frame laser
Pumped volume better matches scattering length of electrons	Large penetration depth, better suited for bulk studies
Multidiffraction orders facilitate structure determinations	Potential for Laue diffraction (not in the case of XFELs)
Pulse duration dependent on electron number (DC electron gun)	Pulse duration independent of photon number
Recompression to <100 fs with single shot structure capabilities and perfect synchronization of optical pump and electron probe	Estimated of 100 fs time resolution limited by timing jitter
Energy deposited in sample per scattering event 400-1000 times less (1.5A X-ray).Electron-induced sample damage is negligible	X-ray-induced damage limits crystal life time. Diffract and destroy
Incoherent (some possibility of cohrent electron)	Coherent (XFEL only)

Figure 5.3: Comparison of electrons and X-rays for applications.

Compared with X-ray, the scattering cross-section of electrons with the electrons surrounding atoms is more than 10^4 higher; therefore, fewer electrons are required to obtain an image of the diffraction pattern. About 10^6 electrons in a pulse are sufficient to demonstrate the single-shot time-resolved electron diffraction methods. Generally, extremely short electron pulses are generated by hitting the femtosecond optical pulses onto the photo-cathode. An electron bunch produced on the photo-cathode is accelerated with the static electric field and focused into a sample. While the bunch of electrons is traveling in vacuum, its pulse width broadens by Coulomb expansion. Therefore, the duration of electron pulse, acceleration energy, the number of electrons in the bunch, and the electron traveling

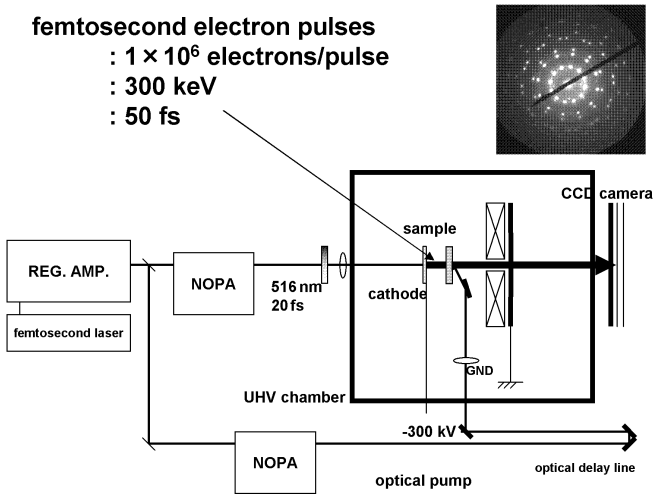

Figure 5.4: Next generation ultrafast electron diffraction measurements.

length in vacuum are strongly related to each other. The next generation ultrafast time-resolved electron diffraction system aims to obtain electron bunches with $\sim 10^6$ electrons at pulse duration of $\sim$50 fs, and acceleration energy of 300 keV for the single-shot measurements. Figure 5.4 shows the experimental setup for the next generation ultrafast time-resolved electron diffraction.

The De Broglie wavelength of an electron at $\sim$100 keV is $\sim$0.1 Åand much shorter than that of the copper characteristic X-rays ($\sim$1 Å). This feature makes it possible to obtain multi-diffraction spots at one time; however, it reduces the spatial resolution to about 1 Å(in X-ray diffraction it is less than 0.1 Å). The multi-diffraction spots allow us to trace the 3-dimentional molecular motion. In addition, the spin-polarized or coherent electrons can be easily produced by the contraption of the electron sources. These sources will show the different aspects of the nature of molecular motion. In the near future, experiments for molecular dynamics with X-ray and electron diffraction will revolutionize the scientific world.

References

[1] J.B. Perrin, The Nobel Prize in Physics 1926.

[2] J.D. Watson, F.H.C. Crick, Nature (London) **171** (1953) 737.

[3] F.H.C. Crick, J.D. Watson, M.H.F. Wilkins, The Nobel Prize in Physiology or Medicine 1962.

[4] N. F. Scherer, J. L. Knee, D. D. Smith, A. H. Zewail, J. Phys. Chem. **89** (1985) 5141.

[5] V. Engel, H. Metiu, R. Almeida, R. A. Marcus, A. H. Zewail, Chem. Phys. Lett. **152** (1988) 1.

[6] R. M. Bowman, M. Dantus, A. H. Zewail, Chem. Phys. Lett. **156** (1989) 131.

[7] A. Zewail, The Nobel Prize in Chemistry 1999.

[8] Z. Vardeny, J. Tauc, Opt. Comm. **39** (1981) 396.

[9] A.A. Bugaev, V.V. Gudyalis, B.P. Zakharchenya, F.A. Chudnovski, JETP Lett. **34** (1981) 430.

[10] C.V. Shank, R. Yen, C. Hirlimann, Phys. Rev. Lett. **50** (1983) 454.

[11] S. Desilvestri, J.G. Fujimoto, E.P. Ippen, E.B. Gamble Jr., L. R. Williams, K.A. Nelson, Chem. Phys. Lett. **116** (1985) 146.

[12] H.J.Zeiger, J.Vidal, T.K.Cheng, E.P.Ippen, G.Dresselhaus, M.S.Dresselhaus Phys. Rev. B **45** (1992) 768.

[13] T.K. Cheng, S,D. Brorson, A.S. Kazeroonian, J.S. Moodera, G. Dresselhaus, M.S. Dresselhaus, E.P. Ippen, Appl. Phys. Lett. **57** (1990) 10.

[14] B.C. Larson, J.Z. Tischler, J. Mater. Res. **1** (1986) 144.

[15] V. Srajer, T. Teng, T. Ursby, C. Pradervand, Z. Ren, S. Adachi, W. Schildkamp, D. Bourgeois, M. Wulff, K. Moffat, Science **274** (1996) 1726.

[16] R.W. Schoenlein, W.P. Leemans, A.H. Chin, P. Volfbeyn, T.E. Glover, P. Balling, M. Zolotorev, K.-J. Kim, S. Chattopadhyay, C.V. Shank, Science **274** (1996) 236.

[17] D.M. Fritz, D.A. Reis, B. Adams, R.A. Akre, J. Arthur, C. Blome, P.H. Bucksbaum, A.L. Cavalieri, S. Engemann, S. Fahy, R.W. Falcone, P.H. Fuoss, K.J. Gaffney, M.J. George, J. Hajdu, M.P. Hertlein, P.B. Hillyard, M.H. Hoegen, M. Kammler, J. Kaspar, R. Kienberger, P. Krejcik, S.H. Lee, A.M. Lindenberg, B. McFarland, D. Meyer, T. Montagne, E.D. Murray, A.J. Nelson, M. Nicoul, R. Pahl, J. Rudati, H. Schlarb, D.P. Siddons, K. Sokolowski-Tinten, Th. Tschentscher, D. von der Linde, J.B. Hastings, Science, **315** (2007) 633.

[18] M.M. Murnane, H.C. Kapteyn, M.D. Rosen, R.W. Falcone, Science, **251**. (1991) 531.

[19] C. Rischel, A. Rousse, I. Uschmann, P.-A. Albouy, J.-P. Geindre, P. Audebert, J.-C. Gauthier, E. Forster, J.-L. Martin, A. Antonetti, Nature (London) **390** (1996) 490.

[20] C. Rose-Petruck, R. Jimenez, T. Guo, A. Cavalleri, C.W. Siders, F. Raksi, J.A. Squier, B.C. Walker, K.R. Wilson, C.P.J. Barty, Nature (London) **398** (1999) 310.

[21] C.W. Siders, A. Cavalleri, K. Sokolowski-Tinten, Cs. Toth, T. Guo, M. Kammler, M.H. Hoegen, K.R. Wilson, D. von der Linde, C.P.J. Barty, Science **286** (1999) 1340.

[22] A.M. Lindenberg, I. Kang, S.L. Johnson, T. Missalla, P.A. Heimann, Z. Chang, J. Larsson, P.H. Bucksbaum, H.C. Kapteyn, H.A. Padmore, R.W. Lee, J.S. Wark, R.W. Falcone, Phys. Rev. Lett. **84** (2000) 111.

[23] A. Rousse, C. Rischel, S. Fourmaux, I. Uschmann, S. Sebban, G. Grillon, Ph. Balcou, E. Foerster, J.P. Geindre, P. Audebert, J.C. Gauthier, D. Hulin, Nature (London) **410** (2001) 65.

[24] K. Sokolowski-Tinten, C. Blome, J. Blums, A. Cavalleri, C. Dietrich, A. Tarasevitch, I. Uschmann, E. Forster, M. Kammler, M.H. Hoegen, D. von der Linde, Nature (London) **422** (2003) 287.

[25] M. Bargheer, N. Zhacoronkov, Y. Gritsai, J.C. Woo, D.S. Kim, M. Woerner, T. Elsaesser, Sicence **306** (2004) 1771.

[26] W.E. King, G.H. Campbell, A. Frank, B. Reed, J.F. Schmerge, B.J. Siwick, B.C. Stuart,P.M. Weber, J. Appl. Phys. **97** (2005) 111101.

[27] J.R. Dwyer, C.T. Hebeisen, R. Ernstorfer, M. Harb, V.B. Deyirmenjian, R.E. Jordan, R.J.D. Miller, Philos. Trans. R. Soc. A, **364** (2006) 741.

[28] M. Harb, R. Ernstorfer, T. Dartigalongue, C.T. Hebeisen, R.E. Jordan, R. J. Dwayne Miller, J. Phys. Chem. B **110** (2006) 25308.

[29] A.A. Ischenko, V.V. Golubkov, V.P. Spiridonov, A.V. Zgurskii, A.S. Akhmanov, M.G. Vabischevich, V. N. Bagratashvili, Appl. Phys. B **32** (1983) 161.

[30] R.C. Dudek, P.M. Weber, J. Phys. Chem. A **105** (2001) 4167.

[31] C. Rulliere (Ed): Femtosecond Laser Pulses, Springer, Berlin (1998).

[32] A.E. Siegman: Laser, University Science Books, Mill Valley, CA (1986), pp. 574-576.

[33] P.F. Curley, A.I. Ferguson, Opt. Lett. **16** (1991) 1016.

[34] N. Sarukura, Y. Ishida, T. Yanagawa, H. Nakano, Appl. Phys. Lett. **57** (1990) 229.

[35] G. Gabetta, D. Huang, J. Jacobson, M. Ramaswamy, E.P. Ippen, J.G. Fujimoto, Opt. Lett. **16** (1991) 1756.

[36] U. Keller, G.W. 'tHooft, W.H. Knox, J.E. Cunningham, Opt. Lett. **16** (1991) 1022.

[37] W.H. Lowdermilk In: M.L. Stitch (Ed), Laser handbook Vol. 3, North Holland Publishing Company, Amsterdam (1979), pp. 361–420.

[38] P. Lacovara, L. Esterowitz, and M. Kokta, IEEE J. Quant. Electron. QE **21** (1985) 1614.

[39] C.E. Byvik, A.M. Buoncristiani, IEEE J. Quant. Electron. QE **21** (1985) 1619.

[40] D.E. Spence, P.N. Kean, W. Sibbett, Opt. Lett. **16** (1991) 42.

[41] D.E. Spence, J.M. Evans, W.E. Sleat, W. Sibbett, Opt. Lett. **16** (1991) 1762.

[42] D. Strickland, G. Mourou, Opt.Comm. **56** (1985) 219.

[43] O.E. Martinez, IEEE J. Quantum Electron. QE **23** (1987) 59.

[44] See for example: User's Manuals of Tsunami (Spectra-Physics) and Spitfire Pro (Spectra-Physics).

[45] J.C. Diels, J.J. Fontaine, I.C. McMichael, F. Simoni, Appl. Opt. **24** (1985) 1270.

[46] J.C. Diels, J.J. Fontaine, W. Rudolph, Rev. Phys. Appl. **12** (1987) 1605.

[47] K. Naganuma, K. Mogi, H. Yamada, IEEE J. Quant. Electron. **25** (1989) 1225.

[48] J.S.Lannin, J.M. Calleja, M. Cardona, Phys. Rev. B **12** (1975) 585.

[49] M. Hase, K. Mizoguchi, H. Harima, S. Nakashima, K. Sakai, Phys. Rev. B **58** (1998) 5448.

[50] M. Hase, K. Ishioka, M. Kitajima, K. Ushida, S. Hishita Appl. Phys. Lett. **76** (2000) 1258.

[51] M. Hase, M. Kitajima, S. Nakashima, K. Mizoguchi, Phys. Rev. Lett. **88** (2002) 067401.

[52] K. Sokolowski-Tinten, J. Bialkowski, D. von der Linde, Phys. Rev. B **51** (1995) 14186.

[53] K.D. Li, P.M. Fauchet, Appl. Phys. Lett. **51** (1987) 1747.

[54] K. Sokolowski-Tinten, J. Bialkowski, M. Boing, Phys. Rev. B **58** (1998) 805.

[55] A.M. Lindenberg, J. Larsson, K. Sokolowski-Tinten, K.J. Gaffney, C. Blome, O. Synnergren, J. Sheppard, C. Caleman, A.G. MacPhee, D. Weinstein, D.P. Lowney, T.K. Allison, T. Matthews, R.W. Falcone, A.L. Cavalieri, D.M. Fritz, S.H. Lee, P.H. Bucksbaum, D.A. Reis, J. Rudati, P.H. Fuoss, C.C. Kao, D.P. Siddons, R. Pahl, J. Als-Nielsen, S. Duesterer, R. Ischebeck, H. Schlarb, H. Schulte-Schrepping, Th. Tschentscher, J. Schneider, D. von der Linde, O. Hignette, F. Sette, H.N. Chapman, R.W.

Lee, T.N. Hansen, S. Techert, J.S. Wark, M. Bergh, G. Huldt, D. van der Spoel, N. Timneanu, J. Hajdu, R.A. Akre, E. Bong, P. Krejcik, J. Arthur, S. Brennan, K. Luening, J.B. Hastings, Science **308** (2005) 392.

[56] P. Lucas, S. Webber (Eds): IEEE, Piscataway, NJ (2003) pp. 423-425.

[57] R. Service, Science **298** (2002) 1356.

[58] M. Yoshida, Y. Fujimoto, Y. Hironaka, K.G. Nakamura, K. Kondo,M. Ohtani, H. Tsunemi, Appl. Phys. Lett. **73** (1998) 2393.

[59] E.C. Eder, G. Pretzler, E. Fill, K. Eidmann, A. Saemann, Appl. Phys. B **70** (2000) 211.

[60] E. Fill, J. Bayerl, R. Tommasini, Rev. Sci. Instrum. **73** (2002) 2190.

[61] C.W. Siders, A. Cavalleri, K. Sokolowski-Tinten, T. Guo, C. Toth, R. Jimenez, C. Rose-Petruck, M. Kammler, M.H. von Hoegen, D. von der Linde, K.R. Wilson, C.P.J. Barty: SPIE Proc. **3776** (1999) 302.

[62] K. Sokolowski-Tinten1, D. von der Linde, J. Phys.: Condens. Matter **16** (2004) R1517.

[63] M. Hagedorn, J. Kutzner, G. Tsilimis, H. Zacharias, Appl. Phys. B **77** (2003) 49.

[64] C.G. Serbanescu, J.A. Chakera, and R. Fedosejevs, Rev. Sci. Instruments **78** (2007) 103502.

[65] C.L. Rettig, W.M. Roquemore, J.R. Gord, Appl. Phys. B **93** (2008) 365.

[66] Y. Jiang, T. Lee, W. Li, G. Ketwaroo, and C.G. Rose-Petruck, J. Opt. Soc. Am. B **20** (2003) 229.

[67] B. Hou, J. Easter, K. Krushelnick, and J.A. Nees, Appl. Phys. Lett. **92** (2008) 161501.

[68] B. Hou, J. Easter, A. Mordovanakis K. Krushelnick, and J.A. Nees, Opt. Express **16** (2008) 17695.

[69] R.M. More, Z. Zinamon, K.H. Warren, R. Falcone, M. Murnane, J. Phys. C **7** (1988) 43.

[70] E.G. Gamaly, Laser Part. Beams **12** (1994) 185.

[71] P. Gibbon, E. Forster, Plasma Phys. Control. Fusion **38** (1996) 769.

[72] R. Fedosejevs, R. Ottmann, R. Sigel, G. Kuhnle, S. Szatmari, F.P. Schafer, Phys. Rev. Lett. **64** (1990) 1250.

[73] D.F. Price, R.M. More, R.S.Walling, G. Guethlein, R.L. Shepherd, R.E. Stewart, W.E. White, Phys. Rev. Lett. **75** (1995) 252.

[74] D.W. Forslund, J.M. Kindel, K. Lee, Phys. Rev. Lett. **39** (1977) 284.

[75] K. Eidmann, J. Meyer-ter-Vehn, T. Schlegel, S. Huller, Phys. Rev. E **62** (2000) 1202.

[76] E.S. Weibel, Phys. Fluids **10** (1967) 741.

[77] S.C. Wilks, Phys. Fluids B **5** (1993) 2603.

[78] S.C. Wilks, W.L. Kruer, M. Tabak, A.B. Langdon, Phys. Rev. Lett. **69** (1992) 1383.

[79] W. Rozmus, V.T. Tikhonchuk, R. Cauble, Phys. Plasmas **3** (1996) 360.

[80] K.G. Nakamura, S. Ishii, S. Ishitsu, M. Shiokawa, H. Takahashi, K. Dharmalingam, J. Irisawa, Y. Hironaka, K. Ishioka, M. Kitajima, Appl. Phys. Lett. **93** (2008) 061905.

[81] Ch. Reich, P. Gibbon, I. Uschmann, and E. Forster, Phys. Rev. Lett. **84** (2000) 4846.

[82] M. Green and V. Cosslett, J. Phys. D **1** (1968) 425.

[83] Y. Hironaka, K.G. Nakamura, K. Kondo, Appl. Phys. Lett. **77** (2000) 4110.

[84] W.M.Wood, C.W. Siders, M.C. Downer, Phys Rev. Lett. **67** (1991) 3523.

[85] B.M. Penetrante, J.N. Bardsley, W.M. Wood, C.W. Siders, M.C. Downer, J. Opt. Soc. Am. B **9** (1992) 2032.

[86] F.V. Hartemann, A.L. Troha, H.A. Baldis, A. Gupta, A.K. Kerman, E.C. Landahl, N.C. Luhmann Jr., J.R. van Meter, Astrophys. J. Suppl. Ser. **127** (2000) 347.

[87] T. Auguste, P. Monot, L.A. Lompre, G. Mainfray, C. Manus, Opt. Commun. **89** (1992) 145.

[88] Y.M. Li, J.N. Broughton, R. Fedosejevs, T. Tomie, Opt. Commun. **93** (1992) 366.

[89] D. Umstadter, Appl. Phys. **36** (2003) R151.

[90] C.G. Serbanescu, J. Santiago, R. Fedosejevs, Proc. SPIE **5196** (2004) 344.

[91] M. Hada, J. Matsuo, Trans. Mater. Res. Soc. Jpn. **34** (2009) 621.

[92] M. Hada, J. Matsuo, Appl. Phys. B **99** (2010) 173.

[93] D. Kuhike, U. Herpers, D. von der Linde, Appl. Phys. Lett. **50** (1987) 1785.

[94] O.R. Wood, W.T. Silfvast, H.W.K. Tom, W.H. Knox, R.L. Fork, C.H. Brito-Cruz, M.C. Downer, P.J. Maloney, Appl Phys. Lett. **53** (1988) 654.

[95] H. Nakano, T. Nishikawa, H. Ahn, and N. Uesugi, Appl. Phys. Lett. **69** (1996) 2992.

[96] J. Kutzner, M. Sillies, T. Witting, G. Tsilimis, H. Zacharias, Appl. Phys. B **78** (2004) 949.

[97] W. Clegg (Ed): Crystal Structure Analysis, Oxford Science Publications, New York (2001).

[98] C. Kittel: Introduction to Solid State Physics, Wiley, New York (1986).

[99] T. Iida: [http://www.crl.nitech.ac.jp/ ida/education/index-j.html].

[100] S.-L. Chang: Multiple Diffraction of X-rays in Crystals, Springer-Verlag, Berlin (1984).

[101] E. Prince (Ed): International Tables for Crystallography Vol. C, Kluwer Academic Publisher, Dordrecht (1992).

[102] T. Feurer, A. Morak, I. Uschmann, Ch. Ziener, H. Schwoerer, Ch. Reich, P. Gibbon, E. Forster, R. Sauerbrey, Phys. Rev. E **65** (2001) 016412.

[103] J. Britt, C. Ferekides, Appl. Phys. Lett. **62** (1993) 2851.

[104] K. Jarasiunas, L. Bastiene, J.C. Launay, P. Delaye, G. Roosen, Semicond. Sci. Technol. **14** (1999) 48.

[105] P. Capper: Property of narrow gap cadmium-based compounds, INSPEC, London (1994).

[106] E.E. Koch, T. Sasaki, H. Winick (Eds): Handbook on Synchrotron Radiation, Vol. 1, North-Holland (1983).

[107] T. Namioka, K. Yamashita: X-ray Imaging Optics, Baifukan, Japan (1999).

[108] S.B. Kaplan, J. Low Temp. Phys. **37** (1979) 343.

[109] D.R. Lide (Ed): Handbook of Chemistry and Physics 84th Edition, CRC Press (2003).

[110] E. Deligoz, K. Colakoglu, Y. Ciftci, Physica B **373** (2006) 124.

[111] L.A. Golovan, P.K. Kashkarov, Yu.N. Sosnovskikh, V.Yu. Timoshenko, N.G. Chechenin, V.M. Lakeenkov, Phys. Solid State **40** (1998) 189.

[112] I. Visoly-Fisher, D. Dobson, J. Nair, E. Bezalel, G. Hodes, D. Cahen, Adv. Funct. Mater. **13** (2003) 289.

[113] R.G. Ulbrich, V. Narayanamurti, M.A. Chin, Phys. Rev. Lett. **27** (1980) 1432.

[114] A.H. Chin, R.W. Schoenlein, T.E. Glover, P. Balling, W.P. Leemans, C.V. Shank, Phys. Rev. Lett. **83** (1999) 336.

[115] M.F. Becker, A.B. Buckman, R.M. Walser, T. Lepine, P. Georges, A. Brun, Appl. Phys. Lett. **65** (1994) 1507.

[116] S. Lysenko, A.J. Rua, V. Vikhnin, J. Jimenez, F. Fernandez, H. Lu, Appl. Surf. Sci. **252** (2006) 5512.

[117] H.-T. Kim, Y.W. Lee, B.-J. Kim, B.-G. Chae, S.J. Yun, K.-Y. Kang, K.-J. Han, K.-J. Yee, Y.-S. Lim, Phys. Rev. Lett. **97** (2006) 266401.

[118] C. Kubler, H. Ehrke, R. Huber, R. Lopez, A. Halabica, R.F. Haglund Jr., A. Leitenstorfer, Phys. Rev. Lett. **99** (2007) 116401.

[119] M. Nakajima, N.Takubo, Z.Hiroi, Y.Ueda, T.Suemoto, J. Lumin. **129** (2009) 1802.

[120] A. Cavalleri, M. Rini, H.H.W. Chong, S. Fourmaux, T.E. Glover, P.A. Heimann, J.C. Kieffer, R.W. Schoenlein, Phys. Rev. Lett. **95** (2005) 067405.

[121] A. Cavalleri, Cs. Toth, C.W. Siders, J.A. Squier, F. Raksi, P. Forget, J.C. Kieffer, Phys. Rev. Lett. **87** (2001) 237401.

[122] P. Baum, D.-S. Yang, A.H. Zewail, Science **318** (2007) 788.

[123] K. Okimura, J. Sakai, Jpn. J. Appl. Phys. **48** (2009) 045504.

[124] K. Okimura, N. Ezreena, Y. Sasagawa, J. Sakai, Jpn. J. Appl. Phys. **48** (2009) 065003.

[125] G. Andersson, Acta Chem. Scand. **10** (1956) 623.

[126] S. Westman, Acta Chem. Scand. **15** (1961) 217.

[127] J.M. Longo, P. Kierkegaard, Acta Chem. Scand. **24** (1970) 420.

[128] CrystalMaker Software Limited, CrystalMaker 8.2 [http://www.crystalmaker.com/]

[129] M.S. Grinolds, V.A. Lobastov, J. Weissenrieder, A.H. Zewail, Proc. Natl. Acad. Sci. USA **103** (2006) 18427.

[130] N. Gedik, D.-S. Yang, G. Longvenov, I. Bozovic, A.H. Zewail, Science **316** (2007) 425.

[131] R. Bonifacio, C. Pellegrini, L.M. Narducci, Opt. Comm. **50** (1984) 373.

[132] E.E. Lattman, Proc. Natl. Acad. Sci. USA **98** (2001) 6535.

[133] J. Arthur (Ed): Linac Coherent Light Source (LCLS) Conceptual Design Report, SLAC-R593, Stanford, (2002).

[134] M. Altarelli (Ed): XFEL The European X-Ray Free-Electron Laser, Technical Design Report. Preprint DESY 2006-097, DESY Hamburg (2006).

[135] T. Tanaka, T. Shintake, (Eds): SCSS X-FEL Conceptual Design Report, RIKEN Harima Institute, Hyogo, Japan (2005).

[136] A. Barty, S. Boutet, M.J. Bogan, S. Hau-Riege, S. Marchesini, K. Sokolowski-Tinten, N. Stojanovic, R. Tobey, H. Ehrke, A. Cavalleri, S. Dusterer, M. Frank, S. Bajt, B.W. Woods, M.M. Seibert, J. Hajdu, R. Treusch, H.N. Chapman, Nature Photonics **2** (2008) 415.

[137] R.J. Dwayne Miller, R. Ernstorfer, M. Harb, M. Gao, C.T. Hebeisen, H. Jean-Ruel, C. Lu, G. Moriena, G. Sciaini, Acta Cryst. Sect. A **66** (2010) 137.

List of publications

Journal Papers

1. M. Hada, K. Okimura, J. Matsuo
   "Characterization of structural dynamics of VO_2 thin film on c-Al_2O_3 using in-air time-resolved X-ray diffraction"
   Physcal Reveiw B, **82**, 153401 (2010).
   DOI: 10.1103/PhysRevB.82.153401

2. M. Hada, K. Ichiki J. Matsuo
   "Characterization of vapor-deposited L-leucine nanofilm"
   Thin Solid Films, in press.
   DOI: 10.1016/j.tsf.2010.10.011

3. M. Hada, J. Matsuo
   "Effects of ambient pressure on Cu Kα X-ray radiation with millijoule high-repetition-rate femtosecond laser"
   Applied Physics B: Lasers and Optics, **99**, 173-179 (2010).
   DOI: 10.1007/s00340-010-3902-4

4. M. Hada, S. Ibuki, S. Ninomiya, T. Seki, T. Aoki and J. Matsuo
   "Evaluation of damage layer in an organic film with irradiation of energetic ion beams"
   Japanese Journal of Applied Physics, **49**, 036503 (2010).
   DOI: 10.1143/JJAP.49.036503

5. M. Hada and J. Matsuo
   "Development of femtosecond X-ray source in helium atmosphere with millijoule high-repetition-rate femtosecond laser"
   Transaction of Material Society of Japan **34**, 621-626 (2009).
   WEB: http://www.nims.go.jp/xray/ref/Vol.34No.4p621-626.pdf

6. S. Kakuta, S. Sasaki, T. Hirano, K. Ueda, T. Seki, S. Ninomiya, M. Hada and J. Matsuo

"Low damage smoothing of magnetic material films using a gas cluster ion beam"
Nuclear Instruments and Methods in Physics Research B, **257**, 677-682 (2007).
DOI: 10.1016/j.nimb.2007.01.110

Proceedings

1. M. Hada, J. Matsuo
"Evaluation of lattice motion in CdTe single crystal using in-air table-top time-resolved X-ray diffractometer"
IOP Conference Series: Materials Science and Engineering, accepted.

2. G. Sciaini, M. Hada, J. Matsuo, A. Karantza, G. Moriena, R.J.D. Miller
"Coherent Acoustic Phonons in Highly Oriented Bismuth Films Monitored by Femtosecond Electron Diffraction"
Ultrafast Phenomena 17 (2010) accepted.

3. M. Hada, S. Ninomiya, T. Seki, T. Aoki and J. Matsuo
"Using ellipsometry for the evaluation of surface damage and sputtering yield in organic films with irradiation of argon cluster ion beams"
Surface and Interface Analysis (2010) accepted.
DOI: 10.1002/sia.3452

4. J. Matsuo, S. Ninomiya, H. Yamada, K. Ichiki, Y. Wakamatsu, M. Hada, T. Seki and T. Aoki
"SIMS with highly excited primary beams for molecular depth profiling and imaging for organic and biological materials"
Surface and Interface Analysis **42**, 1612-1615 (2010).
DOI: 10.1002/sia.3585

5. M. Hada, Y. Hontani, S. Ibuki, K. Ichiki, S. Ninomiya, T. Seki, T. Aoki, J. Matsuo
"Evaluation of Surface Damage of Organic Films due to Irradiation with Energetic Ion Beams"
AIP Conference Series IIT2010 (2010) accepted.

6. M. Hada and J. Matsuo
"Development of ultrafast pulse X-ray source in ambient pressure with millijoule high repetition rate femtosecond laser"
Zero-Carbon Energy Kyoto 2009, 300-305 (2009).

International Conferences

1. G. Sciaini, M. Hada, J. Matsuo, A. Karantza, G. Moriena, R.J.D. Miller
   "Coherent Acoustic Phonons in Highly Oriented Bismuth Films Monitored by Femtosecond Electron Diffraction"
   Ultrafast Phenomena 17 (USA, July 2010, oral).

2. M. Hada, S. Ibuki, S. Ninomiya, T. Seki, T. Aoki and J. Matsuo
   "Evaluation of damage layer in an organic film with irradiation of energetic ion beams"
   18th International Conference on Ion Implantation Technology (Japan, June 2010, poster).

3. M. Hada and J. Matsuo "Evaluation of Lattice Motion with Vacuum-free Compact Designed Time-resolved X-ray Diffraction "The Banff Meeting on Structural Dynamics (Canada, Febrary 2010, poster)

4. G. Moriena, M. Hada, J. Matsuo , C. Lu, Hubert Jean-Ruel, M. Gao, R. Cooney, A. Karantza, G. Sciaini and R.J.D. Miller
   "Coherent acoustic phonons in ultrathin monocrystalline Bismuth"
   The Banff Meeting on Structural Dynamics (Canada, Febrary 2010, poster)

5. J. Matsuo, M. Hada
   "In-air femtosecond X-ray source"
   The Banff Meeting on Structural Dynamics (Canada, Febrary 2010, oral)

6. M. Hada, J. Matsuo
   "Effect of ambient pressure on Cu Kα X-ray radiation with millijoule and high-repetition-rate femtosecond laser"
   International Symposium on the Physics of Excitation-assisted Nanoprocesses(ISPEN2009) (Japan, November 2009, poster).

7. J. Matsuo, S. Ninomiya, K. Ichiki, H. Yamada, M. Hada, T. Aoki, T. Seki
   "Surface Damage Evaluation of Organic Materials Irradiated with Ar Cluster Ions"
   AVS 56th International Symposium USA, November 2009, oral).

8. M. Hada, S. Ninomiya, T. Seki, T. Aoki and J. Matsuo
   "Evaluation of optical properties in organic films with irradiation of

cluster ion beams"
17th International Conference on Secondary Ion Mass Spectrometry (Canada, November 2009, poster).

9. J. Matsuo, H. Yamada, K. Ichiki, M. Hada, S. Ninomiya, T. Seki and T. Aoki
"Material processing and evaluation with cluster ion beam"
10th International Symposium on Sputtering & Plasma Process (Japan, July 2009, oral).

10. J. Matsuo, K. Ichiki, M. Hada, S. Ninomiya, T. Seki, T. Aoki, T. Nagayama and M. Tanjo
"Stress Measurement of Carbon Cluster implanted layers with in-plane Diffraction Technique"
9th International Workshop on Junction Technology (Japan, June 2009, oral).

11. K. Ichiki, S. Ninomiya, M. Hada, T. Seki, T. Aoki, J. Matsuo
"Size-selected high density large gas cluster ion beam irradiation"
2009 MRS spring meeting (USA, April 2009, poster).

12. M. Hada, J. Matsuo
"Development of femtosecond X-ray diffraction"
6th Conference on Ultrafast Surface Dynamics (Germany, July 2008, poster).

13. M. Hada, J. Matsuo
"Real-time observation of ultrafast phenomena with femtosecond X-ray diffaraction"
5th Symposium on Ultrafast Surface Dynamics (Japan, May 2006, poster).

Awards and Selected Papers

1. "Characterization of structural dynamics of VO_2 thin film on c-Al_2O_3 using in-air time-resolved X-ray diffraction" Physcal Reveiw B, **82**, 153401 by Masaki Hada et al. was selected for Virtual Journal of Nanoscale Science & Technology Vol. **22**, Issue 16 (2010).

2. "Evaluation of damage layer in an organic film with irradiation of energetic ion beams" Japanese Journal of Applied Physics, **49**, 036503

by Masaki Hada et al. was selected for Virtual Journal of Nanoscale Science & Technology Vol. **21**, Issue 15 (2010).